

DISSERTATION

TOWARDS THE CHARACTERIZATION OF SILICON SURFACES: SOLID STATE
NUCLEAR MAGNETIC RESONANCE STUDIES

Submitted by

Rebecca Anne Caylor

Department of Chemistry

In partial fulfillment of the requirements

For the Degree of Doctor of Philosophy

Colorado State University

Fort Collins, Colorado

Fall 2011

Doctoral Committee:

Advisor: Gary E. Maciel

Elliot Bernstein
Alan Van Orden
Ted Watson
Amy Prieto

ABSTRACT

TOWARDS THE CHARACTERIZATION OF SILICON SURFACES: SOLID STATE NUCLEAR MAGNETIC RESONANCE STUDIES

One of the developing areas in silicon chemistry is in small silicon particles, primarily the nanoparticles regime. When on the ‘nano’ scale, silicon possesses very different properties and characteristics from bulk silicon. These properties include novel optical and electronic properties that are size dependent. Semiconductor nanoparticles possess a unique bright photoluminescence when in the nanoparticle regime. The photoluminescence in the nanoparticle regime answers the problem of inefficient emissions, which have previously been a problem in bulk silicon, for use in solar cells. Nanoparticle silicon (*np*-Si) is also biocompatible, allowing for the use in various biological applications including biological tracers, biosensors, delivery of medicine, as well as many others. Although *np*-Si is widely used, its surface structure still remains largely debated. The surface structure of *np*-Si is of critical importance as it affects the reactivity of the sample as well as the properties the samples possess. Relative to other silicon samples, *np*-Si lends itself to be studied by solid state NMR due to its higher surface area, although other types of silicon samples have been studied to some degree in this dissertation project. The surface structure and adjacent interior of *np*-Si, obtained as

commercially available silicon nanopowder, were studied in this project using multinuclear, solid-state NMR spectroscopy. The results are consistent with an overall picture in which the bulk of the *np*-Si interior consists of highly ordered ('crystalline') silicon atoms, each bound tetrahedrally to four other silicon atoms. From a combination of ^1H and ^{29}Si magic-angle-spinning (MAS) NMR results and quantum mechanical ^{29}Si chemical shift calculations, silicon atoms on the surface of 'as-received' *np*-Si were found to exist in a variety of chemical structures, including primarily structures of the types $(\text{Si-O})_n(\text{Si-})_{3-n}\mathbf{Si}\text{-H}$ (with $n = 1 - 3$) and $(\text{Si-O})_2\mathbf{Si}(\text{H})\text{OH}$, where \mathbf{Si} stands for a surface silicon atom and *Si* represents another silicon atom that is attached to \mathbf{Si} by either a $\mathbf{Si}\text{-Si}$ bond or a $\mathbf{Si}\text{-O-Si}$ linkage. The relative populations of each of these structures can be modified by chemical treatment, including with O_2 gas at elevated temperature. A deliberately oxidized sample displays an increased population of $(\text{Si-O})_3\mathbf{Si}\text{-H}$, as well as $(\text{Si-O})_3\mathbf{Si}\text{OH}$ sites. Considerable heterogeneity of some types of surface structures was observed. A comparison of ^{29}Si and ^1H MAS experiments provide strong evidence for a modest population of silanol ($\mathbf{Si}\text{-OH}$) moieties, along with the dominant $\mathbf{Si}\text{-H}$ sites, on the surface of 'unmodified' *np*-Si; the former moieties are enhanced by deliberate oxidation of the sample. Dipolar-dephasing experiments provide further evidence of $\mathbf{Si}\text{-H}$ sites on the surface.

ACKNOWLEDGEMENT

To my loving husband, André, who helped and supported me in all my endeavors and my wonderful daughter, Myamór, who was a gift along the way.

TABLE OF CONTENTS

Chapter 1. Introduction.....	p. 1
Chapter 2. The Silicon Surface	p. 7
Chapter 3. Preliminary Studies: Silicon Powder.....	p. 11
Chapter 4. Synthesis of Silicon Nanoparticles	p. 15
Chapter 5. Surface Structure of Commercial Silicon Nanoparticles (<i>np</i> -Si).....	p. 21
Chapter 6. The Search of Better NMR Characterization Techniques	p. 79
A. $^1\text{H}\rightarrow^{29}\text{Si}$ Heteronuclear Correlation Spectroscopy.....	p. 80
B. Comparison of $^1\text{H}\rightarrow^{29}\text{Si}$ Hetcor Techniques via direct (X) detection	p. 87
C. Indirect Detection $\{^{29}\text{Si}\rightarrow^1\text{H}\}$ HetCor	p. 109
D. Overall summary of HetCor comparisons	p. 119
Chapter 7. General Conclusions Regarding the Silicon Surface.....	p. 121
Appendix I. Saving Transverse Magnetization	p. 124
Appendix II. Molecular-Level Consequences of Biomass Pretreatment by Dilute Sulfuric Acid at Various Temperatures	p. 143

LIST OF FIGURES

Figure 2.1. Possible structural features of the oxidized surface of a crystalline silicon sample. The interior core would still be assumed to consist of Si-Si bonds.

Figure 3.1. ^{29}Si CP/MAS spectrum of silicon powder.

Figure 3.2. ^{29}Si DP/MAS spectrum of silicon powder.

Figure 4.1. ^{13}C CP/MAS spectra of synthesized ‘silicon nanoparticles’ a) The spectrum of the silicon nanoparticles before they were cleaned to remove the naphthalene. b) The spectrum after cleaning to remove naphthalene.

Figure 4.2. ^{29}Si CP/MAS spectrum of synthesized ‘silicon nanoparticles’.

Figure 4.3. ^{29}Si DP/MAS spectrum of synthesized ‘silicon nanoparticles’.

Figure 5.1. X-ray powder diffraction pattern for *np*-Si.

Figure 5.2. Proton-coupled ^{29}Si (119.2 MHz) DP/MAS NMR spectrum of *np*-Si evacuated at 150 °C.

Figure 5.3. ^{29}Si CP/MAS spectra of samples based on *np*-Si. ^1H -decoupled, 7 kHz MAS and 14 ms CP contact time unless noted otherwise and evacuated at 150 °C. A) 1 ms contact time. B) 14 ms contact time. C) ^1H -coupled. D) $^2\text{H}_2\text{O}$ -treated. E) O_2 -treated (oxidized) at 500 °C. F) O_2 -treated (oxidized) and $^1\text{H}_2\text{O}$ -treated. G) $^1\text{H}_2\text{O}$ -treated.

Figure 5.4. ^1H MAS NMR spectra of *np*-Si and treated *np*-Si samples. A) As-received *np*-Si. B) Pentane-treated and then evacuated at 150 °C. D) $^2\text{H}_2\text{O}$ -treated, then evacuated at 150 °C. E) O_2 -treated (oxidized) at 500 °C, then evacuated at 500 °C. F) O_2 -treated (oxidized) at 500 °C, then $^1\text{H}_2\text{O}$ -treated and evacuated at 150 °C. G) $^1\text{H}_2\text{O}$ -treated, then evacuated at 150 °C.

Figure 5.5. ^1H MAS NMR spectra of *np*-Si and treated *np*-Si samples. a) CH_3OH -treated. b) Pentane-treated, then evacuated at 500 °C. c) Evacuated at 500 °C. d) O_2 -treated (oxidized) at 500 °C, then $^2\text{H}_2\text{O}$ -treated, then evacuated at 150 °C.

Figure 5.6. Dipolar-dephasing ^{29}Si CP/MAS spectra of *np*-Si.

Figure 5.7. A) ^1H MAS Depth-Echo spectra of a *np*-Si sample evacuated at 150 °C as a function of total echo time, $\tau = 2\tau_1 + 2\tau_2$. B) Deconvolution/simulation contributions to the ^1H NMR spectrum obtained at $\tau = 280 \mu\text{s}$.

Figure 5.8. ^2H MAS NMR spectra of treated silica gel and treated *np*-Si samples. a) $^2\text{H}_2\text{O}$ -treated then 150 °C evacuated silica gel. b) 500 °C O_2 -treated then $^2\text{H}_2\text{O}$ -treated then 150 °C evacuated *np*-Si. c) $^2\text{H}_2\text{O}$ -treated then 150 °C evacuated *np*-Si.

Figure 5.9. Experimental and simulated (calculated) proton-decoupled ^{29}Si CP/MAS NMR spectra of *np*-Si evacuated at 150 °C and their difference spectrum for a CP contact time of 14 ms.

Figure 5.10. Experimental and simulated (calculated) proton-decoupled ^{29}Si CP/MAS NMR spectra of *np*-Si evacuated at 150 °C and their difference spectrum for a CP contact time of 1.0 ms.

Figure 5.11. Experimental and simulated (calculated) proton-coupled ^{29}Si CP/MAS NMR spectra of *np*-Si evacuated at 150 °C and their difference spectrum for a CP contact time of 14 ms.

Figure 5.12. Experimental and simulated (calculated) proton decoupled ^{29}Si CP/MAS NMR spectra of $^2\text{H}_2\text{O}$ -treated *np*-Si and their difference spectrum for a CP contact time of 14 ms.

Figure 5.13. Experimental and simulated (calculated) proton decoupled ^{29}Si CP/MAS NMR spectra of oxidized *np*-Si and their difference spectrum for a CP contact time of 14 ms.

Figure 5.14. Experimental and simulated (calculated) proton-decoupled ^{29}Si CP/MAS NMR spectra of oxidized and $^1\text{H}_2\text{O}$ -treated *np*-Si and their difference spectrum for a CP contact time of 14 ms.

Figure 5.15. Experimental and simulated (calculated) proton decoupled ^{29}Si CP/MAS NMR spectra of $^1\text{H}_2\text{O}$ -treated *np*-Si and their difference spectrum for a CP contact time of 14 ms.

Figure 5.16. Determination of carbon content in *np*-Si via spin-counting.

Figure 6.1. Generic $^1\text{H} \rightarrow ^{29}\text{Si}$ HetCor pulse sequence.

Figure 6.2. The structure of octakis(dimethylsiloxy)-T8-silsesquioxane, Q8M8_H.

Figure 6.3. ^{29}Si CP/MAS spectrum of Q8M8_H.

Figure 6.4. ^1H MAS spectrum of Q8M8_H.

Figure 6.5. $^1\text{H}\rightarrow^{29}\text{Si}$ HetCor pulse sequences under various conditions. **A.** Lee-Goldburg during the evolution period and Hartmann-Hahn cross polarization during the mixing period. **B.** Lee-Goldburg during the evolution period and Lee-Goldburg cross polarization during the mixing period. **C.** MREV-8 during the evolution period and Hartmann-Hahn cross polarization during the mixing period. **D.** MREV-8 during the evolution period and Lee-Goldburg cross polarization during the mixing period.

Figure 6.6. Contour plots of $^1\text{H}\rightarrow^{29}\text{Si}$ HetCor spectra of Q8M8_H, obtained with Lee-Goldburg applied during the evolution period and Hartmann-Hahn cross polarization during the mixing period. Various mixing times were examined.

Figure 6.7. Stacked plots of $^1\text{H}\rightarrow^{29}\text{Si}$ HetCor spectra of Q8M8_H with Lee-Goldburg applied during the evolution period and Hartmann Hahn cross polarization during the mixing period. Various mixing times were examined.

Figure 6.8. Contour plots of $^1\text{H}\rightarrow^{29}\text{Si}$ HetCor spectra of Q8M8_H obtained with LG applied during the evolution period and LG cross polarization during the mixing period. Various mixing times were examined.

Figure 6.9. Stacked plots of $^1\text{H}\rightarrow^{29}\text{Si}$ HetCor spectra of Q8M8_H with LG applied during the evolution period and Lee-Goldburg cross polarization during the mixing period. Various mixing times were examined.

Figure 6.10. **A.** Region of interest for when Lee-Goldburg cross polarization was not used during the mixing period. **B.** Region of interest for when Lee-Goldburg cross polarization was used during the mixing period.

Figure 6.11. Contour plots of $^1\text{H}\rightarrow^{29}\text{Si}$ HetCor spectra of Q8M8_H obtained with MREV-8 applied during the evolution period and Hartmann-Hahn cross polarization during the mixing period. Various mixing times were examined.

Figure 6.12. Stacked plots of $^1\text{H}\rightarrow^{29}\text{Si}$ HetCor spectra of Q8M8_H obtained with MREV-8 applied during the evolution period and Hartmann-Hahn cross polarization during the mixing period. Various mixing times were examined.

Figure 6.13. Contour plots of $^1\text{H}\rightarrow^{29}\text{Si}$ HetCor spectra obtained with MREV-8 applied during the evolution period and Lee-Goldburg cross polarization during the mixing period. Various mixing times were examined.

Figure 6.14. Stacked plots of $^1\text{H}\rightarrow^{29}\text{Si}$ HetCor spectra obtained with MREV-8 applied during the evolution period and Lee-Goldburg cross polarization during the mixing period. Various mixing times were examined.

Figure 6.15. Comparison of the region of interest (0.2 ms CT) corresponding to the pulse-sequences shown in Figure 5.5. A. Based on the sequence shown in Figure 5.5A. B. Based on the sequence shown in Figure 5.5B. C. Based on the sequence shown in Figure 5.5C. D. Based on the sequence shown in Figure 5.5D.

Figure 6.16. A comparison of the efficiency of WIM-24 for polarization transfer with Hartmann-Hahn polarization transfer. A. The ^{13}C CP/MAS spectrum of hexamethylbenzene taken with a contact time of 0.120 ms. B. The ^{13}C CP/MAS spectrum of hexamethylbenzene taken with a contact time of 0.350 ms using Hartmann-Hahn cross polarization. C. The ^{13}C CP/MAS spectrum of hexamethylbenzene taken with one WIM-24 cycle, a contact time of 0.120 ms.

Figure 6.17. Contour plots of $^1\text{H}\rightarrow^{29}\text{Si}$ HetCor spectra a Q8M8_H/t-butyl trichlorosilane mixture, obtained with Lee-Goldburg applied during the evolution period and Hartman-Hahn cross polarization during the mixing period. Various mixing times were examined.

Figure 6.18. Stacked plots of $^1\text{H}\rightarrow^{29}\text{Si}$ HetCor spectra a Q8M8_H/t-butyl trichlorosilane mixture, obtained with Lee-Goldburg applied during the evolution period and Hartman-Hahn cross polarization during the mixing period. Various mixing times were examined.

Figure 6.19. Contour plots of $^1\text{H}\rightarrow^{29}\text{Si}$ HetCor spectra a Q8M8_H/t-butyl trichlorosilane mixture, obtained with Lee-Goldburg applied during the evolution period and Lee-Goldburg cross polarization during the mixing period. Various mixing times were examined.

Figure 6.20. Stacked plots of $^1\text{H}\rightarrow^{29}\text{Si}$ HetCor spectra a Q8M8_H/t-butyl trichlorosilane mixture, obtained with Lee-Goldburg applied during the evolution period and Lee-Goldburg cross polarization during the mixing period. Various mixing times were examined.

Figure 6.21. Pulse sequence for an indirect detection $\{^{29}\text{Si}\rightarrow^1\text{H}\}$ HetCor technique.

Figure 6.22. Contour plot of $\{^1\text{H}\rightarrow^{13}\text{C}\}$ HetCor spectrum of a hexamethylbenzene and adamantane mixture, obtained using direct detection.

Figure 6.23. Slice, of HetCor spectrum shown in Figure 5.22, at a proton chemical shift of 2ppm.

Figure 6.24. Contour plot of $\{^{13}\text{C}\rightarrow^1\text{H}\}$ HetCor spectrum obtained using indirect detection and with cw decoupling during detection, on a mixture of hexamethylbenzene and adamantane.

Figure 6.25. Slice, of the HetCor spectrum shown in Figure 5.24, at a ^1H chemical shift of 2ppm.

Figure 6.26. Contour plot of an indirect detection $\{^{13}\text{C}\rightarrow^1\text{H}\}$ HetCor, obtained with TPPM decoupling during detection, on a mixture of hexamethylbenzene and adamantane mixture.

Figure 6.27. Slice, of the HetCor spectrum shown in Figure 5.26, at a proton chemical shift of 2 ppm.

Figure 6.28. Contour plot of an indirect detection $\{^{13}\text{C}\rightarrow^1\text{H}\}$ HetCor experiment, obtained with Spinal-64 decoupling during detection, on a mixture of hexamethylbenzene and adamantane.

Figure 6.29. Slice, of the HetCor spectrum shown in Figure 5.28, at a proton chemical shift of 2ppm.

Figure AI.1. The pulse sequence, ALT-1, for preserving transverse magnetization without ^1H decoupling during the storage period, shown for the case of ‘initial’ transverse magnetization generated by cross polarization.

Figure AI.2. Vector diagram corresponding to ALT-1. M_α and M_β represent two orthogonal components of the ‘initial’ transverse magnetization, which is along the x or the y axis at $t = a$.

Figure AI.3. Comparison of the spectral intensities of the ^{13}C NMR spectrum of static hexamethylbenzene (HMB) as a function of storage time, τ_s .

Figure AI.4. Comparison of storage efficiencies (in terms of the total area of the static HMB spectrum) for various magnetization storage sequences, as a function of storage time τ_s .

Figure AI.5. Effect of sample spinning on storage efficiency by ALT-1 on HMB.

Figure AI.6. Comparison among various magnetization storage sequences of the storage efficiency (as measured in terms of spectral area) of the ^{13}C spectrum of methanol absorbed in a rose stem, as a function of storage time τ_s .

Figure AII.1. Structure of dominant chemical units in wood. a) cellulose, b) the syringyl unit of lignin (S), c) the guaiacyl unit of lignin (G) and d) a typical $\text{C}_\beta\text{-O-C}_4$ ($\beta\text{-O-4}$) linkage of lignin.

Figure AII.2. ^{13}C CP/MAS NMR spectrum of water-saturated poplar sawdust.

Figure AII.3. ^{13}C CP/MAS spectra of poplar sawdust with various treatment temperatures in 0.5 wt% H_2SO_4 .

Figure AII.4. ^{13}C CP/MAS spectra of poplar sawdust treated at 120 °C with 0.5 wt% H_2SO_4 , as a function of treatment time.

Figure AII.5. ^{13}C CP/MAS spectra of poplar sawdust treated at 120 °C for 15 min with various H_2SO_4 concentrations.

Figure AII.6. Lignin region of the ^{13}C CP/MAS NMR spectra of poplar sawdust samples treated with 0.5 wt% H_2SO_4 , as a function of (A) treatment time and (B) temperature.

Figure AII.7. $T_{1\text{C}}$ of holocellulose (65 – 110 ppm), \blacklozenge , and lignin (130 – 160 ppm), \blacksquare , regions of the ^{13}C CP/MAS spectra of poplar sawdust, as a function of pretreatment temperature.

Figure AII.8. $T_{1\text{C}}$ of holocellulose (65 – 110 ppm), \blacklozenge , and lignin (130 – 160 ppm), \blacksquare , regions of the ^{13}C CP/MAS spectra of poplar sawdust, as a function of pretreatment time.

Figure AII.9. $T_{1\text{H}}$ of holocellulose (65 – 110 ppm), \blacklozenge , and lignin (130 – 160 ppm), \blacksquare , regions of the ^{13}C CP/MAS spectra of poplar sawdust, as a function of pretreatment temperature.

Figure AII.10. $T_{1\text{H}}$ of holocellulose (65 – 110 ppm), \blacklozenge , and lignin (130 – 160 ppm), \blacksquare , regions of the ^{13}C CP/MAS spectra of poplar sawdust, as a function of treatment time.

Figure AII.11. T_{CH} for the 65-110 ppm region of the ^{13}C CP/MAS spectra of poplar sawdust, as a function of treatment time.

Figure AII.12. T_{CH} for (A) the 130-140 ppm region (S1 + G1) and (B) the 140-160 ppm region (S3 + S5 + G3 + G4) of the ^{13}C CP/MAS spectra of poplar sawdust, as a function of treatment time.

Figure AII.13. T_{CH} for the 130-160 ppm region of the ^{13}C CP/MAS spectra of poplar sawdust samples, as a function of H_2SO_4 concentration.

Figure AII.14. $T_{1\rho\text{H}}$ for the 65-110 ppm region of the ^{13}C CP/MAS spectra of poplar sawdust, as a function of treatment time.

Figure AII.15. T_{CH} (A) and $T_{1\rho\text{H}}$ (B) for the 130-160 ppm region of the ^{13}C CP/MAS spectra of poplar sawdust, as a function of treatment time.

Figure AII.16. T_{CH} (A) and $T_{1\rho\text{H}}$ (B) for the 130-160 ppm region of the ^{13}C CP/MAS spectra of poplar sawdust samples, as a function of H_2SO_4 concentration.

CHAPTER 1

Introduction

A long-term goal in our research group has been to characterize the surface of ultra-thin silicon wafers by solid state nuclear magnetic resonance (ssNMR) through the use of novel instrumentation. Due to the low surface area of such samples, special low temperature instrumentation was deemed necessary to acquire signals with a useful level of signal to noise. Because of this, emphasis in this particular project was refocused onto silicon *particles* because of recognition that the ability to achieve our goal of studying ultra-thin silicon wafer surfaces could not be achieved within the time span of a normal thesis project. The much higher surface area of silicon *particles* should allow for the use of current instrumentation, without having to build any specialized low temperature instrumentation.

One of the developing areas in silicon chemistry is in small silicon particles; primarily the nanoparticles regime.¹ When on the ‘nano’ scale, silicon possesses very different properties and characteristics from bulk silicon. These properties included novel optical and electronic properties that are size dependent.¹ Semiconductor nanoparticles possess a unique bright photoluminescence. The photoluminescence in the nanoparticle regime answers the problem of inefficient emissions, which have previously

been a problem in bulk silicon, for use in solar cells.² Silicon nanoparticles are also biocompatible, allowing for the use in various biological applications including biological tracers, biosensors, delivery of medicine, as well as many others.^{3,4} The focus of our studies is on the surface moieties of the *np*-Si. It is critical for one to know what is on the surface of *np*-Si due to the widespread applications. ssNMR provides one with a tool to determine what is on the surface of *np*-Si which is discussed in greater detail below.

While the nomenclature in the literature varies, it is generally considered that nanoparticles have a diameter in the nanometer range.^{1,3-5} For the purposes of this dissertation, we employ the following definitions: silicon powder includes silicon particles greater than 50 nm in diameter; purchased silicon nanoparticles (*np*-Si) includes silicon particles greater than 10 nm in diameter and less than 50 nm in diameter; and synthesized silicon nanoparticles includes particles that are less than 10 nm in diameter. Silicon particles are often made with an H terminating group; i.e., they are said to be hydride capped. This is the case in the studies that are the focus in this dissertation.^{3,4,6}

Techniques routinely used to study silicon samples include transmission electron microscopy (TEM) and scanning tunneling microscopy (STM), as well as Fourier transform infrared spectroscopy (FTIR). These techniques have provided a significant amount of information on various silicon samples.^{1,3,4,6-10} Despite the information provided by such studies, there still remains a lot to be determined about these silicon samples, such as the surface moieties and stability of the terminating groups that are frequently used.

Although ^{29}Si nuclei are 4.7% in natural abundance and have spin $\frac{1}{2}$, few studies on crystalline silicon samples have been performed using solid state nuclear magnetic resonance (ssNMR) and they have provided little information on surface structure. This is likely related to the low surface area of the majority of silicon samples, much lower than that necessary for surface study by ssNMR. Other samples containing silicon, such as silica gel and mica, have been widely studied by ssNMR.¹¹⁻¹³ Despite these studies, there still remains a lot to be determined on the ^{29}Si chemical shifts of various structural moieties, many of which have been estimated by quantum mechanical chemical shift calculations, using GAUSSIAN 2003, in the study reported here. ssNMR has the potential of being a very useful technique in the study of silicon surfaces, provided samples of interest have high enough surface area ($\sim 400 \text{ g/m}^2$) to obtain useful signals as well as a ^{29}Si chemical shift database available to refer to that is large enough to provide one with enough information on the chemical shift values of interest.

There are a number of techniques that are routinely used in ssNMR. NMR in the solid state lagged behind NMR in solution due to problematic line broadening effects, such as dipolar coupling and chemical shift anisotropy (CSA). These line broadening effects are averaged out in solution by the random motion that is present. Other difficulties often present in ssNMR are the large spin-lattice relaxation times and magnetic inhomogeneity of the sample. These sources of difficulty often result in very broad lines and low signal-to-noise, unless certain remedies are applied. To address some of these difficulties, specialized techniques are used, including high-power proton decoupling, cross polarization (CP) and magic angle spinning (MAS).

Cross polarization is a frequently used technique that has been demonstrated to shorten the bottleneck effect that would otherwise be present in nuclei that typically have large spin-lattice relaxation times (T_1), like ^{29}Si . This is accomplished through the transfer of polarization from ^1H (which frequently has a much smaller T_1) to ^{29}Si on a millisecond time scale.¹⁴ When desiring quantitative results, the cross polarization dynamics need to be taken into consideration. Magic-angle spinning (MAS) is a technique in which the sample rotates about an axis at the “magic” angle of 54.74° relative to the direction of the static magnetic field. MAS serves as a mechanical replacement for the random motion that is present in solution. MAS can also average the dipolar coupling to zero if the spinning rate is fast enough, which frequently is not possible for ^1H - ^1H dipolar interactions, so other techniques may be necessary in ^1H experiments. Cross polarization is often used in conjunction with magic-angle spinning (CP/MAS), a combination that was first demonstrated by Schaefer and Stejskal.¹⁵ CP/MAS has become the most widely used technique in ssNMR.

Frequently silicon samples are prepared as ‘hydride capped’, with Si-H bonds at the surface. Ideally, this results in protons being located only at the surface. After oxidation and many other types of chemical reactions at the surface, ^1H may still be located only on the surface of the silicon samples. In such cases, because the only location of protons in the silicon samples is assumed to be at the surface, analysis by $^1\text{H} \rightarrow ^{29}\text{Si}$ CP/MAS essentially becomes a surface selective technique. This allows CP/MAS ssNMR to be a critical tool in analyzing possible surface structures on the various silicon samples, assuming a high enough surface area is available to achieve adequate signals for analysis.

Other techniques in ssNMR, such as 2-D $^1\text{H} \rightarrow ^{29}\text{Si}$ ssNMR Heteronuclear Correlation Spectroscopy, also present the possibility of providing insight into the surface structure of the silicon samples provided there is enough surface area to run the experiments successfully. This dissertation takes one through my ssNMR studies of silicon samples, looking for insight into what surface moieties are present, as well as possible ways of determining what surface moieties are present.

References:

- (1) Zou, J.; Sanelle, P.; Pettigrew, K. A.; Kauzlarich, S. M. *J. Cluster Sci.* **2006**, *17*, 565.
- (2) Guenes, S.; Sariciftci, N. S. *Inorg. Chim. Acta* **2008**, *361*, 581.
- (3) Chopra, N.; Gavalas, V. G.; Hinds, B. J. *Anal. Lett.* **2007**, *40*, 2067.
- (4) O'Farrell, N.; Houlton, A.; Horrocks, B. R. *Int. J. Nanomed.* **2006**, *1*, 451.
- (5) Badia, A.; Gao, W.; Singh, S.; Demers, L.; Cuccia, L.; Reven, L. *J. Am. Chem. Soc.* **1997**, *119*, 11104.
- (6) Ogawa, H.; Ishikawa, K.; Inomata, C.; Fujimura, S. *J. Appl. Phys.* **1995**, *79*, 472.
- (7) Liao, W.-S.; Lee, S.-C. *J. Appl. Phys.* **1996**, *80*, 1171.
- (8) Takahagi, T.; Ishitani, A.; Kuroda, H. *J. Appl. Phys.* **1990**, *68*, 2187.
- (9) Tardif, F.; Chabli, A.; Danel, A.; Rochat, N.; Veillerot, M. *J. Electrochem. Soc.* **2003**, *150*, G333.
- (10) Vickerman, J. C. *Surface Analysis- The Principal Techniques*; Wiley & Sons, 1997.
- (11) Sindorf, D. W.; Maciel, G. E. *J. Phys. Chem.* **1982**, *86*, 5208.
- (12) Sindorf, D. W.; Maciel, G. E. *J. Phys. Chem.* **1983**, *87*, 5516.
- (13) Sindorf, D. W.; Maciel, G. E. *J. Am. Chem. Soc.* **1983**, *105*, 1848.
- (14) Pines, A.; Gibby, M. G.; Waugh, J. S. *J. Chem. Phys.* **1973**, *59*, 569.
- (15) Schaefer, J.; Stejskal, E. *J. Am. Chem. Soc.* **1976**, *98*.

CHAPTER 2

The Silicon Surface

One of the primary gaps of understanding in silicon samples is a detailed knowledge of the surface moieties. The silicon samples of interest, primarily commercially received silicon nanoparticles (termed *np*-Si in this dissertation), were received as ‘hydride capped’. It is important to determine what is still on the surface of the *np*-Si. It is very possible that the Si-H bond at the surface has reacted and one is no longer dealing with a ‘hydride capped’ surface. The properties of the silicon samples, specifically *np*-Si, depend on what is on the surface. According to the literature, the ‘hydride capped’ surface of silicon samples undergoes oxidation with atmospheric water, as is shown in reaction 1, resulting in a surface structure that is comparable to that of silica (like that of Figure 2.1a).^{7,16} In this dissertation, we will see evidence that suggests structures like those shown in Figure 2.1b or 2.1c for the oxidized silicon surface.

Silicon wafers, obtained as ‘hydride capped’, are believed to undergo oxidation in the time span of minutes to days when in the presence of the atmosphere.^{9,17} Interior Si-Si bonds (bond strength:53 Kcal/mol) are weaker than Si-H bonds (bond strength:74 Kcal/mol) on the surface; therefore the surface reaction proposed in the literature proceeds according to the following stoichiometry:⁷



Alternatively, it has been speculated that Si-Si bonds are oxidized first and then Si-H bonds at the surface are oxidized second, forming a surface that is believed to be similar to that of silica, as shown in Figure 2.1a.^{7,9} The literature on these issues is not convincing, with conflicting information.^{7,9,16,17} If the oxidation does not occur completely, it may be possible to generate a surface with a structure of the type shown in Figure 2.1b, with Si-O-Si bonds, yet with Si-H still remaining at the surface. There are multiple other possible surface structures for various stages of oxidation, not all of which are shown here; one example is shown in Figure 2.1c. Although certainly of interest, the depth and rate at which the oxidation of the silicon surface occurs has not been well characterized in the literature. Our laboratory has obtained results that suggest that the hydride capped surface does not react with water from the atmosphere, but does react with oxygen from the atmosphere. Evidence for this is shown in studies performed on silicon nanoparticles (*np*-Si), shown in Chapter 5, where reactions with H₂O are minimal at best and reactions with oxygen are very substantial. Details of these reactions with the silicon surface are given in Chapter 5 of this dissertation. It is speculated that the hydride capped surface can react with oxygen as follows, with (Si) representing internal silicon:



We hope, in the long run, to better characterize the oxidation of silicon wafers under a variety of conditions.

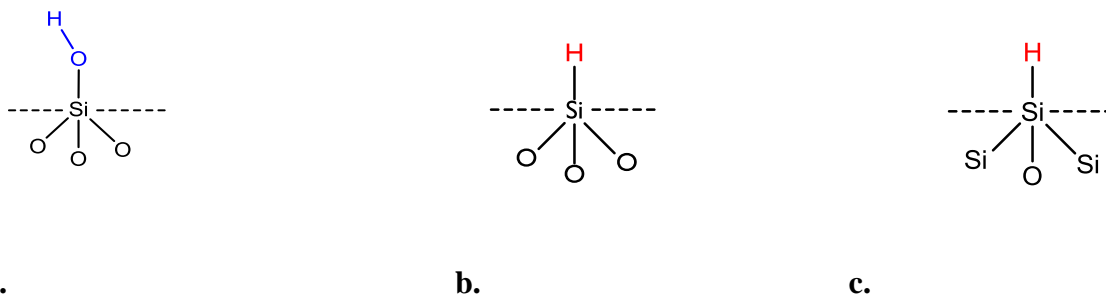


Figure 2.1. Possible structural features of the oxidized surface of a crystalline silicon sample. The interior core would still be assumed to consist of Si-Si bonds.

Our ability to understand the surface of the oxidized Si wafer is at least in part dependent upon our ability to make ssNMR chemical shift assignments. Our tentative chemical shift assignments thus far have been made on the basis of literature data of limited reliability and on the shaky assumption that we are working with a silicon surface that is oxidized to produce a surface structure similar to that of silica. It is not clear, however, if this assumption is in fact correct. The limited ^{29}Si database is addressed in this dissertation project in a variety of ways: these include working with silicon compounds of known structure, performing quantum-chemical calculations, and through the development of spectroscopic techniques for the identification of ^{29}Si chemical shifts.

It also became clear at the beginning of this dissertation project that, due to the low surface area and the need for complicated specialized instrumentation, working with silicon wafers was not going to be possible in the time span of this project because the specialized instrumentation necessary to enhance the S/N would not be available. Because of this, other silicon samples that were expected to have similar structural features on the surface were studied; these other materials are ‘hydride capped’ silicon

powder, synthesized silicon nanoparticles (supposedly 'methoxy capped'), and commercially available 'hydride capped' silicon nanoparticles (*np*-Si).

References:

- (1) Liao, W.-S.; Lee, S.-C. *J. Appl. Phys.* **1996**, *80*, 1171.
- (2) Ling, L. *J. Appl. Phys.* **1992**, *73*, 3018.
- (3) Tardif, F.; Chabli, A.; Danel, A.; Rochat, N.; Veillerot, M. *J. Electrochem. Soc.* **2003**, *150*, G333.
- (4) Tsuboi, T.; Sakka, T.; Ogata, Y. H. *Phys. Rev. B.* **1998**, *58*, 863.

CHAPTER 3

Preliminary Studies: Silicon Powder

As a first step, the first silicon surface studied was that of silicon powder (Sigma Aldrich, lot number 7440-21-3, 99.9995%). The surface area of this material was determined in our laboratory by BET measurements to be $\sim 2.5 \text{ m}^2/\text{g}$,¹⁰ much lower than the surface areas typical of materials on which NMR surface studies have been made. TEM measurements were taken, but the particle size was too large for an accurate size measurement. The manufacturer claimed the surface of the silicon powder was hydride capped. On the basis of a prevailing view in the literature,^{6,7,9,17} this study began with the view that the powder surface was possibly oxidized in a fashion similar to that which was discussed above, resulting in a surface similar to that of silica.⁷

²⁹Si and ¹H ssNMR spectra were obtained on the ‘as received’ silicon powder. The ²⁹Si CP/MAS spectrum is shown in Figure 3.1. The broad peak from about -89 ppm to about -110 ppm in Figure 3.1 corresponds to chemical shifts characteristic of a silica surface, i.e., consistent with an oxidized surface of silicon powder. If silicon powder is oxidized to provide a surface comparable to that of silica, as shown in Figure 2.1a,¹⁸ it would be expected to have a spectrum with a peak corresponding to Si-OH at a location similar to that of the Si-OH peaks of silica,^{1,17} assuming the crystalline silicon core is far

enough away from the surface that it will not affect the chemical shifts of silicon nuclei at the surface.^{1,17} This is consistent with the spectrum shown in Figure 3.1.

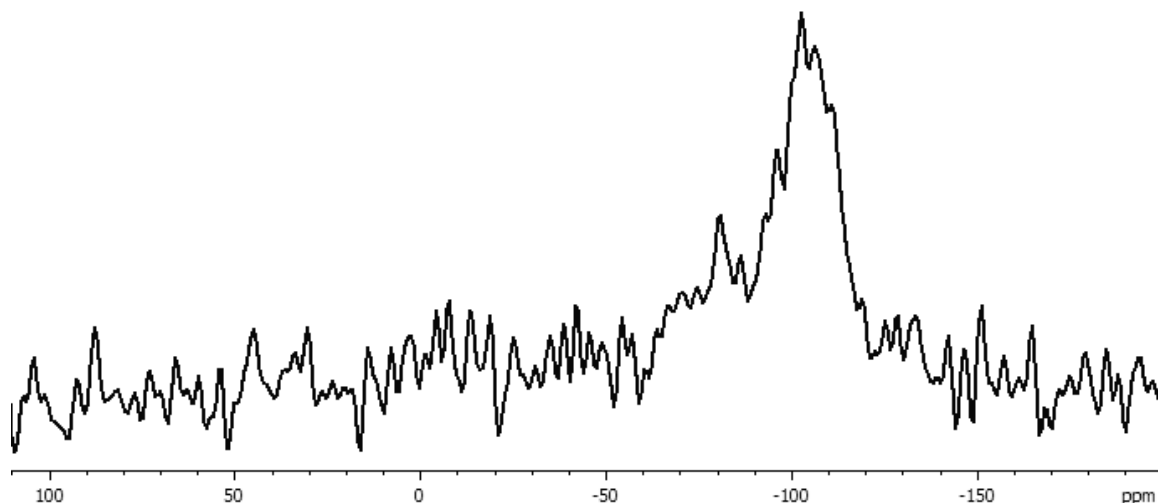


Figure 3.1. ^{29}Si CP/MAS spectrum of silicon powder, taken at 8.5 T with 16,000 acquisitions, a recovery time of 2 s and a CP contact time of 10 ms.

A directly polarized (DP) ^{29}Si spectrum (no cross polarization) of silicon powder was also taken and is shown in Figure 3.2. The use of direct polarization instead of cross polarization, assuming one has satisfied the spin-lattice relaxation (T_1) requirements, gives a representation of ^{29}Si present throughout the sample, not just the silicon nuclei at the surface, i.e., near protons. However, in the case of our silicon samples, direct polarization does not necessarily represent all ^{29}Si present in the sample uniformly, because the recovery time used (300 s) is not three times the T_1 of crystalline silicon. Preliminary measurements made in our lab determined the T_1 of crystalline silicon to be ~12000 s. The peak at -80 ppm in Figure 3.2 corresponds to what has been reported for the crystalline core of silicon,¹⁸ whereas amorphous silicon has been reported to give a broad peak centered at -38.3 ppm.

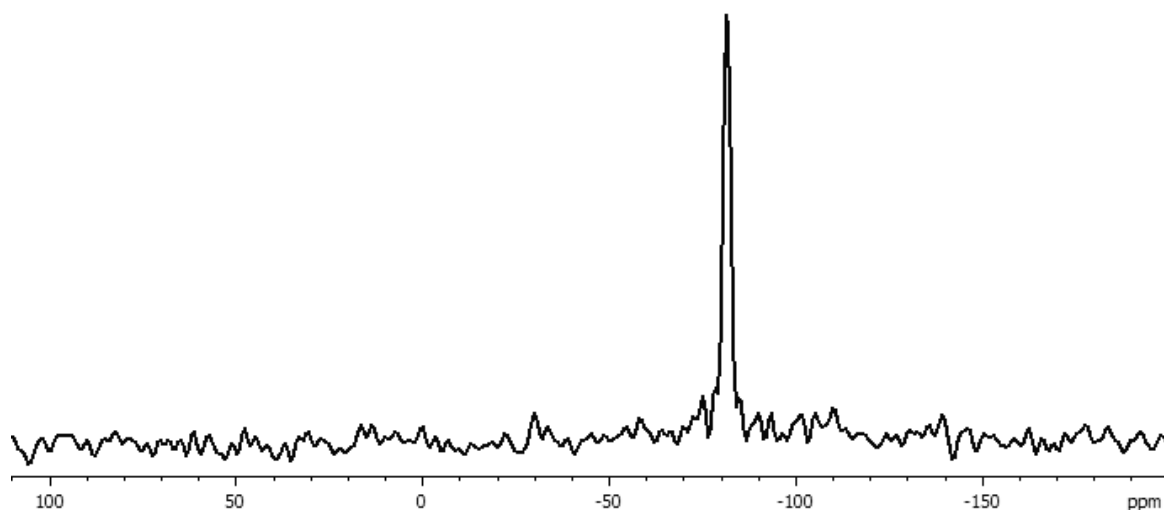


Figure 3.2. ^{29}Si DP/MAS spectrum of silicon powder, taken at 8.5 T, with 16 acquisitions and a recovery time of 300 s.

The surface area of the silicon powder was determined to be too low for our desired interests. With a surface area determined to be $\sim 2.5 \text{ m}^2/\text{g}$, much lower than surfaces typically studied by ssNMR ($\sim 400 \text{ g}/\text{m}^2$), a spectrum such as that shown in Figure 3.1 required almost nine hours to collect. A sample with a larger surface area would be ideal. This realization led to the attempted synthesis of higher surface area silicon samples, such as silicon nanoparticles, as described in the next chapter.

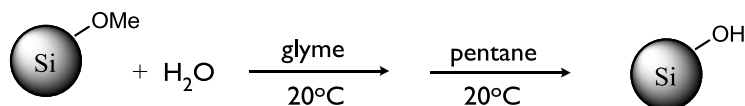
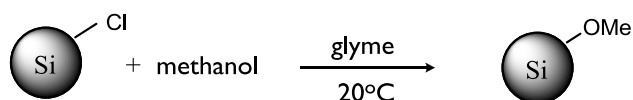
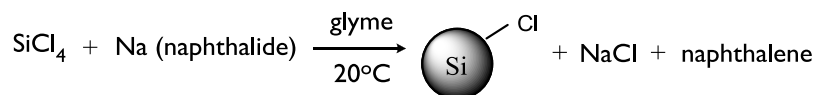
References:

- (1) Vickerman, J. C. *Surface Analysis- The Principal Techniques*; Wiley & Sons, 1997.
- (2) Tsuboi, T.; Sakka, T.; Ogata, Y. H. *Phys. Rev. B* **1998**, *58*, 863.
- (3) Tardif, F.; Chabli, A.; Danel, A.; Rochat, N.; Veillerot, M. *J. Electrochem. Soc.* **2003**, *150*, G333.
- (4) Ogawa, H.; Ishikawa, K.; Inomata, C.; Fujimura, S. *J. Appl. Phys.* **1995**, *79*, 472.
- (5) Liao, W.-S.; Lee, S.-C. *J. Appl. Phys.* **1996**, *80*, 1171.
- (6) Shao, W. L.; Shinar, J.; Gerstein, B. C. *Phys. Rev. B* **1990**, *41*, 9491.
- (7) Zou, J.; Sanelle, P.; Pettigrew, K. A.; Kauzlarich, S. M. *J. Cluster Sci.* **2006**, *17*, 565.

CHAPTER 4

Synthesis of Silicon Nanoparticles

A form of silicon with a larger surface area would require the synthesis of crystalline silicon nanoparticles, a synthesis that was undertaken before the synthetic aspects of my project were terminated for safety/health reasons. The solution synthesis of silicon nanoparticles, reported to have an average particle size of 5 nm, was followed according to the procedure by Jing Zou et al.¹ The overall transformation was proposed by the authors as follows, with  representing a Si atom of the crystalline silicon structure:¹



Sodium-naphthalide was prepared by stirring 1.46 g (6.35×10^{-2} mole) sodium (rinsed with pentane) and 5.50 g (4.29×10^{-2} mole) naphthalene in dry, distilled glyme (dimethoxyethane) overnight under N_2 gas at 20°C . The sodium-naphthalide (dark green solution) was then transferred to a round bottom 500 ml flask containing 300 ml

degassed, distilled glyme and 1.3 ml SiCl₄. The resulting mixture (dark brown) was then stirred for 2 hr at 20 °C, when 0.4 ml of distilled, degassed methanol was then added and the resulting mixture was stirred for 14 hr under N₂ at 20 °C. The resulting mixture (yellowish/orange) was then allowed to let settle for 3 hr and the yellow supernatant liquid, presumably containing the silicon nanoparticles, was transferred to another flask and the solvent was removed at 20 °C under vacuum at 5 x 10⁻³ torr. The solid that settled out from the mixture was rinsed with glyme and the supernatant liquid from the wash was added to the previous supernatant liquid portion. The solvent was again removed under vacuum at 5 x 10⁻³ torr, resulting in a sample that was expected to be methoxy capped silicon nanoparticles.

¹³C CP/MAS ssNMR analysis of the 1.25 g reaction product, before cleaning, is shown in Figure 4.1a. This spectrum shows that there was a substantial amount of naphthalene present in the sample; the peak at 125 ppm with a shoulder at 133 ppm is assumed to be from naphthalene remaining in the sample.¹⁹ Located at 10-30 ppm is an additional peak which is assigned to residual paraffin oil in which the sodium was stored. In an effort to remove the naphthalene and paraffin oil, the product was rinsed with ten 10 ml portions of pentane. Based on the solubility of naphthalene in pentane, this should have been sufficient to remove 5.50 g of naphthalene. The product (ideally Si) was then re-suspended in 300 ml of distilled, degassed glyme and 0.10 ml of distilled, degassed H₂O was added to make hydroxyl capped silicon nanoparticles. The product was then held under vacuum at 5x10⁻³ torr at 20 °C for a total of 10 days to remove any excess solvent and naphthalene. The ¹³C CP/MAS spectrum of the “cleaned” reaction product is shown in Figure 4.1b; it has a far less intense naphthalene signal than before cleaning,

although some naphthalene remains. The estimated amount of naphthalene from the ^{13}C spectrum after washing, based on ^{13}C spin counting, is 42.6 ± 0.4 mg out of 232 mg of product.

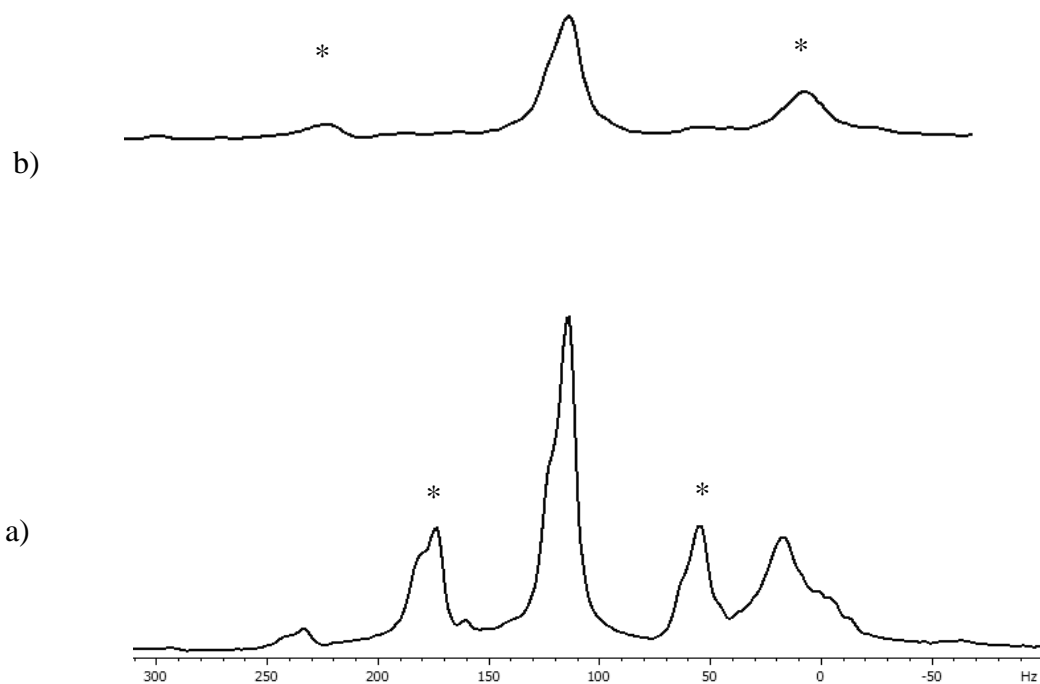


Figure 4.1. ^{13}C CP/MAS spectra of synthesized ‘silicon nanoparticles’, taken at 4.7 T, a recovery time of 2 s and a CP contact time of 10 ms. a) The spectrum of the silicon nanoparticles before they were cleaned to remove the naphthalene. b) The spectrum after cleaning to remove naphthalene. The spectra are scaled for the number of acquisitions and sample size. Spinning sidebands are denoted by asterisks.

The ^{29}Si CP/MAS spectrum of the product (presumably hydroxyl capped silicon nanoparticles) after washing with pentane is shown in Figure 4.2. The broad peak

centered at -80 ppm in Figure 4.2 is assigned to the crystalline core;¹⁸ the peak at -99 ppm and -109 are assigned to Si–OH moieties on the surface,¹ and the broad peak in the range of -5 ppm to -45 ppm tentatively is assigned to SiCl_x.²⁰ The core Si peak at -80 ppm is broad in this case, presumably because there are structural defects in the crystallinity, which causes line broadening.

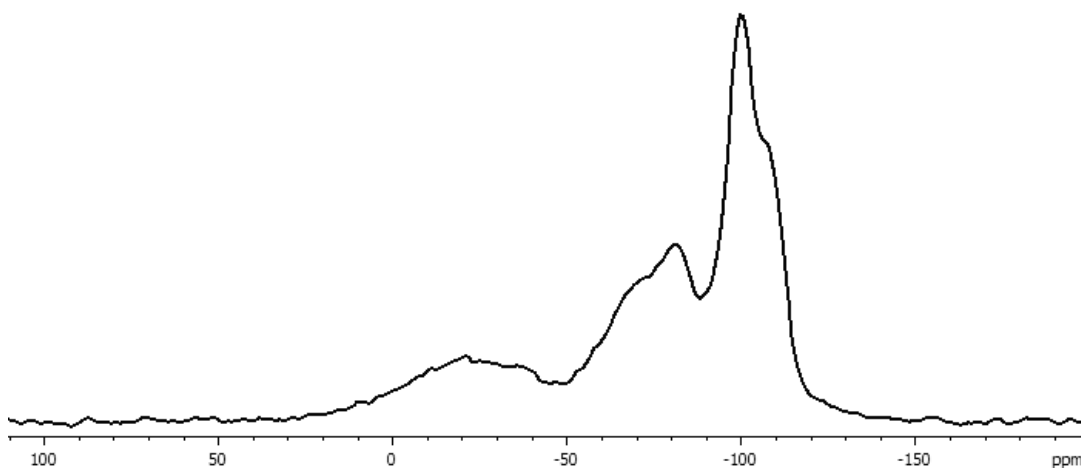


Figure 4.2. ²⁹Si CP/MAS spectrum of silicon nanoparticles, taken at 8.5 T with 1,600 acquisitions, a recovery time of 2 s and a CP contact time of 10 ms.

The direct polarization (DP) ²⁹Si NMR spectrum of the synthesized silicon nanoparticles is shown in Figure 4.3. The peak at -80 in Figure 4.3 is assigned to the crystalline core; the peaks at -99 ppm and -109 ppm are assigned to Si–OH on the surface.^{12,18} The peak at -80 ppm assigned to the crystalline core is also broad here, due presumably to structural defects in the crystallinity, especially near the surface. Given that direct polarization is representative of all ²⁹Si nuclei located throughout the sample (assuming a sufficiently long repetition delay, 12,000 s, is used), and not just those located near ¹H, it can be seen when comparing the DP/MAS spectra of the silicon

powder (Figure 3.2) and synthesized ‘silicon nanoparticles’ (Figure 4.3) that the fraction of silicon nuclei that are part of a crystalline silicon structure (-80 ppm) is larger in the silicon powder. In the direct polarization spectrum of the synthesized ‘silicon nanoparticles’ (Figure 4.3) the peak corresponding to interior core silicon is far less dominant due to the smaller ratio of core crystalline ^{29}Si to surface ^{29}Si when compared to the ratios for silicon powder.

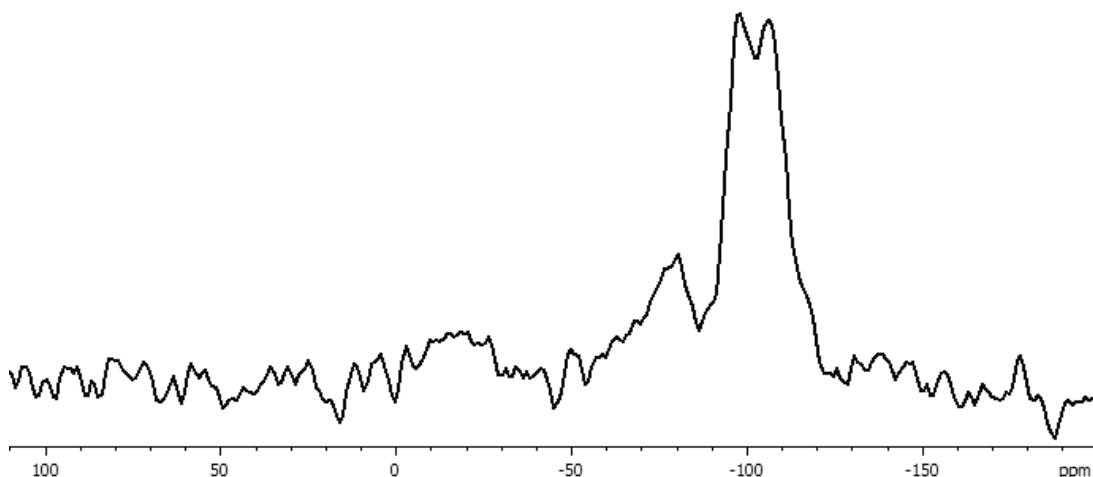


Figure 4.3. ^{29}Si DP/MAS spectrum of synthesized ‘silicon nanoparticles’, taken at 4.7 T, with 52 acquisitions and a recovery time of 5,000 s.

The synthetic aspects of my project were terminated for health reasons, eliminating further progress on synthesized ‘silicon nanoparticles’. There is a commercially available form of ‘silicon nanoparticles’, termed in this dissertation as *np-Si* (~50 nm). Although the particle size is not small as that of the synthesized ‘silicon nanoparticles’ (~5 nm), this commercially available material was chosen as a compromise between the commercially available silicon powder and the synthesized ‘silicon nanoparticles’.

References:

- (1) Zou, J.; Sanelle, P.; Pettigrew, K. A.; Kauzlarich, S. M. *J. Cluster Sci.* **2006**, *17*, 565.
- (2) Petit, D.; Chazalviel, J. N.; Ozanam, F.; Devreux, F. *App. Phy. Lett.* **1997**, *70*, 191.
- (3) Shao, W. L.; Shinar, J.; Gerstein, B. C. *Phys. Rev. B* **1990**, *41*, 9491.
- (4) Niemann, U.; Marsmann, H. C. *Z. Naturforsch* **1975**, *30b*, 202.
- (5) Sindorf, D. W.; Maciel, G. E. *J. Phys. Chem.* **1983**, *87*, 5516.

CHAPTER 5

Surface Structure of Commercial Silicon Nanoparticles (*np*-Si)

The contents in this dissertation chapter include a reformatted paper to be submitted for publication. The contents of this chapter summarize the large majority of my studies in characterizing silicon surfaces by ssNMR.

The Surface of Nanoparticle Silicon As Studied by Solid-State NMR

Rebecca A. Faulkner, Joseph A. DiVerdi, Takeshi Kobayashi,¹ Yuan Yang,² and Gary E. Maciel*

Department of Chemistry, Colorado State University, Fort Collins, Colorado 80523-1872

E-mail: gary.maciel@colostate.edu

Overview.

The surface structure and adjacent interior of nanoparticle silicon (*np*-Si) obtained as commercially available silicon nanopowder was studied using multinuclear, solid-state NMR spectroscopy. The results are consistent with an overall picture in which the bulk of

¹ Present Address: Ames Laboratory, Iowa State University, Ames, IA 50011

² Present Address: Colorado School of Mines, Golden, CO 80401

the *np*-Si *interior* consists of highly ordered ('crystalline') silicon atoms, each bound tetrahedrally to four other silicon atoms. From a combination of ^1H , ^{29}Si and ^2H magic-angle-spinning (MAS) NMR results and quantum mechanical ^{29}Si chemical shift calculations, silicon atoms on the *surface* of 'as-received' *np*-Si were found to exist in a variety of chemical structures, with apparent populations in the order $(\text{Si-O})_3\mathbf{Si-H} >$ sites with the same ^{29}Si chemical shift (-99 ppm) as $(\text{Si-O})_3\mathbf{SiOH}$ (which is included as a small contribution) $> (\text{HO-})_n\mathbf{Si}(\text{Si})_m(-\text{OSi})_{4-m-n} \sim (\text{Si-O})_2\mathbf{Si}(\text{H})\text{OH} >$ sites with the same ^{29}Si chemical shift (-89 ppm) as $(\text{Si-O})_2\mathbf{Si}(\text{-OH})_2$ (which is included as a small contribution) $>$ sites with the ^{29}Si chemical shift of $(\text{Si-O})_4\mathbf{Si}$ (-109 ppm), where **Si** stands for a surface silicon atom and *Si* represents another silicon atom that is attached to **Si** by either a **Si-Si** bond or a **Si-O-Si** linkage. The relative populations of each of these structures can be modified by chemical treatment, including with O_2 gas at elevated temperature. A deliberately oxidized sample displays an increased population of $(\text{Si-O})_3\mathbf{Si-H}$, as well as -99 ppm sites (including $\text{Si-O-}_3\mathbf{SiOH}$ sites). Considerable heterogeneity of some surface structures was observed. A combination of ^1H and ^2H MAS experiments provide evidence for a small population of silanol (**Si-OH**) moieties, along with the dominant **Si-H** sites, on the surface of 'unmodified' *np*-Si; the former moieties are enhanced by deliberate oxidation of the sample. An extension of the DEPTH background suppression method that permits measurement of the T_2 relaxation parameter simultaneously with background suppression is demonstrated.

Introduction.

Silicon particles, like those of other elements, often exhibit novel and unusual properties as their physical dimensions approach the nanometer scale.¹ Optical, physical and electronic properties of nanoparticle silicon (*np*-Si) can be very different from those of bulk silicon and are interesting from both a fundamental perspective and a practical viewpoint.^{1,21} *np*-Si has been found to be biocompatible,²² allowing for its use in biological tracers,²² sensors,²¹ and carriers of pharmaceuticals²² or other probes. Nanostructure silicon has shown potential as a chemical hydride (a compound that can take up and release molecular hydrogen without passing through the gas phase).²³ The chemical nature and structural organization of silicon's surface atoms play a crucial role in the behavior and characteristics of *np*-Si and, although it has been subjected to considerable scrutiny, much remains to be understood about their surface structure and reactivity.

Silicon exists in several important and distinct allotropes. Crystalline silicon (*c*-Si) (available as large single crystals with high atomic purity, from which correspondingly large and thin wafers are derived) consists of silicon atoms in a tetrahedral environment with each atom bonded to four other silicon atoms. These arrangements persists throughout the bulk solid and is discontinued at the surface, beyond which there are no additional silicon atoms to provide a total of four Si-Si bonds. If no effort is made to address this valence insufficiency, then there will be a number of "dangling bonds" (equivalently "trapped free radicals") associated with these surface silicon atoms.²⁴ Hydrogen,²⁵ oxygen,²⁶ halogens²⁷ or organic ligands²⁸ can be used to

satisfy these bonding sites in a process commonly known as "passivation",²⁹ "capping"³⁰ or "termination".^{27,28}

Porous silicon (*p*-Si) is obtained by anodic etching of crystalline silicon (in the form of a thin wafer) in aqueous HF, resulting in a film of porous silicon on the surface of the wafer.³¹ This highly porous film exhibits a large surface area and high spatial inhomogeneity, with both silicon structures and pores ranging in size from meso- to nano-scale.³¹⁻³³ The crystallinity of the source silicon is retained in porous silicon.³³⁻³⁵

Amorphous silicon (*a*-Si) is another allotrope, produced by condensing silicon vapor generated by RF-plasma-sputtering of a silicon wafer on a condensing target that is maintained in an ultra high vacuum (UHV) or an inert atmosphere, for example argon.¹⁸ The *a*-Si can take the form of a powdered solid or a film, depending upon the experimental conditions.^{18,36} Amorphous silicon is a non-crystalline solid that displays a high concentration of dangling bonds.¹⁸ Hydrogenated amorphous silicon (*a*-Si:H) can be synthesized using the same method by including hydrogen or silane gas in the blanketing atmosphere, by related methods including laser ablation of elemental silicon and by hot-wire chemical vapor deposition (decomposition of gaseous silane).^{18,36} Hydrogenated amorphous silicon is also a non-crystalline solid, with a lower concentration of dangling bonds than in *a*-Si; *a*-Si:H can take the form of a powdered solid or film.³⁶

Silicon nanoparticles (*np*-Si) can be prepared via solid-state and mixed-phase methods. Depending on the method used, the preparation can result in various types of surface termination.^{1,30}

The chemical structures present on the surface of the various forms of silicon vary widely and can be modified by various treatments. Dangling bonds, essentially immobilized free radical sites, display chemical reactivity that is roughly similar to that of corresponding mobile radical species. A silicon surface that is terminated with various chemical functionalities can be manipulated in much the same fashion as are other liquid- or solid-state silicon species.³⁷ Reaction of the native silicon surface with molecular oxygen at high temperature results in the formation of a silicon oxide layer that can extend with significant depth into several layers of silicon atoms.^{26,38-40} This oxidation reaction and its product are of extreme interest and importance to silicon device technologies.

The chemical and physical information that is currently available on these silicon systems has been obtained primarily through two significantly disparate approaches: (1) the study of ultra-low surface-area materials ($\sim 10^{-4} \text{ m}^2 \text{ g}^{-1}$), using ultra-high-vacuum systems and the techniques of "surface science", that is, infra-red (IR) spectroscopy, scanning tunneling microscopy (STM), atomic force microscopy (AFM), transmission electron microscopy (TEM), high-resolution electron energy loss spectroscopy (HREELS) or x-ray photoelectron spectroscopy (XPS), etc. and (2) the study of high-surface-area materials ($\sim 10^2 \text{ m}^2 \text{ g}^{-1}$) by solid-state nuclear magnetic resonance (ssNMR). The surface of single crystal silicon has been extensively examined by the former method but has been relatively inaccessible to ssNMR, because there are an insufficient number of nuclei at the surface to overcome NMR's inherently low sensitivity. All the other silicon allotropes have been studied by ssNMR, because their higher surface areas provide plentiful nuclei for achieving satisfactory signal-to-noise ratios.

In this work a commercial preparation of *np*-Si, commercially termed "silicon nanopowder," serves as a suitable material for the detailed ssNMR examination of the number and types of structures present on the surface of the particles and their organization. The primary goal is to understand the nature of the nanoparticle surface in terms of its fundamental chemical properties. This involves observation and characterization of the surface species with the ability to uniquely discriminate among them, while subjecting them to various chemical treatments. Through the use of various nuclear spin properties, in particular the chemical shift, ssNMR provides an experimental window to achieve this goal. *np*-Si offers a high enough surface area to satisfy the requirement for a sufficient number of nuclei in the sample for NMR analysis.

Experimental.

Materials. Silicon nanopowder (98+%, #633097, Aldrich, batch 04421BH), with a reported average particle size of 50 nm, was used as described in the sections on sample preparation. ^{13}C NMR measurements (see Supporting Information) show that the as-received *np*-Si contains less than 1% carbon by weight. $^2\text{H}_2\text{O}$ (99.9 atom % as ^2H , Cambridge Isotope Labs.), tris(trimethylsilyl)silane (TTMSS, Fluka) and polydimethylsiloxane (PDMS, 2.5 MDa MW, Petrarch Systems, Inc. Bristol, PA) were used as received. All other materials used were reagent grade. O_2 gas was from Airgas (99+% UN1072).

Surface Properties. BET surface area measurements were made using a Quantasorb MS-6 system (Quantachrome, Boynton Beach, FL).

X-Ray Powder Diffractometry. X-ray diffraction (XRD) powder pattern measurements were performed using a calibrated Scintag X2 Advanced Diffraction

System (Themo Optek, Cupertino, CA) equipped with Cu K α radiation ($\lambda = 0.154$ nm) and a Peltier-cooled detector. Diffraction patterns were recorded in the 2θ range of 5 to 90° with a step size of 0.02° at a rate of 1° min⁻¹. Diffrac^{plus} EVA software (Bruker AXS, Madison, WI) with the PDF-2 database (International Centre for Diffraction Data, Newtown Square, PA) was used for background correction and peak assignment. XRD samples were prepared by dusting silicon nanopowder onto glass substrates.

Nanoparticle Silicon (*np*-Si). Silicon nanopowder was suspended in pentane at a ratio of 25 mL pentane g⁻¹ of silicon nanopowder with swirling at room temperature for a few minutes, after which the mixture was centrifuged and the clear and colorless supernatant liquid was decanted. This process was repeated two more times and the resultant solid was evacuated at for 15 h at either 150 or 300 °C and 5 x 10⁻³ Torr.

²H₂O-Treated *np*-Si. Silicon nanopowder was suspended in ²H₂O at a ratio of 25 mL ²H₂O g⁻¹ of silicon nanopowder with occasional swirling at room temperature for one hour, after which the mixture was centrifuged and the cloudy and yellow supernatant liquid was decanted. This process was repeated two more times and the resultant solid was evacuated for 15 h at 150 °C and 5 x 10⁻³ Torr.

¹H₂O-Treated *np*-Si. ¹H₂O-treated *np*-Si samples were prepared by suspending silicon nanopowder in ¹H₂O at a ratio of 25 mL ¹H₂O gram⁻¹ of silicon nanopowder with occasional swirling at room temperature for three hours, after which the mixture was centrifuged and the cloudy and yellow supernatant liquid decanted. The resultant solid was evacuated for 15 h at 150 °C and 5 x 10⁻³ Torr.

Oxidized *np*-Si Sample Preparation. O₂ gas (99+%) at atmospheric pressure was passed for one hour over silicon nanopowder contained in a ceramic boat placed in a

furnace at 500 °C. After cooling to room temperature (under flowing O₂) the solid was either used directly or treated as in the ¹H₂O-treated *np*-Si samples, including the final 150 °C evacuation.

Sample Handling. As-received silicon nanopowder and prior-to-evacuation *np*-Si samples were stored and handled in a common laboratory atmosphere with no action to prevent exposure to atmospheric oxygen or water, except as noted. After evacuation, all *np*-Si samples were handled exclusively in a dry N₂ atmosphere. Samples for spectroscopy were contained in PENCIL-II (Chemagnetics, Fort Collins, CO), zirconia MAS rotors with standard plastic-to-ceramic closures. Unless specified to the contrary below in specific cases, *all* samples were evacuated at 150 °C before NMR measurements.

DP ²⁹Si NMR. Direct-polarization (DP) solid-state ²⁹Si NMR spectra were obtained using a CMX-Infinity spectrometer (Chemagnetics) operating at 14.1 T (119.2 MHz for ²⁹Si). A single-resonance, transmission-line tuned, home-built probe with a 4.0 mm (rotor diameter) magic angle spinning (MAS) module was used with spinning speed of 13 kHz.

An initial state of transverse ²⁹Si magnetization was created using a single $\pi/2$ ²⁹Si pulse (5.0 μ s). No ¹H decoupling was used. Spectra were obtained by Fourier transformation of complex data after apodization with 60 Hz of Lorentzian line broadening. The recovery time was 6,000 s.

CP ²⁹Si NMR. Cross-polarization solid-state ²⁹Si NMR spectra were obtained using a CMX-II spectrometer (Chemagnetics) operating at 8.5 T (71.5 MHz for ²⁹Si and 360.1 MHz for ¹H). A double-resonance, home-built probe with a 5.0 mm (rotor

diameter) MAS module was used with spinning speeds up to 7.0 kHz. An initial state of transverse ^{29}Si magnetization was created via cross polarization (CP) from spin-locked protons via a variable-amplitude-modification of a Hartmann-Hahn CP match.^{14,41} In experiments using a higher MAS speed or performed on samples with a weak heteronuclear dipolar interaction, simple CP can display enhanced sensitivity to the constancy and accuracy of the match condition. During the contact interval, the spinlock field is used was varied linearly, centered on the Hartmann-Hahn match condition ($\gamma_{\text{H}}B_{1\text{H}} = \gamma_{\text{Si}}B_{1\text{Si}}$) and with extremes corresponding to one sideband away ($\gamma_{\text{H}}B_{1\text{H}} \pm v_{\text{MAS}} = \gamma_{\text{Si}}B_{1\text{Si}}$). The use of CP (either simple or with the variable-amplitude-modification) has significant effects: (1) the ^{29}Si signal from each CP-generated transient is larger than that of a corresponding DP-generated transient, (2) the number of transients acquired per unit time with CP (limited by proton T_1) is correspondingly increased over that obtained with DP (limited by ^{29}Si T_1) because, in this case, the former is shorter than the latter and (3) while for DP ^{29}Si NMR each silicon site in the sample appears with an intensity (area) proportional to its total population in the sample, provided the recovery time is sufficiently long to permit full spin-lattice relaxation, for ^{29}Si signals obtained using CP, only those silicon sites spectrally appear that are in close proximity to hydrogen (details of the relationship between signal amplitude and internuclear ^{29}Si - ^1H distance determined by details of the pulse timing and any molecular motion present). As the current understanding of the structure of *np*-Si is that hydrogen occurs solely on the surface, cross polarization can be considered to be a surface-selective method.

High-power ^1H decoupling with a rotating-field amplitude of 50 kHz was used in ^{29}Si experiments, unless otherwise specified. Spectra were obtained by Fourier

transformation of complex data after apodization with 71 Hz of Lorentzian line broadening. The $\pi/2$ pulse time was 5.0 μs in all cases. For CP experiments the CP contact time and magnetization recovery time were between 1 and 14 ms and 2 s, respectively. ^{29}Si chemical shifts are reported in parts per million, referenced to liquid TMS (0.0 ppm), based on substitution of the secondary reference TTMSS (-8.1 and -134.2 ppm relative to TMS).

^1H NMR. Solid-state ^1H NMR spectra were obtained using a CMX-Infinity spectrometer (Chemagnetics) operating at 14.1 T (600.1 MHz for ^1H) and employing a home-built, single-resonance probe, using a 3.2 mm (rotor diameter) MAS module with a spinning speed of 20 kHz in most cases or using the 360 MHz spectrometer described above (12 kHz MAS speed). An initial state of transverse ^1H magnetization was created by DP (4.0 μs $\pi/2$ pulse). As the probe exhibits a significant ^1H background (relative to the signal obtained from the samples studied here), it was necessary to experimentally suppress the background when examining the relatively low proton density *np*-Si. This was performed by the use of the DEPTH method that utilizes a number of π pulses with various rotating-frame phases to preserve the sample's legitimate signal (which arises in the more intense rotating-frame RF field in the center of the sample coil) and suppresses the background signal (which arises in the less intense rotating-frame RF field surrounding the sample coil).⁴² An extension of this method used in the work described here permits estimation of the spin-spin relaxation time (T_2) simultaneously with this background suppression.

Spectra were obtained by Fourier transformation of complex data after apodization with 60 Hz of Lorentzian line broadening. The magnetization recovery time

was 3 s. ^1H chemical shifts are reported in parts per million, referenced to liquid TMS (0.0 ppm), based on substitution of the secondary reference polydimethylsiloxane (PDMS, 0.0 ppm relative to TMS).

^2H NMR. Direct-polarization (DP) solid-state ^2H NMR spectra were obtained using a CMX-Infinity spectrometer operating at 8.5 T (55.2 MHz for ^2H). A single-resonance, transmission-line tuned, home-built probe with a 4.0 mm (rotor diameter) MAS module was used with spinning speed of 13 kHz. An initial state of transverse ^2H magnetization was created by DP (4.0 μs $\pi/2$ pulse). No ^1H decoupling was used. Spectra were obtained by Fourier transformation of complex data after apodization with 20 Hz of Lorentzian line broadening. The magnetization recovery time was 2 s. ^2H chemical shifts are reported in parts per million, referenced to liquid TMS (0.0 ppm), based on substitution of the secondary reference hexamethylbenzene- d_6 (2.2 ppm relative to TMS).

All NMR measurements were made at ambient temperature (approximately 30 $^{\circ}\text{C}$) without any temperature control.

NMR Spectrum Simulations. Each experimental spectrum was analyzed by matching a simulated spectrum made up of a series of two-dimensional contributions, each consisting of a linear combination of frequency-domain and time-domain functions corresponding to Lorentzian and Gaussian functions in the frequency dimension and either a decaying (DEPTH-echo experiments) or increasing (saturation recovery experiments) first-order exponential function in the time dimension; these simulations were carried out using custom-made algorithms, generated in Igor Pro software (Wavemetrics, Inc. Lake Oswego, OR). For each experimental spectrum, the entire experimental and calculated matrices were compared at once, instead of comparing

individual slices of the frequency dimension in one step and then comparing the time points obtained from individual comparisons in a second step.

Quantum Mechanical Chemical Shift Calculations. ^{29}Si chemical shifts were calculated for various Si-containing cluster models which potentially can represent models for the surface structure of *np*-Si. The cluster models were created from tetrahedral silicon or silica networks by replacing specific atoms and adjusting the corresponding bond distances. For the initial structures of silicon and silica, the crystalline silicon structure (Si–Si bond length = 0.235 nm)⁴³ and β -cristobalite structure (Si–O bond length = 0.161 nm, Si–O–Si bond angle = 146.4°)^{44,45} were used, respectively. For the H–Si bond length, the silane bond length (0.148 nm) was used.⁴⁶

All calculations were carried out with the GAUSSIAN 2003 program package, using the restricted Hartree-Fock (RHF) method with the 6-311+G(d, p) basis set. Chemical shielding tensors were calculated using the gauge-independent atomic orbital (GIAO) method. Theoretical shieldings σ were transformed to relative chemical shifts δ by subtracting the calculated chemical shielding of TMS. Isotropic chemical shifts were calculated from the relationship $\sigma = (\sigma_{11} + \sigma_{22} + \sigma_{33})/3$.

Results and Discussion.

***np*-Si Characterization.** The surface area measured for as-received *np*-Si was $86.3 \pm 1.1 \text{ m}^2 \text{ g}^{-1}$. Using the assumption of a spherical particle shape, this value corresponds to an average particle diameter of $40.0 \pm 0.5 \text{ nm}$. No information on the

heterogeneity of this population is available from this method. The surface areas for oxidized and $^1\text{H}_2\text{O}$ -treated *np*-Si samples were found to be $86.8 \pm 1.1 \text{ m}^2 \text{ g}^{-1}$.

Suspensions of the *np*-Si in several solvents (methanol, acetone, water) yielded in each case a pale yellow supernatant phase with significant turbidity, indicating considerable agglomeration of the particles into μm -size aggregates. No turbidity was observed when *np*-Si was suspended in pentane. *np*-Si dissolved completely in 1 M KOH to yield a clear and colorless solution. *np*-Si flocculated in 1 M HCl, yielding a clear and colorless supernatant phase.

The total (surface) proton concentration of *np*-Si was estimated by spin counting (carried out by comparing the integral of each ^1H NMR signal with that of 1,3,5-trimethoxybenzene as an external reference).⁴¹ For *np*-Si samples evacuated at 150 and 300 °C, this concentration was found to be 0.83 ± 0.07 and $0.82 \pm 0.07 \text{ mmol H g}^{-1}$, respectively. These values correspond to 5.8 ± 0.5 and $5.7 \pm 0.5 \text{ H (nm)}^{-2}$, respectively, based on the surface area measurements reported above.

The X-ray diffraction pattern for *np*-Si is shown in Figure 5.1, which demonstrates that these particles possess a significant crystalline phase. No significant difference was observed between the angular locations of the signals for *np*-Si and the corresponding values for crystalline silicon. From the width of the (111) signal and using Scherrer's formula,⁴⁷ the "size" of the crystalline phase (which is not necessarily the same as the particle size) is estimated to be $23 \pm 1 \text{ nm}$.⁴⁷ This dimension is substantially smaller than the manufacturer's reported particle size (50 nm) and the particle size estimate derived from the BET surface area measurement (40 nm). This discrepancy may be due to some combination of the following: (1) the crystalline silicon region constitutes

only a fraction of the entire particle, with a surrounding mantle, or a central core of non-diffracting material (perhaps amorphous silicon or amorphous silicon dioxide), (2) there are several diffracting grains or regions within each particle or (3) the averaging process involved in the diffraction measurement differs substantially from the corresponding average of the surface area measurement.

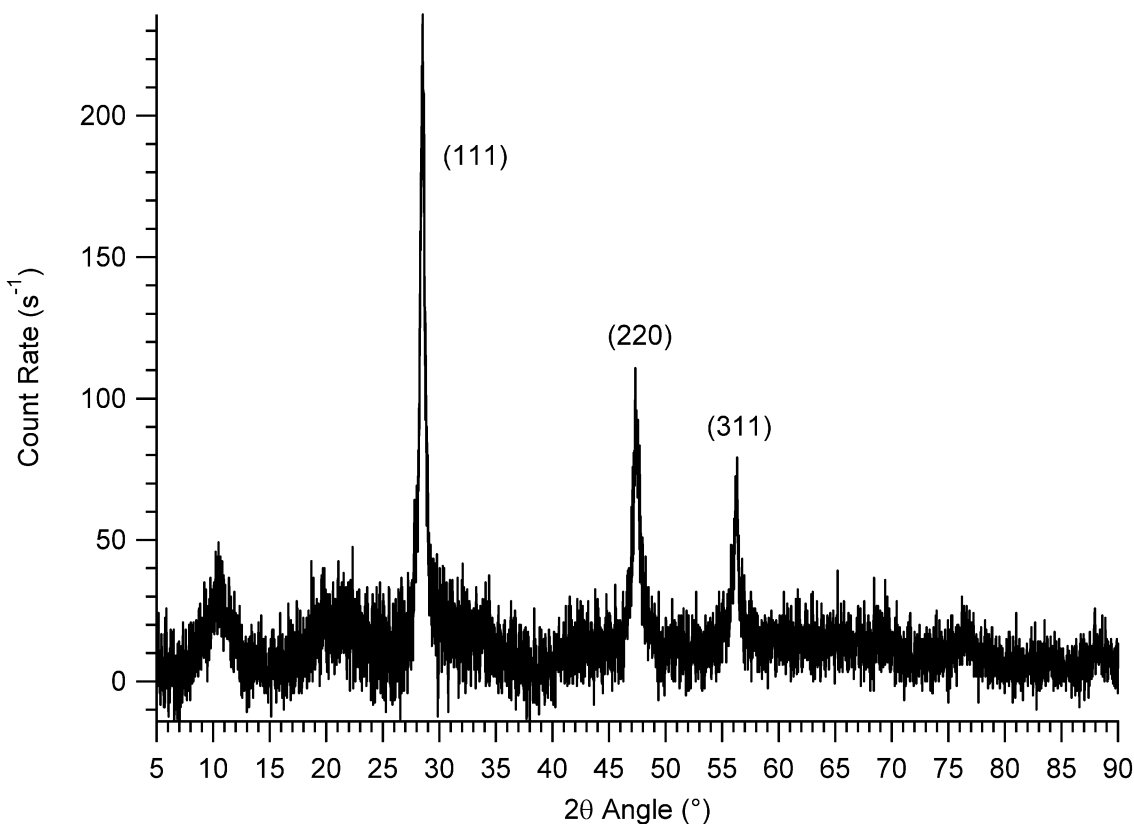


Figure 5.1. X-ray powder diffraction pattern for *np*-Si.

²⁹Si DP/MAS NMR of 150 °C Evacuated *np*-Si. Figure 5.2 shows the proton-coupled ²⁹Si DP/MAS NMR spectrum of *np*-Si evacuated at 150 °C. The chemical shift of the single signal is centered at -79 ppm, with a line width (full width at half maximum, FWHM) of 1.3 ppm (160 Hz), corresponding closely to the ²⁹Si NMR characteristics of

c-Si.¹⁸ No signal corresponding to *a*-Si (a signal centered at -40 ppm with a width ranging from 70 to 80 ppm) is seen in this spectrum.¹⁸

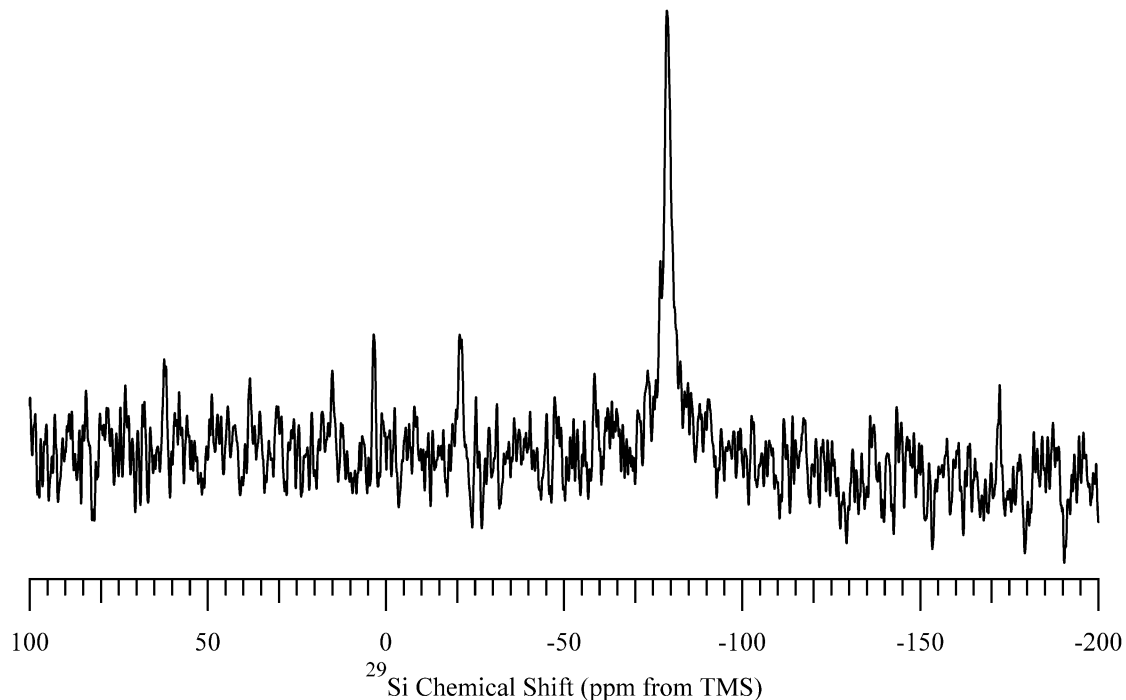


Figure 5.2. Proton-coupled ²⁹Si (119.2 MHz) DP/MAS NMR spectrum of *np*-Si evacuated at 150 °C. A MAS speed of 10 kHz was used.

The DP excitation used in obtaining this spectrum does not discriminate *per se* between surface and buried silicon atoms. However, if there is a distribution of ²⁹Si T₁ values and the recovery time used is shorter than three times the largest T₁ value, then there will be a measurable distortion in the simple relationship of signal intensity to site concentration. The ²⁹Si T₁ of the *c*-Si-like signals in Figure 5.2 was estimated (by variation of the magnetization recovery time) to be on the order of 12,000 s (data not shown). This value is comparable to that reported for *c*-Si,¹⁸ where it is also reported that ²⁹Si T₁ for *a*-Si ranges from 3,000 to 6,000 s. Although it would be questionable to

specify a lower bound with confidence, if there were a substantial amount of *a*-Si present (e.g., 10 atom % of the silicon) in the *np*-Si sample examined here, one would expect it to be revealed in this spectrum.

MAS NMR

²⁹Si CP/MAS. In comparing chemical shifts obtained in MAS experiments on solid samples with values reported on the same or similar materials in liquid samples (solutions), one should not be surprised by significant differences. These can result from a combination of sources, including small liquid-vs-solid structural differences (bond lengths and angles), unaccounted non-nearest-neighbor substituent effects, differences in local and bulk magnetic susceptibility effects, solvent effects and variations in chemical shift referencing methods. For ²⁹Si, these differences might be as large as a few ppm.

Figure 5.3 shows ²⁹Si CP/MAS spectra of a set of *np*-Si samples that have been treated in various ways. All of the spectra of Figure 5.3, except that shown in Figure 5.3A (1.0 ms CP contact time) were obtained in experiments with a CP contact time of 14 ms. The CP technique is based directly upon dipole-dipole interactions, ¹H–²⁹Si interactions in the present case, and favors ²⁹Si NMR signals of silicon atoms that are near hydrogen atoms. The CP/MAS experiments carried out with a long CP contact time (14 ms) lessen (but do not eliminate) the spatial selectivity of the method.

The ²⁹Si spectra of Figures 5.2 and 5.3 are so different that, at first glance, they seem to belong to entirely different samples. The spectral differences occur because DP/MAS and CP/MAS are based on completely different mechanisms for generating the ²⁹Si spin polarization that are observed. While the DP/MAS ²⁹Si spectrum (Fig. 5.2) relies on ²⁹Si spin-lattice relaxation, which in turn is based on time-dependent spin interactions

(e.g., the fluctuating fields generated by a small concentration of unpaired electrons), in ^{29}Si CP/MAS experiments (Fig. 5.3) the ^{29}Si spins derive spin polarization from nearby protons via static components of ^{29}Si - ^1H dipolar interactions. Then, in keeping with the popular view that elemental silicon particles are ‘capped’ on the surface by $-\text{H}$ and/or $-\text{OH}$ moieties, the observed CP-vs-DP ^{29}Si NMR differences can be understood on the basis that the ‘core’ of an *np*-Si particle consists of crystalline-like Si sites, which are spatially distant from any hydrogen atoms and hence unable to participate in ^1H - ^{29}Si CP. This ‘core’ is surrounded by a hydrogen-containing sheath in which the ^{29}Si nuclei can participate in ^1H - ^{29}Si CP.

Taking the typical *np*-Si particle diameter of about 50 nm, if one makes the oversimplified assumption of a spherical particle shape, a simple calculation yields the result that about 6% of the idealized *np*-Si particle is at the surface, within about 0.5 nm of the outer edge of the particle. According to this interpretation, the DP/MAS ^{29}Si spectrum of Figure 5.2 represents about 94% of the silicon sites in the particle, with the CP/MAS ^{29}Si spectra of Figure 5.3 representing the roughly 6% of the silicon sites that are ‘at the surface’. From this point on, until the Summary and Conclusions, this paper is concerned only with the surface region.

For purposes of spectral interpretation, each of the spectra of Figure 5.3 was simulated in terms of a set of peaks with line shapes that were either Gaussian (-14 ppm contribution) or Lorentzian (all other contributions). For each of the spectra of Figure 5.3, the use of a mixed (linear combination of Lorentzian and Gaussian) line shape for any of the signals did not improve the match between the experimental and simulated spectra. Pictorial details of these simulations are given in the Supporting Information. There it is

seen that the quality of the match between an experimental and a simulated spectrum, as represented by the weak intensity of the difference spectrum, is very good. Nevertheless, one should keep in mind the fact that, as is the case in such simulations of most functions with severely overlapping contributions ('peaks'), there is a substantial degree of arbitrariness in this kind of procedure, especially when signal-to-noise is limited, as it is in the present case. The relative intensities and line widths of the spectral contributions resulting from the simulations are summarized in Table 5.1.

No signal attributable to *c*-Si (centered at -79 ppm with a line width of about 1.3 ppm) can be found in any of these ^{29}Si CP/MAS NMR spectra of Figure 5.3. This indicates that the crystalline-like Si sites (Fig. 5.2) are essentially all spatially removed from any hydrogen atoms, hence unable to participate in $^1\text{H}\text{-}>^{29}\text{Si}$ CP.

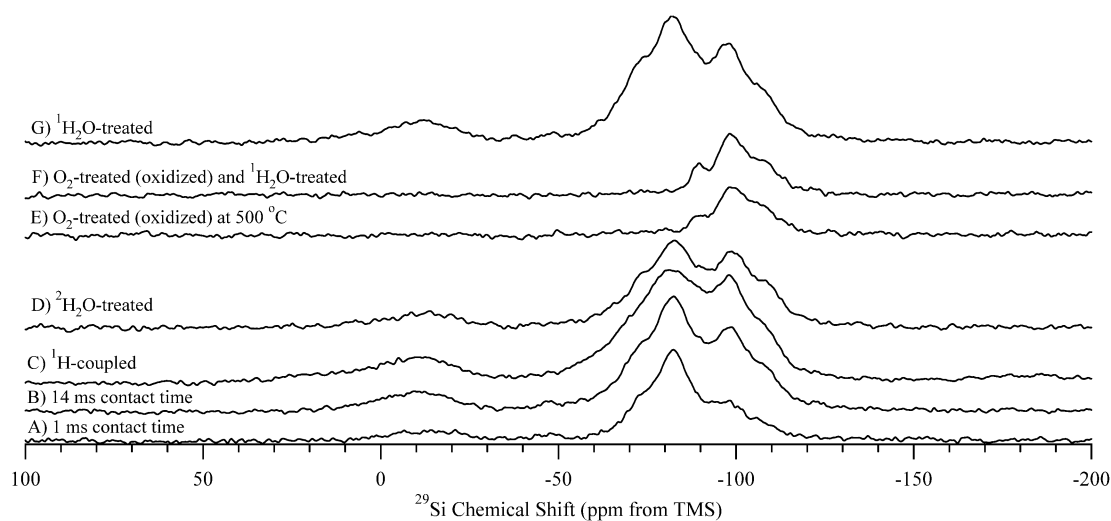


Figure 5.3. 71.5 MHz ^{29}Si CP/MAS spectra of samples based on *np*-Si. ^1H -decoupled, 7 kHz MAS and 14 ms CP contact time unless noted otherwise and evacuated at 150 °C. A) 1 ms contact time. B) 14 ms contact time. C) ^1H -coupled. D) $^2\text{H}_2\text{O}$ -treated. E) O_2 -treated (oxidized) at 500 °C. F) O_2 -treated (oxidized) and $^1\text{H}_2\text{O}$ -treated. G) $^1\text{H}_2\text{O}$ -treated.

Table 5.1. Parameters used in the simulations of ²⁹Si CP/MAS spectra of Figure 5.3^a

Sample (Figs.)		²⁹ Si Chemical Shift (ppm)						Total
		-14	-74	-83	-89	-99	-109	
1 ms CT (Fig. 5.3A)	Signal	73,	74,	250,	57,	92,	24,	540, (0.57)
	Intensity ^e , Line Width ^f , (intensity ratio) ^h	28, (0.43)	9, (0.44)	10, (0.93)	11, (0.67)	11, (0.38)	8, (0.37)	
14 ms CT (Fig. 5.3B)	Signal Intensity, Line Width	170, 28	170, 12	270, 10	85, 11	240, 12	65, 9	1000
¹ H coupled (Fig. 5.3C)	Signal Intensity, Line Width	150, 28	160, 24	390 ⁱ , 18	45, 12	220, 12	43, 7	1004
² H ₂ O treated (Fig. 5.3D)	Signal Intensity, Line Width	150, 26	155, 12	375, 12	30, 12	320, 12	100, 10	1130
500 °C O ₂ (Fig. 5.3E)	Signal Intensity, Line Width	0	0	0	20, 5	180, 10	80, 7	280
500 °C O ₂ / ¹ H ₂ O treated (Fig. 5.3F)	Signal Intensity, Line Width	0	0	0	30, 4	200, 10	80, 9	310

^a Unless otherwise specified, all spectra were obtained with a CP contact time (CT) of 14 ms. Some details about the deconvolutions are given in the Supporting Information.

^b Sample preparation or important parameter of the NMR experiment.

^c Table divisions given in terms of ppm refer to the position of the center of each spectral contribution represented.

^d Total (spectrum-wide) integrated intensity for this spectrum, normalized to 1000 for the spectrum of Fig. 5.3B.

^e Integrated signal intensity of this deconvoluted spectral contribution. Uncertainties estimated to be, for each case, about ±10% of the corresponding reported intensity.

^f Full width at half height of this deconvoluted spectral contribution. Uncertainties estimated to be, for each case, roughly ± 15 % of the corresponding reported line width.

^g Spectrum identity. Samples of A, B and C were *np*-Si that had been pentane-washed and evacuated at 150 °C. Spectra E – G were all obtained with CT = 14 ms.

^h Ratio of total (integrated) spectral intensities obtained with CT of 1 ms and 14 ms.

ⁱ 24% of the signal intensity of this peak is in MAS sidebands.

^1H MAS . 360 MHz ^1H MAS experiments were carried out, using 15 – 17 kHz spinning, on a variety of samples based on *np*-Si. The spectra are collected in Figures 5.4 and 5.5. For the reasons given above for caution in comparing MAS-determined chemical shifts with literature values (especially for liquids), one might expect analogous differences here, perhaps up to about 0.8 ppm.

^1H MAS spectra of samples that correspond to the ^{29}Si spectra of Figure 5.3 are shown in Figure 5.4; these figures also show the total ^1H content per gram for each sample. These ^1H contents were determined by ^1H NMR spin counting, using 1,3,5-trimethoxybenzene as an intensity reference.⁴¹ A repetition delay of 3 s was employed in the experiments yielding the spectra of Figures 5.4 and 5.5; this compares to numbers around 0.5 s, measured by the saturation-recovery method, for the ^1H T_1 values of these samples.

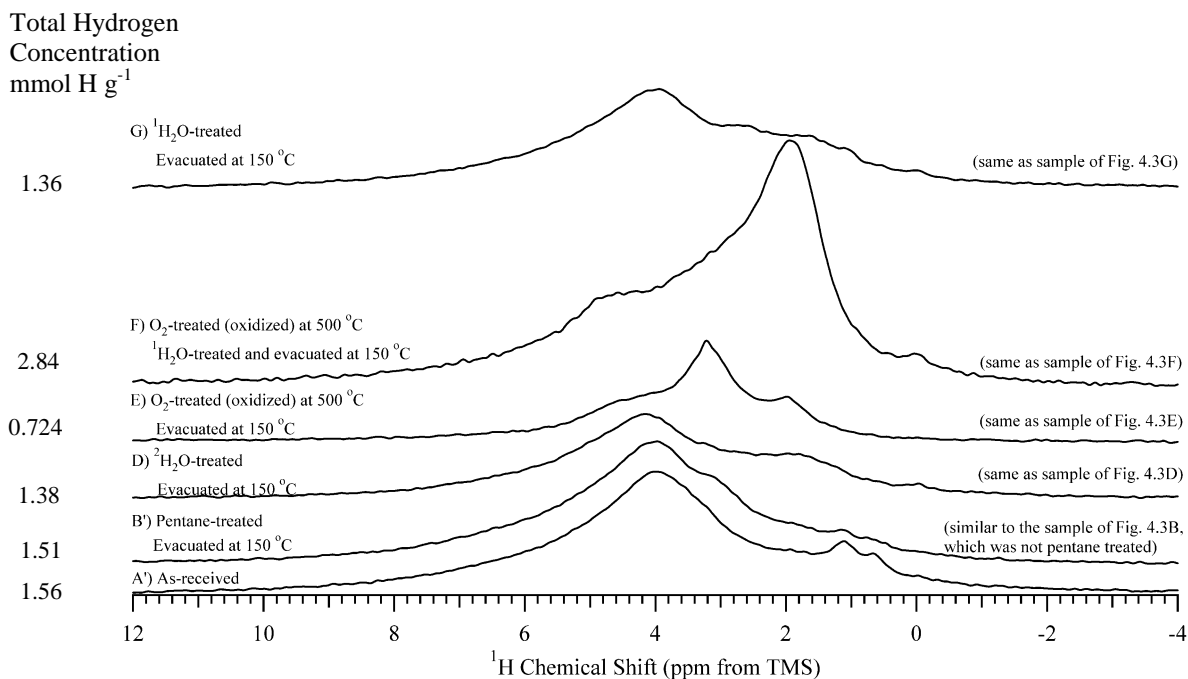


Figure 5.4. ^1H (360 MHz) MAS (15 – 17 kHz) NMR spectra of $np\text{-Si}$ and treated $np\text{-Si}$ samples. A') As-received $np\text{-Si}$. B') Pentane-treated and then evacuated at 150°C (similar to the sample of Fig. 5.3B, which was *not* pentane treated). D) $^2\text{H}_2\text{O}$ -treated, then evacuated at 150°C (same as sample of Fig. 5.3D). E) O_2 -treated (oxidized) at 500°C , then evacuated at 500°C (same as sample of Fig. 5.3E). F) O_2 -treated (oxidized) at 500°C , then $^1\text{H}_2\text{O}$ -treated and evacuated at 150°C (same as sample of Fig. 5.3F). G) $^1\text{H}_2\text{O}$ -treated, then evacuated at 150°C (same as sample of Fig. 5.3G). All spectra scaled so that the total area is proportional to H g^{-1} value for each sample.

Examination of the ^1H MAS spectra in Figure 5.4 reveals that there is ^1H NMR intensity -- as peaks, shoulders or 'wings' -- at chemical shifts spanning the range from about 7 ppm to about 0 ppm. These spectra and those of Figure 5.5 were analyzed via deconvolution/simulation based on up to nine peaks or contributions; not all nine components are represented in any one spectrum. Table 5.2 collects the results of these simulations.

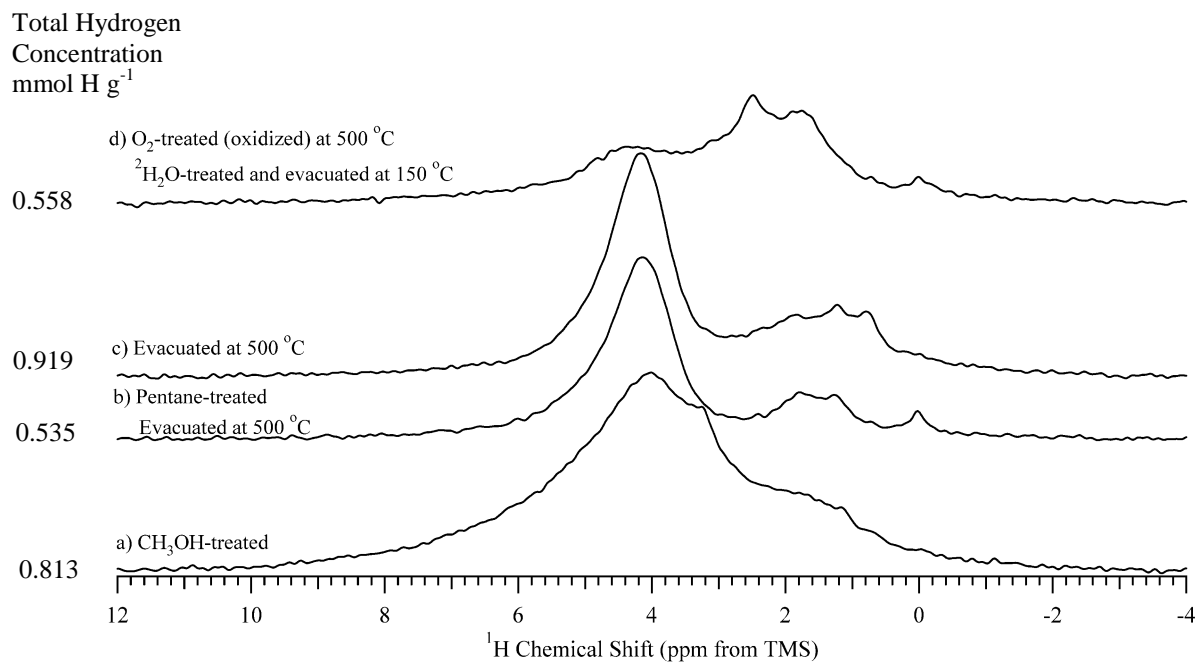


Figure 5.5. ¹H (360 MHz) MAS (15 – 17 kHz) NMR spectra of *np*-Si and treated *np*-Si samples. a) CH₃OH-treated. b) Pentane-treated, then evacuated at 500 °C. c) Evacuated at 500 °C. d) O₂-treated (oxidized) at 500 °C, then ²H₂O-treated, then evacuated at 150 °C. All spectra scaled so that the total area is proportional to the H g⁻¹ value for each sample.

Table 5.2. Summary of the Signal Areas of the Simulation/Deconvolutions of ^1H MAS Spectra of Figures 5.4 and 5.5.

Sample (Figs.)	^1H Chemical Shift (ppm)								
	6.0	4.8	4.5	3.9	3.3	3.1	2.2	1.1	0.0
CH_3OH (5.6a)	44	31	48	32	35	7	21	26	0
oxidized & $^2\text{H}_2\text{O}$ (5.6d)	16	18	12	10	17	0	37	54	5
oxidized & $^1\text{H}_2\text{O}$ (5.5F)	42	158	85	66	68	0	178	249	8
$^2\text{H}_2\text{O}$ (5.5D)	75	75	70	40	39	0	39	75	4
$^1\text{H}_2\text{O}$ (5.5G)	60	48	84	48	48	0	48	72	3
pentane & 500 °C evacuated (5.6b)	13	19	86	11	0	0	0	26	7
500 °C evacuated (5.6c)	13	17	122	0	0	0	9	103	13
500 °C oxidized (5.5E)	23	19	15	23	89	0	15	31	2
pentane & 150 °C evacuated (5.5B')	93	46	110	76	56	0	32	41	0
as-received (5.5A')	60	42	68	101	130	0	40	26	3

150 °C Evacuated *np*-Si. Figure 5.3B shows the proton-decoupled ^{29}Si CP/MAS NMR spectrum of *np*-Si evacuated at 150 °C. The simulated spectrum of Figure 5.3B (Supporting Information) consists of six heavily overlapping signals, each with a unique chemical shift, whose spectral characteristics are summarized in Table 5.1. The signal at -14 ppm, in addition to differing from the other contributions in line shape, also differs from the rest in the spectrum simulation of Figure 5.3B in having a significantly larger line width of 28 ppm, compared with 9 to 12 ppm for the others. This suggests that the -14 ppm peak/contribution likely represents more than one site structure on the surface. This -14 ppm signal appears in all of the spectra of Figure 5.3 for samples that have *not* been subjected to the oxidative treatment with O_2 at 500 °C. No spinning sidebands are observed for any signal. It is worth noting that -74 ppm and -84 ppm are very close to the -74 ppm and -85 ppm values that have been reported for $(\text{Si-O})_2\text{Si}(\text{H})\text{OH}$ and $(\text{Si-O})_3\text{Si-H}$ structures, respectively, from data on solid and/or liquid samples of

(R-O)₃Si-H or its polysiloxane polymers and/or modified silicas.^{48,49} Here the symbol, *Si*, stands for silicon atoms that are bonded or bridged to the silicon atom, **Si**, on whose chemical shift we are focused, and it is understood that *Si* has additional bonds that are understood but not shown.

In examining the ²⁹Si CP/MAS results and attempting to assign specific spectral regions to specific local surface structures, an important strategy is to establish which spectral regions are identified with silicon atoms with directly attached (bonded) hydrogen atoms, i.e., with Si-H bonds. In solid-state ²⁹Si NMR, one is drawn to experimental approaches that depend predictably on the strengths of ²⁹Si-¹H dipole-dipole interactions. One such approach is to examine the effect of changing the CP contact time (CT), since the rate of ¹H->²⁹Si CP transfer of polarization depends strongly on the strength of pertinent ¹H-²⁹Si dipolar interactions, which in turn are inversely proportional to the cube of the ¹H-²⁹Si inter-nuclear distance.

Comparison of the spectra of Figures 5.3A and 5.3B, which come from spectra obtained with 1 ms and 14 ms, respectively, provides an opportunity to assess *qualitatively* the CP dynamics. Of course, to characterize the CP dynamics *quantitatively*, one would need a more extensive study of the relevant spin dynamics (most commonly, a variable-contact-time study). To the extent that the 14 ms spectra represent, at least qualitatively, the relative populations of surface sites, the integrated intensities shown in Table 5.1 indicate that the surface populations fall in the order: -83 ppm > -99 ppm > -14 ppm ~ -73 ppm > -89 ppm > -109 ppm. As expected, in the comparison highlighted here, seen both in the spectra and in the corresponding parameters in Table 5.1 that were derived from them, the overall integrated spectral intensity of the spectrum measured

with CT = 14 ms (Fig. 5.3B) is substantially larger than for the spectrum obtained with CT = 1 ms (Fig. 5.3A). This intensity difference is very strong for the spectral contributions at around -14 ppm, -89 ppm, -99 ppm and -109 ppm, and not so large for the contribution at -83 ppm. This pattern seems reasonable if one assumes that the -83 ppm contribution comes from Si-H sites, for which CP transfer will be well developed already at 1 ms of CP contact, and will have less to gain from a CT increase to 14 ms than will CP at silicon atoms with no directly bonded hydrogen. The CP responsible for those spectral contributions, at -14 ppm, -89 ppm, -99 ppm and -109 ppm, benefit more markedly from the longer CP CT; therefore, the corresponding silicon sites center on silicon atoms with no directly-bonded hydrogens. The -73 ppm spectral contribution, for reasons not yet understood, also shows a strong response to increasing CT. The ratio of integrated spectral intensities obtained with CT values of 1 ms and 14 ms, also given in Table 5.1, are consistent for the spectral contributions at -89 ppm, -99 ppm and -109 ppm with results published on fumed silica³¹ and silica gel³⁵, derived from variable-contact-time data for silica peaks identified as $(Si-O)_2Si(OH)_2$, $(Si-O)_3SiOH$ and $(Si-O)_4Si$ contributions, respectively.

Figure 5.3C shows the *proton-coupled* ^{29}Si CP/MAS NMR spectrum of pentane-treated *np*-Si evacuated at 150 °C. The spectrum was recorded *without proton decoupling*. Even without proton decoupling, the ^{29}Si - 1H dipolar coupling will be largely averaged by 7 KHz MAS; but the ^{29}Si - 1H J coupling will still be operative. Comparing the spectra of Figures 5.3B and 5.3C, and the corresponding parameters in Table 5.1, one sees that the line widths of the spectral contributions at about -74 ppm and -83 ppm have roughly doubled when the proton decoupler was turned off, while the line widths of the

-14 ppm, -89 ppm, -99 ppm and -109 ppm spectral contributions are almost unchanged. The large increases in line widths observed are likely due to a combination of residual dipolar broadening and unresolved ^{29}Si - ^1H J coupling in silicon sites with directly-bonded hydrogens. $J_{\text{Si-H}}$ in silatrane, $\text{N}(\text{CH}_2\text{CH}_2\text{O})_3\text{Si-H}$, is reported to be 270 Hz.⁵⁰ These patterns are consistent with the following tentative assignments: -14 ppm, no directly-bonded hydrogens (at least for the main structural constituent contributing to this spectral region); -74 ppm, $(\text{Si-O})_2\text{Si}(\text{H})\text{OH}$ (substantial uncertainty associated with the CT dependence described above); -83 ppm, $(\text{Si-O})_3\text{Si-H}$; -89 ppm, $(\text{Si-O})_2\text{Si}(\text{OH})_2$; -99 ppm, $(\text{Si-O})_3\text{Si-OH}$; -109 ppm, $(\text{Si-O})_4\text{Si}$.

Another dipole-based technique that is used routinely in ^{13}C MAS NMR to establish C-H connectivity, or at least proximity (assuming rapid MAS or atomic-level motions do not largely average the relevant dipole-dipole interactions), is interrupted decoupling or *dipolar dephasing* technique.⁵¹ In this technique a period, often about 40 μs is inserted between the end of the period generating ^{13}C magnetization from CP and the beginning of proton-decoupled ^{13}C detection. During this ‘interrupt’ period, ^{13}C magnetization of carbons that are strongly impacted by dipolar interaction(s) with one or more protons (e.g., directly-bound ^{13}C - ^1H in relatively rigid structures) is rapidly dephased and strongly attenuated in the observed ^{13}C spectrum. Figure 5.6 shows the result of applying the dipolar-dephasing technique to the CP/MAS ^{29}Si spectrum of *np*-Si evacuated at 150 °C. From the spectra shown for various durations of the dephasing period, one sees that magnetization of the region around -80 ppm (including both the -74 ppm and -83 ppm spectral contributions) dephases much more rapidly than for other regions of the spectrum, indicating that the ^{29}Si resonance(s) giving rise to spectral

intensity in that region are due to silicon sites that are in closest proximity to H, e.g., Si(-H)_n sites.

The integrated intensities of each contribution in the deconvolutions of the spectra in Figure 5.6 for each dephasing period (interrupt period) were analyzed in terms of a single decaying exponential function (almost certainly an oversimplification); this analysis yielded the following time constants describing the decays of the various ²⁹Si CP/MAS spectral contributions: -14 ppm, 0.18 ms; -73 ppm, 0.085 ms; -83 ppm, 0.060 ms; -89 ppm, 0.10 ms; -99 ppm, 0.35 ms; -109 ppm, 0.50 ms. The dipolar-dephasing time constants for the -89 ppm and -99 ppm contributions are in reasonable agreement with published values for the (Si-O)₂Si(-OH)₂ and (Si-O)₃Si-OH peaks, respectively, derived from dipolar-dephasing experiments on fumed silica⁵² and are in the same order (albeit with much smaller values) as are dipolar-dephasing constants derived from silica gel data.⁵³

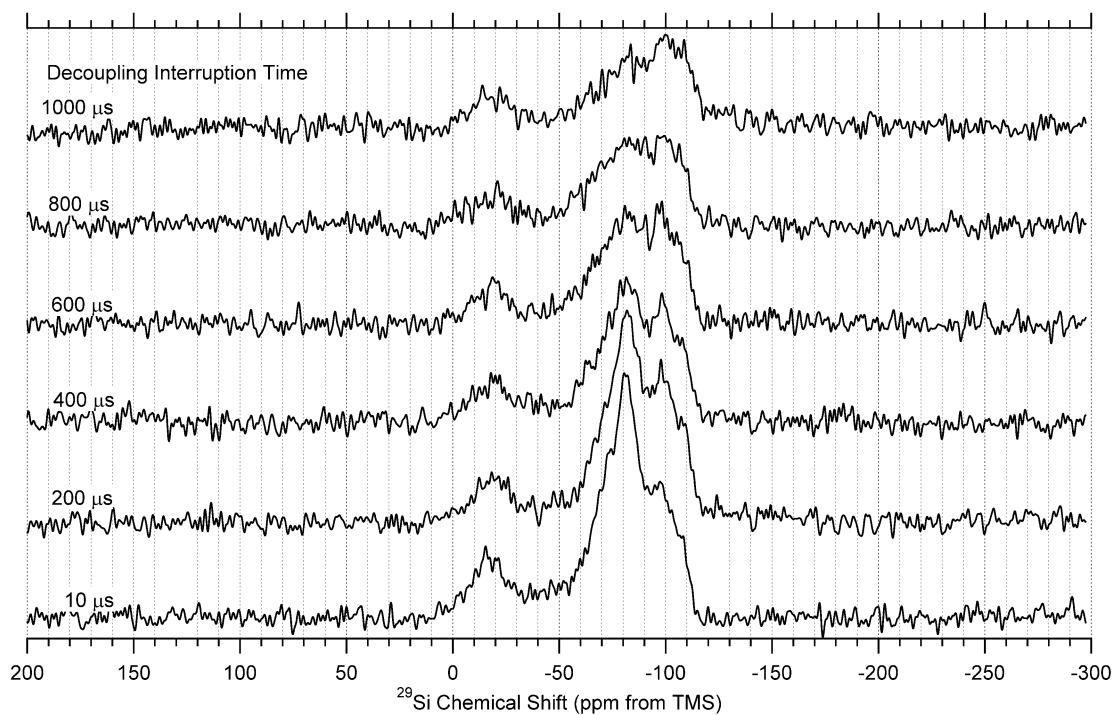


Figure 5.6. Dipolar-dephasing ^{29}Si CP/MAS spectra of np -Si for various interrupt periods, τ , as indicated. A 5.0 kHz MAS speed was used.

The six dipolar-dephasing time constants given above are qualitatively consistent with what one would expect in terms of the chemical shift assignments suggested above and in interpretations below, i.e., $(\text{HO-})_n\text{Si}(-\text{Si})_m(-\text{O-Si})_{4-m-n}$ for -14 ppm, $(\text{Si-O-})_2\text{Si}(\text{H})\text{OH}$ for -73 ppm, $(\text{Si-O-})_3\text{Si-H}$ for -83 ppm, $(\text{Si-O-})_2\text{Si}(-\text{OH})_2$ partially responsible for spectral density around -89 ppm, $(\text{Si-O-})_3\text{Si-OH}$ partially responsible for spectral intensity around -99 ppm and $(\text{Si-O-})_4\text{Si}$ at least partially responsible for spectral intensity around -109 ppm. The last three structures correspond to silica-like surface sites.

Assignments and Quantum Mechanical Calculations of ^{29}Si Chemical Shifts. As an aid in identifying specific ^{29}Si chemical shifts with specific structural moieties, ^{29}Si

chemical shift calculations were performed, using the GAUSSIAN 03 computational package,³² on model clusters that represent possible local structures that may contribute to the overall surface structure of *np*-Si. The results, which cover an experimental range of about 70 ppm, are summarized in Table 5.3. As a prior calibration of the ²⁹Si chemical shift calculations on model surface clusters, ²⁹Si chemical shifts were calculated on several Si-containing molecules (molecules 1-8 in Table 5.3) and compared with the values obtained experimentally. In the interest of saving computational time in the calculations on possible structural models for specific surface sites of *np*-Si, the **Si**OSiH₃ moiety was used instead of **Si**OSi(-O-Si)₃ to represent a Si-O-Si bridge between the silicon atom for which $\delta^{29}\text{Si}$ is calculated (represented in bold face) and another silicon atom in the structure. The relatively close agreement for model compounds 6, 7 and 8 in Table 5.3 with experimental results on silica gel indicates that this is a reasonable approximation.

For the cases in which calculated results can be compared with reliable experimental data, it seems that the calculated ²⁹Si chemical shifts are commonly more positive (lower shielding) by a few ppm than those obtained experimentally. From the results for compounds 1 – 9 in the table, a plot of $\delta^{29}\text{Si}(\text{calc})$ vs $\delta^{29}\text{Si}(\text{exp})$ shows a very smooth correlation.

Table 5.3. Calculated and Experimentally Obtained ^{29}Si Chemical Shifts (Si atom in bold face), relative to $(\text{CH}_3)_3\text{Si}$.

	Molecule	$\delta^{29}\text{Si}$ (ppm)		Molecule	$\delta^{29}\text{Si}$ (ppm)	
		Exp.	Calc.			Calc.
1	Si H ₄	-93 ^a	-91	11	HSi (-SiH ₃) ₂ -OSiH ₃	-18
2	H ₃ Si -SiH ₃	-103 ^b	-96	12	(HO-) Si (-SiH ₃) ₃	-14
3	H ₂ Si (-SiH ₃) ₂	-115 ^b	-105	13	(HO-) ₂ Si (-SiH ₃) ₂	-12
4	HSi (-SiH ₃) ₃	-136 ^b	-124	14	H ₂ Si (-OSiH ₃) ₂	-44
5	Si (-SiH ₃) ₄	-165 ^b	-159	15	H ₂ Si (-SiH ₃)-OSiH ₃	-37
6	(HO-) ₂ Si (-OSiH ₃) ₂	-89 ^c	-86	16	(HO-) Si (-SiH ₃) ₂ -OSiH ₃	-2
7	HO-Si(-OSiH ₃) ₃	-99 ^c	-93	17	(HO-) Si (-SiH ₃)(-OSiH ₃) ₂	-49
8	Si (-OSiH ₃) ₄	-109 ^c	-100	18	(HO-) ₂ Si (-SiH ₃)-OSiH ₃	-37
9	HSi (-OSiH ₃) ₃		-77	19	HO(H) Si (-SiH ₃) ₂	-22
10	HSi (-SiH ₃)(-OSiH ₃) ₂		-14	20	HO(H) Si (-SiH ₃)-OSiH ₃	-24
				21	HO(H) Si (-OSiH ₃) ₂	-71

a Ref. ⁵⁴

b Ref. ⁵⁵

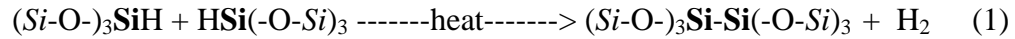
c Ref. ⁵⁶ and ref. ⁵⁷

Si-containing compounds that might represent the structures of sites on a *np*-Si surface are included in Table 5.3. The model cluster $\text{H-Si}(-\text{OSiH}_3)_3$ (molecule 9) represents hydrogen-terminated Si atoms bonded to three bridging oxygen atoms, $\text{H-Si}(-\text{OSi})_3$, and the ^{29}Si chemical shift for the model cluster is calculated to be -77 ppm. This chemical shift is close to the experimentally observed chemical shift of the contribution/peak at about -80 ppm, which was tentatively assigned above to some kind(s) of $\text{Si}(-\text{H})_n$ moiety, specifically -83 ppm for $(\text{Si-O})_3\text{Si-H}$ (and -73 ppm for $(\text{Si-O})_2\text{Si}(\text{H})\text{OH}$). The experimentally observed -73 ppm chemical shift is close to the result calculated for molecule 21 in the table (-71 ppm), providing additional support for this chemical shift assignment to the $\text{HO}(\text{H})\text{Si}(-\text{O-Si})_2$ structure.

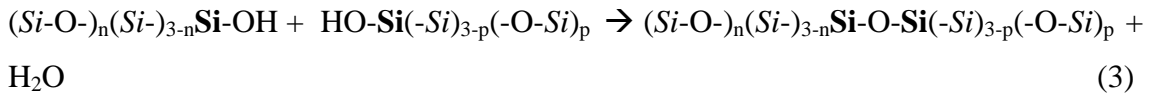
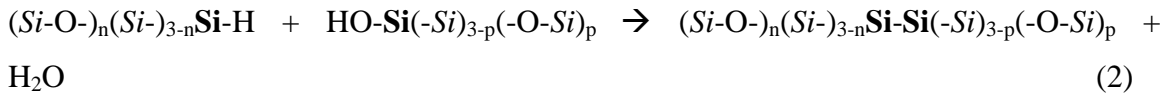
Among the calculated results of Table 5.3, only those for model molecules 10, 11, 12, 13, 16, 19 and 20 are within 20 ppm of -14 ppm, the position of the broad, low-intensity peak in Figure 5.3. Of these seven model molecules in Table 5.3, numbers 10, 11, 19 and 20 are tentatively ruled out because they contain **Si-H** bonds. This leaves, as possible assignments, the structures, $\text{HO-Si}(-\text{Si})_3$, $(\text{HO-})_2\text{Si}(-\text{Si})_2$ and $\text{HO-Si}(-\text{Si})_2(-\text{O-Si})$, which are modeled in Table 5.3 by model molecules 12, 13 and 16; these three structural possibilities are all covered by the formula, $(\text{HO})_n\text{Si}(-\text{Si})_m(-\text{OSi})_{4-n-m}$, which is taken as the structural assignment for the -14 ppm peak. The breadth of the -14 ppm peak may indicate that more than one of these structures contributes to this peak.

The ^1H MAS spectra of as-received *np*-Si (Fig. 5.4A') and *np*-Si that has been treated with pentane and then evacuated at 150 °C (Fig. 5.4B') consist of a broad peak centered at about 4 ppm, with some intensity in the regions around 3.3 ppm, 2.2 ppm, 1.1 ppm and 0.7 ppm; the overall (spectrum-wide) intensities for the two samples are

essentially the same. Such patterns (aside from the small features at 0.7 ppm, which are not included in the simulations from which Table 5.2 was generated) are represented by substantial numbers for several contributions in the deconvolution results given in Table 5.2. The samples evacuated at 500 °C (Fig. 5.5b and Fig. 5.5c) show a sharpening of the main pattern that includes a maximum at about 4.3 ppm and more sharply defined intensity pattern in the 0 to 2 ppm range. These *np*-Si samples that had been evacuated at 500 °C experience substantial decreases in overall spectral intensity, more than 1/3 for the 500 °C-evacuated sample (Fig. 5.5c) and about 2/3 for the pentane-treated/500 °C-evacuated sample (Fig. 5.5b) relative to samples that have not been heated at 500 °C (Fig. 5.4A' and 5.4B). One can speculate that this ¹H NMR intensity loss centered around 4 ppm could be due to some kind of dehydrogenation reaction of the type represented in eq. 1 or a



condensation process of the types represented in eq. 2 or, more likely, eq. 3.



Processes of these types could also account for the loss of CP/MAS ²⁹Si intensity centered at about -80 ppm, identified above as sites of the type, (Si-O)₃Si-H (or (Si-O)₂Si(H)OH), in the spectra of *np*-Si that has been heated at 500 °C in the presence

of O₂ (*vide infra*); however, this change in spectra associated with O₂ treatment at 500 °C could also be associated with an oxidative process of the type represented in eq. 4 and eq. 5.

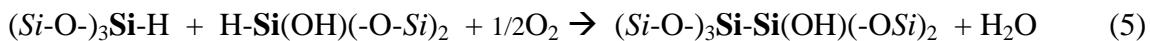
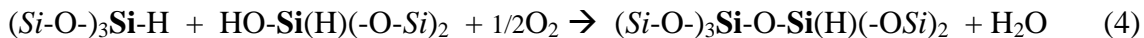


Figure 5.7 shows the ¹H MAS NMR spectra (obtained by the DEPTH-echo sequence) of the *np*-Si sample (pentane-treated and evacuated at 150 °C) as a function of total echo time, $\tau = 2\tau_1 + 2\tau_2$. In this technique, probe background signals are suppressed and the isotropic part of the ¹H NMR chemical shift refocuses for any time τ , while the anisotropic part of the ¹H chemical shift can refocus completely only when τ is equal to $2n\tau_r$, where n is an integer and τ_r is the MAS rotor period. The inhomogeneous part of dipolar interactions (¹H-¹H and ¹H-²⁹Si) are also refocused, along with the CSA, each time that τ equals an even number of rotor periods ($2n\tau_r$). Thus, it is the *homogeneous* contribution of dipolar interactions in effect over the τ period that preferentially attenuates the transverse magnetization of the protons that are most strongly involved in homogeneous dipolar interactions. This is roughly analogous to the well-known ¹³C-¹H dipolar dephasing technique applied routinely in solid-state ¹³C NMR and represented in Figure 5.4 for ²⁹Si NMR or to CRAMPS ¹H experiments with dipolar dephasing.⁵⁸ In obtaining the spectra shown in Figure 5.8, the parameter τ was varied from 280 μ s to

3940 μs , keeping τ equal to $2n\tau_r$. Only spectra obtained for $\tau = 280, 840, 1520$ and 2520 μs are shown in Figure 5.7.

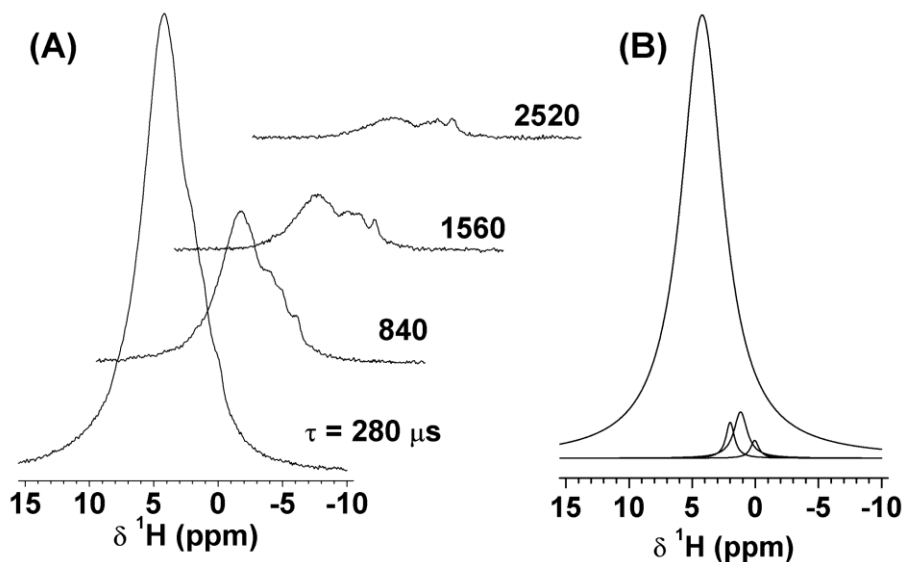


Figure 5.7. A) ^1H (360 MHz) MAS Depth-Echo spectra of a *np*-Si sample evacuated at 150 $^{\circ}\text{C}$ as a function of total echo time, $\tau = 2\tau_1 + 2\tau_2$. Spectra were obtained by the DEPTH-echo pulse sequence with 1024 repetitions, shown without amplitude scaling (true amplitude); MAS rate = 14.3 kHz. B) Deconvolution/simulation contributions to the ^1H NMR spectrum obtained at $\tau = 280$ μs .

The ^1H NMR spectra obtained with various τ values were deconvolved into four Lorentzian-shape peaks, centered at 4.4 ppm, 2.2 ppm, 1.4 ppm and 0.1 ppm (shown in Fig. 5.7B only for $\tau = 280$ μs). For $\tau = 280$ μs , the peak centered at 4.4 ppm accounts for approximately 95% of the total spectral area (Fig. 5.7B). According to these deconvolutions, the corresponding magnetization decay of each of the four contributions was represented by an exponential function with a time constant, T_2' . The T_2' values estimated for those four contributions individually by fitting the four contribution

intensities from the simulations/ deconvolutions to exponential decays are: 4.4 ppm, 0.39 ms; 2.2 ppm, 0.59 ms; 1.4 ppm, 0.73 ms; 0.1 ppm, 0.78 ms.

As can be seen in Figure 5.7A and the T_2' values given above, the lowest-shielding ^1H MAS contribution decays by dipolar dephasing faster than do the higher-shielding contributions, which indicates that the protons that contribute to the lower-shielding side of the spectrum are involved in stronger homogeneous ^1H - ^1H dipolar effects than those on the higher-shielding side. If the 1.4 ppm peak is assigned to protons of isolated hydroxyl groups, then its larger T_2' value can perhaps be explained partially by the motion of those protons about a Si-O bond. It has been shown previously that hydroxyl groups of a silica gel surface execute fast (with reference to a 5×10^{-6} s time scale defined by deuterium quadrupole interactions), limited-extent rotational (librational) diffusion about the Si-O axis; the librational motions can be restricted by hydrogen bonds. The librational motions of *isolated* hydroxyl groups are less restricted than those of hydrogen-bonded hydroxyls (the distance between a pair of isolated hydroxyl groups is longer than that of a hydrogen-bonded hydroxyl pair), which results in smaller ^1H - ^1H dipolar interactions for the isolated hydroxyls.

The small 2.2 ppm contribution in Figure 5.7B can tentatively be assigned to protons of hydrogen-bonded hydroxyls. The librational motions of hydrogen-bonded hydroxyls are more restricted than those of isolated hydroxyl groups.⁵⁹ It is known that hydrogen bonding produces a proton chemical shift to lower shielding and that the magnitude of this effect increases with stronger hydrogen bonding.^{60,61} Thus, strongly hydrogen-bonded hydroxyls give a ^1H NMR signal in the lower-shielding region and are less mobile. The dominant peak at 4.4 ppm cannot be interpreted primarily in the same

way, because the results discussed above and in the ^2H MAS results presented below indicate that SiOH moieties do *not* constitute a major portion of silicon surface sites.

A plausible identification of at least a major portion of the 4.4 ppm spectral contribution is hydrogens that are *directly* bonded to silicon. This kind of hydrogen is essentially immobile, in contrast to the protons of hydroxyl groups, which execute librational motions about the inter-nuclear Si–O axis, at least for those that are not strongly hydrogen bonded. The ^1H - ^1H dipolar interaction between immobile protons is not averaged by atomic-level motion and is expected to be stronger than that between 'mobile' hydroxyl protons of a comparable inter-hydrogen distance. The spectral contribution at 4.4 ppm accounts for approximately 95 % of the total spectral area in the depth-echo measurements on *np*-Si for $\tau = 280$ us. The ^{29}Si CP/MAS spectra and related theoretical calculations of ^{29}Si chemical shifts (*vide supra*) also indicate that a major fraction of the surface sites in *np*-Si samples that have not been intentionally oxidized consists mainly of hydrogen-terminated silicon, instead of silanol (SiOH) groups (*vide infra*). This is consistent with our interpretation that the peak at about 4.4 ppm arises mainly from hydrogen atoms that are *directly* bonded to surface silicon atoms.

Water-Treated Samples. Figure 5.3D shows the proton-decoupled ^{29}Si CP/MAS NMR spectrum of $^2\text{H}_2\text{O}$ -treated *np*-Si (then evacuated at 150 °C), obtained using a 14 ms CP contact time. This spectrum shows the effect of a chemical treatment that provided an opportunity for replacement of any readily-exchangeable hydrogens on the surface (e.g., of Si-OH) by deuterium atoms. One sees no substantial evidence in Figure 5.3D or Table 5.1 of a removal of ^1H sources for ^1H - $\rightarrow^{29}\text{Si}$ CP. The simulated spectrum for Figure 5.3D (Supporting Information) consists of five heavily overlapping signals whose spectral

characteristics are summarized in Table 5.1. Figure 5.3G shows the proton-decoupled ^{29}Si CP/MAS NMR spectrum of *np*-Si that has been treated with $^1\text{H}_2\text{O}$ (then evacuated at 150 °C), also obtained using a 14 ms CP contact time. This spectrum is very similar to the spectra of 150 °C-evacuated *np*-Si (Fig. 5.3B) and the sample treated with $^2\text{H}_2\text{O}$ (Fig. 5.3D). While there are some significant, albeit not dramatic, differences in the intensities of the six contributions (Table 5.1) for comparable positions in the spectra of Figures 5.3B, 5.3D and 5.3G, the line widths of comparable contributions are identical (within experimental error). The similarities among the ^{29}Si CP/MAS spectra of Figures 5.3B, 5.3D and 5.3G are so strong that the only chemically significant conclusion that seems obvious is that *OH groups are not dominant on the surfaces of these samples*; otherwise, the effects of ^1H — ^2H exchange would have been more dramatic in these MAS spectra based on ^1H — ^{29}Si CP.

The total NMR-determined proton concentrations of the samples of Figure 5.4A' (as-received) and Figure 5.4B' (pentane-treated and evacuated at 150 °C) are essentially the same as each other; also the total ^1H concentrations of the samples of Figure 5.4D ($^2\text{H}_2\text{O}$ -treated and evacuated at 150 °C) and Figure 5.4G ($^1\text{H}_2\text{O}$ -treated and evacuated at 150 °C) are the same as each other. Within this quartet of samples/spectra, the pentane-treated and as-received samples have about 12 % higher total ^1H intensity than the samples that have been treated with water. This difference is primarily manifested in the intensity contributions around 3.9 ppm and 3.3 ppm and is partially compensated by larger contributions around 1.1 ppm for the water-treated samples. If there were a dominant contribution of Si-OH moieties on the untreated (or pentane-treated/150 °C evacuated) sample, the main effect of $^2\text{H}_2\text{O}$ treatment would be hydrogen exchange and a

reduced Si-O-¹H intensity (probably at about 1.1 ppm);⁵² such a spectral difference is not observed between Figures 5.4D and 5.4G, or between Figure 5.4D and Figures 5.4A' or 5.4B'. These results are consistent with indications from the ²⁹Si NMR results (and ²H MAS results, *vide infra*) that there is not a dominant contribution of Si-OH moieties on the un-oxidized *np*-Si surface.

An obvious difference between the ¹H NMR spectra of ²H₂O-treated and ¹H₂O-treated samples would have been expected, and is *not* observed, if water treatment had resulted in simple hydrolysis of strained Si--Si linkages, e.g., as represented by eq. 6 (where it is understood that the symbol, *Si*, stands for a silicon atom to which there are

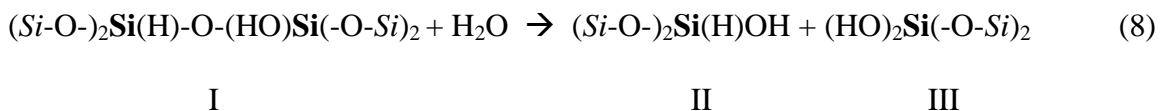


additional bonds that are not shown explicitly). A direct oxidation by water (eq. 7) seems



unlikely.

Table 5.2 indicates that the main ¹H NMR effect of *np*-Si treatment with ¹H₂O (Fig. 5.4G) and ²H₂O (Fig. 5.4D) is a transfer of ¹H intensity from the region around 3.9 ppm (near the assignment for (Si-O-)₃Si-H to about 1.1 ppm (near previous assignment for isolated silanols of a silica system).⁵² This decrease in 3.9 ppm intensity and increase in 1.1 ppm intensity could be explained by some kind of chemical reaction of the type shown in eq. 8 (assuming that the hydride ¹H chemical shift of structure II is substantially different from that in structure I).



It may be noteworthy that the ^{29}Si CP/MAS spectra (Figures 5.3D and 5.3G) of samples that correspond to those of the proton MAS spectra of water-treated samples (Figures 5.4D and 5.4G) do not show any convincing evidence that supports (or refutes) the speculative chemistry embodied in eqs. 6 – 8, or of *any* substantive chemical changes.

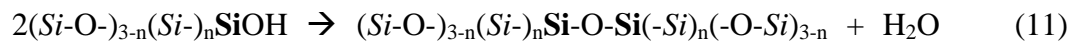
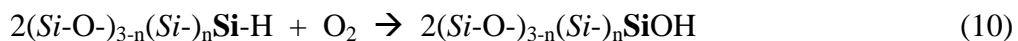
Treatment of *np*-Si that had been pentane-treated and evacuated at 150 °C with another hydroxyl-containing species, CH_3OH (Fig. 5.5a), yielded a *lower* overall hydrogen concentration and a broader, reduced-intensity pattern around the central maximum, between about 3 ppm and about 5 ppm. This overall reduction of hydrogen concentration seems unlikely to be due to an extraction of non-polar organic contaminants, as these would be more effectively extracted by pentane; Figures 5.4 and 5.5 show no evidence that this occurs. One can speculate that the reduced-intensity pattern around 4 ppm might be due to some kind of chemical reaction involving the reduction of CH_3OH (eq. 9).



Oxidized np-Si. Figure 5.3E shows the proton-decoupled ^{29}Si CP/MAS NMR spectrum of oxidized *np*-Si (evacuated at 500 °C), obtained using a 14 ms CP contact time. The most obvious differences between the spectra of oxidized (Fig. 5.3E) and unoxidized (Fig. 5.3B) samples are a general loss of overall spectral intensity and peak narrowing in the spectrum of the oxidized sample and the total loss of intensity in the -14 ppm, -73 ppm and -83 ppm regions. One sees in Table 5.1 that only the spectral contributions centered at -89 ppm, -99 ppm and -109 ppm survive in the oxidation (the -109 ppm contribution may actually increase); as pointed out above, these are the same

chemical shifts at which one finds the Q2, Q3 and Q4 moieties in the ^{29}Si CP/MAS spectra of silicas;¹² hence, such assignments may account for at least portions of the spectral density in these chemical shift regions in the spectra of Figure 5.3. In terms of the tentative structural assignment given above, these results indicate that the 500 °C O₂ treatment converts all **Si-Si** and **Si-H** bonds, and some of the **Si-OH** moieties, at the surface primarily to **Si-O-Si** linkages and that **Si** of most of these new **Si-O-Si** linkages are sufficiently remote from hydrogen atoms to be incapable of exhibiting observable ^1H - ^{29}Si CP.

In the ^1H MAS spectra, the three samples with a history of intentional oxidation (O₂ treatment at 500 °C), represented in Figures 5.4E, 5.4F and 5.5d, show dramatic changes relative to as-received (Fig. 5.4A') or pentane-treated/150 °C-evacuated (Fig. 5.4B') *np*-Si samples. The sample that was subjected to *only* 500 °C O₂ treatment, with no subsequent water treatment (Fig. 5.4E), shows a sharp decrease (roughly half) in total ^1H concentration; Table 5.2 indicates that this intensity loss is distributed throughout the entire spectrum, except perhaps for the contribution at about 3.3 ppm. This broad intensity loss would be consistent with the occurrence of oxidation processes that convert **Si-H** moieties into **Si-O-Si** moieties or into **Si-OH** groups (eq. 10), followed by condensation of adjacent silanols (eq.11).



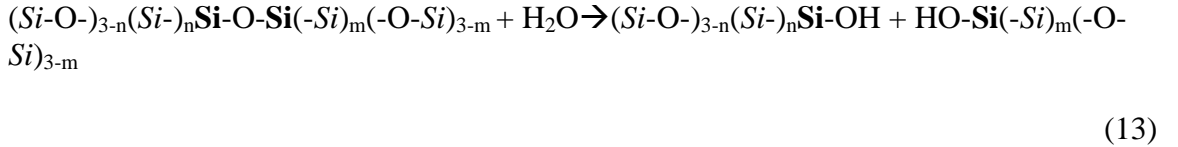
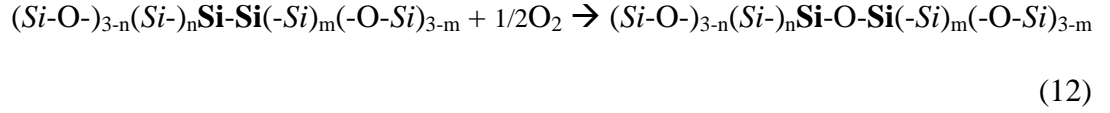
The fact that, as seen in Table 5.2, the 1.1 ppm intensity in Figures 5.4A' and B' (as-received or pentane-treated/150 °C evacuated, respectively) is largely retained in Figure

5.4E (500 °C oxidized) is consistent with the idea that dehydration is more difficult with isolated silanols (about 1.1 ppm) than with hydrogen-bonded silanols (> 2 ppm). In light of the ^{29}Si CP/MAS (Fig. 5.3) results on the – 109 ppm spectral contribution, It would appear that $n = 0$ may be the most probable interpretation.

Oxidized-and- $^1\text{H}_2\text{O}$ -treated np-Si. Figure 5.3F shows the proton-decoupled ^{29}Si CP/MAS NMR spectrum of oxidized-and- $^1\text{H}_2\text{O}$ -treated (then evacuated at 150 °C) *np-Si*, obtained using a 14 ms CP contact time. This spectrum is very similar to that of the *np-Si* sample that had been only oxidized (no $^1\text{H}_2\text{O}$ treatment, Fig. 5.3E), as shown numerically in Table 5.1. Thus, the ^{29}Si CP/MAS experiments provide no obvious evidence of any major chemical transformation due to the water treatment.

The ^1H MAS spectrum of the $^2\text{H}_2\text{O}$ -treated/oxidized sample (Figure 5.5d) shows a huge decrease in total ^1H concentration (relative to that of the pentane-treated/150 °C evacuated *np-Si* sample, manifested across the entire spectrum, except for a small intensity increase in the 1 – 3 ppm range (Table 5.2). The large total ^1H intensity loss upon oxidation of *np-Si* with O_2 at 500 °C (Fig. 5.4E) is more than restored when this sample is treated with $^1\text{H}_2\text{O}$ (Fig. 5.4F); in fact the total ^1H content of this sample is almost double that of the as-received or pentane-treated/150-°C-evacuated samples. From Table 5.2 one sees that this increase in total ^1H content, relative to the spectrum of the O_2 -oxidized-only sample (Fig. 5.4E), is spread across the spectrum, except for a modest decrease in spectral intensity around 3.3 ppm, and is especially large in the 4.8 ppm, 2.2 ppm and 1.1 ppm contributions. These intensity increases with $^1\text{H}_2\text{O}$ treatment are consistent with surface reactions of the types represented in equations 12 and 13 for the oxidation and water-treatment steps and imply that the 4.8 ppm, 2.2 ppm and 1.1 ppm

chemical shifts may be associated with structures of the $(Si-O-)_{4-n-p}(Si-)_pSi(-OH)_n$ type on the surface. For $p = 0$,



these proton chemical shifts have been assigned in previous work on silica gel to protons in isolated silanols (Si-OH) (1.1 ppm),⁵² silanols with hydrogen-bonds (Si-OH...HO-Si) of modest strength (roughly 1.2 to 2.0 ppm) and silanol networks with very strong hydrogen bonds (> 2 ppm). The modest decrease in 3.3 ppm intensity in the ¹H MAS spectrum upon ¹H₂O treatment suggests that one effect of water treatment on the *np*-Si sample that had been oxidized at 500 °C could be a ‘sharpening’ of the spectral intensity patterns on both sides of 3.3 ppm, ostensibly due to reduced structural heterogeneity in the associated site structures, reducing the overlapped intensity into the 3.3 ppm region.

Comparison of the spectra of oxidized samples that have been treated with ¹H₂O (Fig. 5.4F) and with ²H₂O (Fig. 5.5d) emphasizes structural changes that are generated by oxidation, but show up in ¹H NMR spectra of water-treated samples only when the water is ¹H₂O. This comparison shows larger spectral intensity contributions across the entire spectrum (Table 5.2) of Figure 5.4F, compared with Figure 5.5d, with the largest differences for the contributions at 4.8 ppm, 2.2 ppm and 1.1 ppm. Since one expects that the main source of differences between these ¹H MAS spectra will be associated with readily ‘exchangeable’ SiOH moieties, these results indicate that these three spectral regions perhaps correspond to structural sites of the type, $(Si-O-)_{4-n}Si(-OH)_n$ (most

probably with $n = 1$ and 2). These chemical interpretations are consistent with the corresponding ^{29}Si CP/MAS results, which show a dramatic loss of intensity centered at about -80 ppm ($(\text{Si-O})_3\text{Si-H}$ and $(\text{Si-O})_2\text{Si(H)OH}$) for oxidized samples (Fig. 5.3E for oxidized-only and Fig. 5.3F for oxidized and $^1\text{H}_2\text{O}$ -treated). The combination of results suggests that most likely there are essentially no Si-Si bonds remaining at the surface after O_2 oxidation at 500°C .

^2H MAS NMR. Since useful information regarding the chemical status of hydrogen atoms is often available from deuterium NMR, especially from comparing the NMR results of samples that differ only in their ^1H -vs- ^2H contents, ^2H MAS experiments were carried out on *np*-Si samples that had been a) treated (exchanged?) with $^2\text{H}_2\text{O}$ (the same kind of sample as in Figures 5.3D and 5.4D) and b) oxidized and then treated with $^2\text{H}_2\text{O}$ (the same kind of sample as in Figure 5.5d). While most solid-sample ^2H NMR experiments are carried out on static samples, focusing on the relationship between line shape and motion,⁵⁹ our experiments employed MAS because of anticipated signal-to-noise problems in static-sample ^2H NMR spectra of the samples of this study. The results are shown in Figure 5.8, along with a ^2H MAS spectrum of $^2\text{H}_2\text{O}$ -treated silica gel. This figure shows a ^2H NMR signal that is roughly twice as intense for the oxidized/ $^2\text{H}_2\text{O}$ -exchanged sample (Fig. 5.8b) as for the sample that had not been subjected to the $\text{O}_2/500^\circ\text{C}$ oxidation procedure (Fig.5.8c). Since the effect of $^2\text{H}_2\text{O}$ treatment is viewed substantially in terms of ^2H -for- ^1H exchange in silanol groups at the surface, this result implies that the $500^\circ\text{C}/\text{O}_2$ treatment roughly doubles the silanol concentration on the *np*-Si surface. In comparison with the spectrum of a $^2\text{H}_2\text{O}$ -exchanged silica gel (Fig. 5.8a),

one sees that the silanol concentrations represented in Figure 5.8 are very small compared with those of silica gel.⁶²

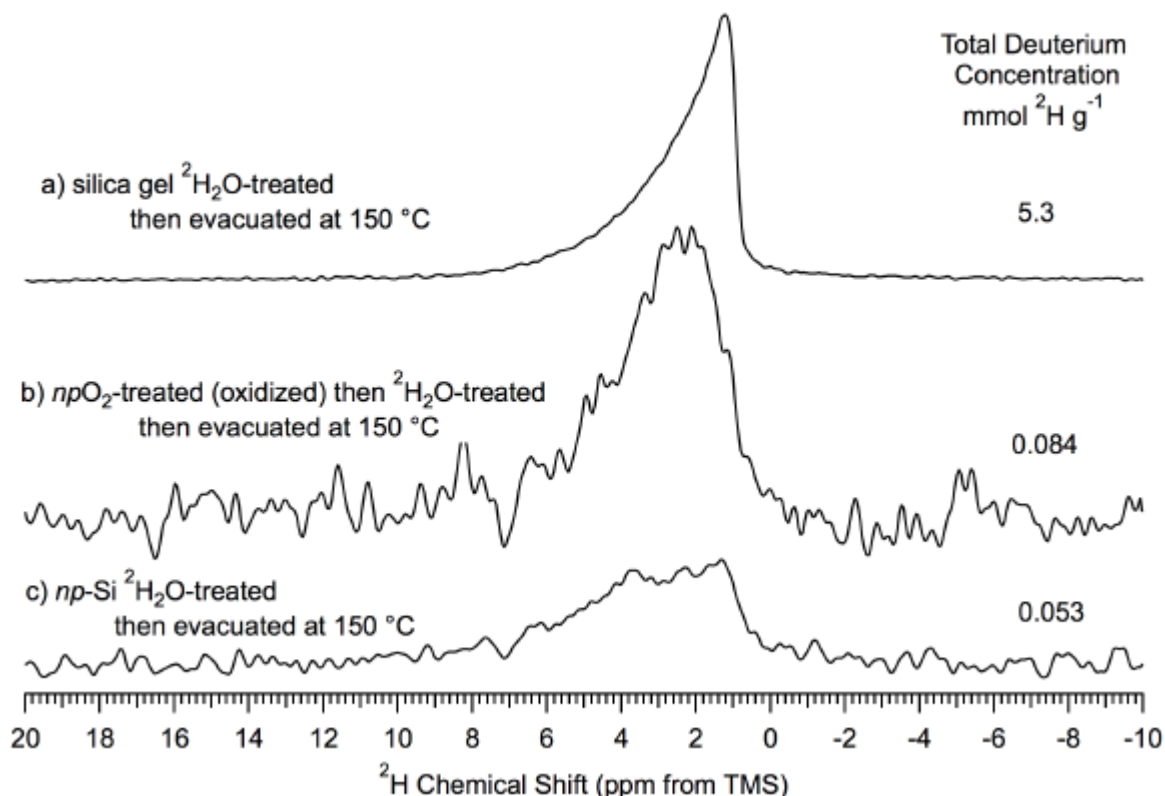


Figure 5.8. ^2H (55 MHz) MAS (7 kHz) NMR spectra of treated silica gel and treated *np*-Si samples. a) $^2\text{H}_2\text{O}$ -treated then 150 °C evacuated silica gel. b) 500 °C O_2 -treated then $^2\text{H}_2\text{O}$ -treated then 150 °C evacuated *np*-Si. c) $^2\text{H}_2\text{O}$ -treated then 150 °C evacuated *np*-Si. The total deuterium concentration was determined by comparison of the numerical integral of each spectrum referenced to the proton concentration for dry silica gel determined by Li et. al. The *np*-Si spectra are scaled so that the total area (integral) is proportional to the $^2\text{H g}^{-1}$ value for each sample. The silica gel spectrum is scaled similarly except for a factor of 100.

Since the OH concentration of dry silica gel has previously been determined,⁶² from the ²H NMR intensities of Figure 5.8 and the weights of the individual samples, the OH concentration of *np*-Si and oxidized *np*-Si could be estimated as 0.053 and 0.110 mmol H g⁻¹, respectively, assuming that all of the ²H₂O-exchangeable hydrogen on *np*-Si-based samples are readily exchangeable silanol moieties. Comparing these two numbers with the hydrogen contents given in Table 5.2, one can conclude that about 3 % of the hydrogen content of pentane-treated/150 °C evacuated *np*-Si is in surface silanols and for the oxidized *np*-Si sample this percentage is about 6 %. *These numbers are an order of magnitude smaller than what one would expect from the integrated ²⁹Si CP/MAS NMR intensities summarized in Table 5.1.* These results confirm the tentative interpretation above that SiOH moieties constitute a significant, but not large portion of surface sites in the *np*-Si samples of this study.

Summary and Conclusions

The combination of ²⁹Si and ¹H chemical shift results and time-domain NMR data based on magnetic dipole-dipole interactions yields a self-consistent interpretation of the surface chemical structure of *np*-Si and various treated *np*-Si samples. This combination of NMR-derived information leads to a picture of the surface of as-received *np*-Si as consisting of a dominant contribution of a Si-H layer, with a small but significant contribution of surface silanols; these types of ‘surface sites’ are connected to a crystal-like silicon core by Si-O-Si bridges and Si-Si bonds. It has been reported that a hydrogen-terminated silicon surface is oxidized under ambient air at room temperature to form a SiO₂-type layer.⁷ Apparently, when a H-Si(-Si)₃ surface is oxidized, the formation of

$\text{H-Si}(-\text{Si})_n(-\text{O-Si})_{3-n}$ is energetically favored, compared to formation of a surface hydroxyl, e.g., $\text{H-O-Si}(-\text{Si})_3$, configuration. Thus, the broad -80 ppm contribution that is dominant in the ^{29}Si CP/MAS spectra of samples that have not been deliberately oxidized (500 °C O_2) is assigned to a monohydride silicon atoms that are each bonded to three bridging oxygen atoms, $(\text{Si-O})_3\text{Si-H}$ (with intensity probably centered at about -85 ppm), and to the related $(\text{Si-O})_2\text{Si(H)OH}$ sites (with intensity centered at about -75 ppm); these assignments are supported by quantum mechanical calculations of ^{29}Si chemical shifts. Such calculations also suggest that a ^{29}Si CP/MAS spectral contribution at about -14 ppm in the spectrum of unmodified *np*-Si may be due to structures of the type $(\text{Si-O})_2\text{Si(H)}(-\text{Si})$ and/or $(\text{Si-O})\text{Si(H)}(-\text{Si})_2$. Comparing integrated intensities of the various contributions to the ^{29}Si CP/MAS spectra of 150 °C evacuated *np*-Si (Table 5.1) suggest the following qualitative order of site populations: $(\text{Si-O})_3\text{Si-H} >$ sites with the same ^{29}Si chemical shift (- 99 ppm) as $(\text{Si-O})_3\text{SiOH}$ (which is included as a small contribution) $>$ $(\text{HO-})_n\text{Si}(\text{Si})_m(-\text{OSi})_{4-m-n} \sim (\text{Si-O})_2\text{Si(H)OH} >$ sites with the same ^{29}Si chemical shift (-89 ppm) as $(\text{Si-O})_2\text{Si}(-\text{OH})_2$ (which is included as a small contribution) $>$ sites with the ^{29}Si chemical shift of $(\text{Si-O})_4\text{Si}$ (-109 ppm). A combination of ^1H and ^2H MAS experiments provide strong evidence for small contributions of silanol groups, along with the dominant Si-H sites, on the surface of unmodified *np*-Si; these silanol sites are dramatically increased by deliberate oxidation (500 °C O_2). These experiments provide a self-consistent view of the generation or elimination of silanols under hydrolysis, oxidation and condensation reactions. Some of the speculative chemical processes that may be relevant in accounting for the NMR data involve transfer of the elements of H_2 . This fact is of interest in connection with the

suggestion that silicon-based materials may hold promise in the search for efficient hydrogen storage.²³ This also supports the beginning hypothesis in Chapter 2 that the surface (Si)₃-Si-H structures react with O₂ in the atmosphere, as opposed to atmospheric moisture.

Acknowledgements.

The authors gratefully acknowledge the donation of the (Si-O)₃Si-H polymer by Prof. Junior E. Sandoval of Universidad Del Valle, Cali, Columbia, the partial support of this research from the National Science Foundation (Grant No. CHE-9021003), helpful discussions with Professor Bruce Parkinson during the early stages of this work and technical assistance from Drs. Sandeep Kohli and Patrick McCurdy.

References:

- (1) Zou, J.; Sanelle, P.; Pettigrew, K. A.; Kauzlarich, S. M. *J. Cluster Sci.* **2006**, *17*, 565.
- (2) Chopra, N.; Gavalas, V. G.; Hinds, B. J. *Anal. Lett.* **2007**, *40*, 2067.
- (3) O'Farrell, N.; Houlton, A.; Horrocks, B. R. *Int. J. Nanomed.* **2006**, *1*, 451.
- (4) Neiner, D.; Kauzlarich, S. M. *Chem. Mater.* **2010**, *22*, 487.
- (5) Lemke, B. P.; Haneman, D. *Phys. Rev. B* **1978**, *17*, 1893.
- (6) Ubara, H.; Imura, T.; Hiraki, A. *Solid State Commun.* **1984**, *50*, 673.
- (7) Tamao, K.; Kumada, M.; Takahashi, T. *J. Organomet. Chem.* **1975**, *94*, 367.
- (8) Sunada, T.; Yasaka, T.; Takakura, M.; Sugiyama, T.; Miyazaki, S.; Hirose, M. *Jpn. J. Appl. Phys.* **1990**, *29*, L2408.
- (9) Mayeri, D.; Phillips, B. L.; Augustine, M. P.; Kauzlarich, S. M. *Chem. Mater.* **2001**, *13*, 765.
- (10) Takagoshi, K.; Nagai, I.; Ishitani, A.; Kuroda, H. *J. Appl. Phys.* **1988**, *64*, 2516.
- (11) Zou, J.; Baldwin, R. K.; Pettigrew, K. A.; Kauzlarich, S. M. *Nano Lett.* **2004**, *4*, 1181.
- (12) Reimer, J. A.; Vaughan, R. W.; Knights, J. C. *Phys. Rev. Lett.* **1980**, *44*, 193.
- (13) Reimer, J. A.; Vaughan, R. W.; Knights, J. C. *Phys. Rev. B* **1981**, *24*, 3360.
- (14) Tsuboi, T.; Sakka, T.; Ogata, Y. H. *Phys. Rev. B* **1998**, *58*, 13863.
- (15) Petit, D.; Chazalviel, J. N.; Ozanam, F.; Devreux, F. *App. Phys. Lett.* **1997**, *70*, 191.
- (16) Pietrass, T.; Bifone, A.; Roth, R. D.; Koch, V. P.; Alivisatos, A. P.; Pines, A. J. *J. Non-Cryst. Solids* **1996**, *202*, 68.
- (17) Shao, W. L.; Shinar, J.; Gerstein, B. C. *Phys. Rev. B* **1990**, *41*, 9491.
- (18) vanderHeiden, E. D.; Ohlsen, W. D.; Taylor, P. C. *J. Non-Cryst. Solids* **1984**, *66*, 115.
- (19) Yates, J. T. *J. Phys-Condens Mat.* **1991**, *3*, S143.
- (20) Tardif, F.; Chabli, A.; Danel, A.; Rochat, N.; Veillerot, M. *J. Electrochem. Soc.* **2003**, *150*, G333.
- (21) Tatsumura, K.; Watanabe, T.; Yamasaki, D.; Shimura, T.; Umeno, M.; Ohdomari, I. *Phys. Rev. B* **2004**, *69*, 085212.
- (22) Verdi, L.; Miotello, A.; Kelly, R. *Thin Solid Films* **1994**, *241*, 383.
- (23) Levit, M. H. *Spin Dynamics Basics of Nuclear Magnetic Resonance*; John Wiley & Sons, Ltd: West Sussex, England, 2001.
- (24) Pines, A.; Gibby, M. G.; Waugh, J. S. *J. Chem. Phys.* **1973**, *59*, 569.
- (25) Cory, D. G.; Ritchey, W. M. *J. Magn. Reson.* **1988**, *80*, 128.
- (26) Dutta, B. N. *Phys. Stat. Sol.* **1962**, *2*, 984.
- (27) Peacor, D. R. *Z. Kristallogr.* **1973**, *138*, 274.
- (28) Shimura, T.; Misaki, H.; Umeno, M.; Takahashi, I.; Harada, J. *J. of Cryst Growth* **1996**, *166*, 786.

- (29) Duncan, J. L. *J. Mol. Spectro.* **1976**, *60*, 225.
- (30) Cullity, B. D. *Elements of X-ray Diffraction*, 2nd ed.; Addison-Wesley: Reading, MA, 1978.
- (31) Corminboeuf, C.; Heine, T.; Weber, J. *Chem. Phys. Lett.* **2002**, *357*, 1.
- (32) Maciel, G. E.; Haw, J. F.; Chuang, I.; Hawkins, B. L.; Early, T. A.; McKay, D. R.; Petrakis, L. *J. Am. Chem. Soc.* **1983**, *105*, 5529.
- (33) Fink, M. J.; DeYoung, D. J.; West, R. *J. Am. Chem. Soc.* **1983**, *105*, 1070.
- (34) Alemany, L. B.; Grant, D. M.; Alger, T. D.; Pugmire, R. J. *J. Am. Chem. Soc.* **1983**, *105*, 6697.
- (35) Liu, C. H. C.; Maciel, G. E. *J. Am. Chem. Soc.* **1996**, *118*, 5103.
- (36) Chuang, I.; Kinney, D. R.; Bronnimann, C. E.; Maciel, G. E. *J. Phys. Chem.* **1992**, *96*, 4027–4034.
- (37) Lower, R.; Vongehr, M.; Marsmann, H. C. *Chemiker-Zeitung* **1975**, *99*, 33.
- (38) Hahn, J. Z. *Naturforsch., B: Chem. Sci.* **1980**, *35*, 282.
- (39) Marsmann, H. C. *Z. Naturforsch., B: Chem. Sci.* **1974**, *B29*, 495.
- (40) Maciel, G. E.; Sindorf, D. W. *J. Am. Chem. Soc.* **1980**, *102*, 7606.
- (41) Bronnimann, C. E.; Hawkins, B. L.; Zhang, M.; Maciel, G. E. *Anal. Chem.* **1988**, *60*, 1743.
- (42) Kobayashi, T.; DiVerdi, J. A.; Maciel, G. E. *J. Phys. Chem. C* **2008**, *112*, 4315.
- (43) Berglund, B.; Vaughan, R. W. *J. Chem. Phys.* **1980**, *73*, 2037.
- (44) Schroter, B.; Rosenberger, H.; Hadzi, D. *J. Mol. Struct.* **1983**, *96*, 301.
- (45) Sindorf, D. W.; Maciel, G. E. *J. Phys. Chem.* **1983**, *87*, 5516.
- (46) Li, J.; DiVerdi, J. A.; Maciel, G. E. *J. Am. Chem. Soc.* **2006**, *128*, 17093.
- (47) Liao, W.-S.; Lee, S.-C. *J. Appl. Phys.* **1996**, *80*, 1171.

Supporting Information

Deconvolution of the ^{29}Si CP/MAS Spectra of Figure 5.3

Each figure in this section is presented in three parts - the experimental spectrum, the calculated spectrum based on the deconvolved spectra contributions and the difference between the first two. Figure 5.9 shows the experimental and simulated proton-decoupled ^{29}Si CP/MAS NMR spectra of *np*-Si evacuated at 150 °C. The experimental spectrum, as with all but the next spectrum shown, was taken with a CP contact time (CT) of 14 ms.

The calculated spectrum of Figure 5.9 consists of six heavily overlapping signals, each with a unique chemical shift, whose spectral characteristics are summarized in Table 5.1. One signal centered at -14 ppm has a Gaussian line shape, while the five others at -74, -84, -91, -100 and -109 ppm have Lorentzian line shapes. The use of a mixed (linear combination of Lorentzian and Gaussian) line shape for any of the signals did not improve the match between the experimental and simulated spectra. The signal at -14 ppm also differs from the rest in having a significantly larger line width of 28 ppm, compared with 9 to 12 ppm for the others. No spinning sidebands are observed for any signal.

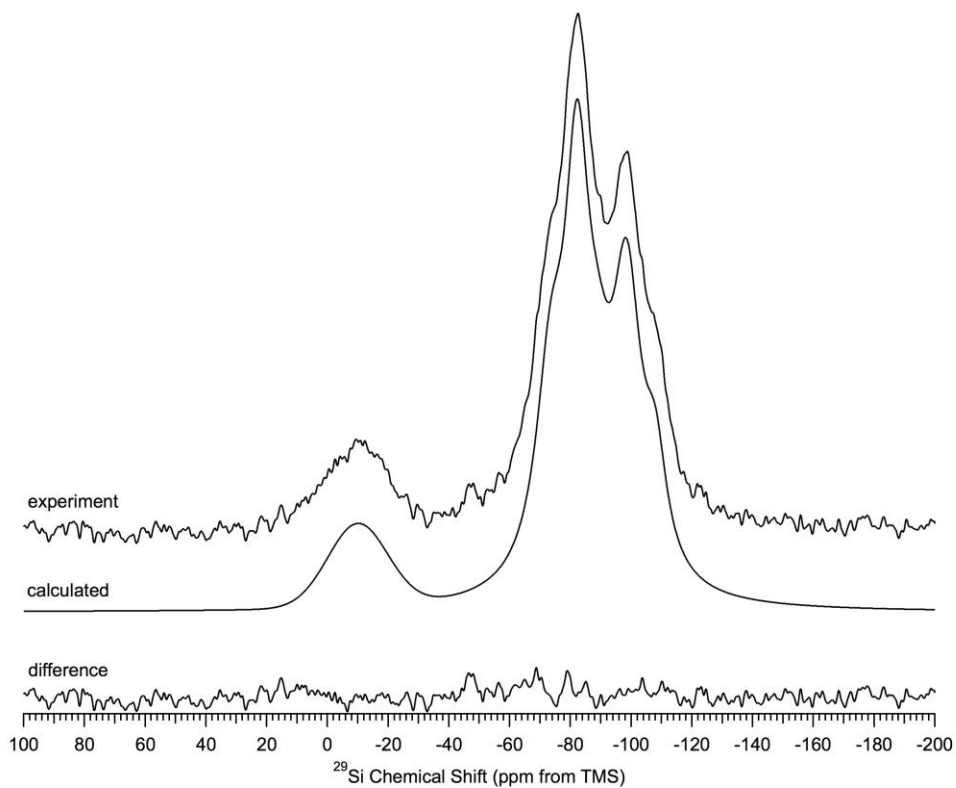


Figure 5.9. Experimental and simulated (calculated) proton-decoupled ^{29}Si (71.5 MHz) CP/MAS NMR spectra of *np*-Si evacuated at 150 °C and their difference spectrum. A CP contact time of 14 ms and a MAS speed of 7.0 kHz were used.

Figure 5.10 shows the experimental and simulated proton-decoupled ^{29}Si CP/MAS spectra of *np*-Si evacuated at 150 °C, taken with a 1.0 ms CP contact time. The spectral characteristics for this calculated spectrum are also tabulated in Table 5.1. The line shape and line width of each signal in Figure 5.10 are very similar with the values of the corresponding signals in Figure 5.9, with some minor variations attributable to experimental error and the exception of the signal at -74 ppm, where the short CP contact time instance is several ppm narrower than the long CP contact instance. Although the difference is significant, it is small and its significance uncertain.

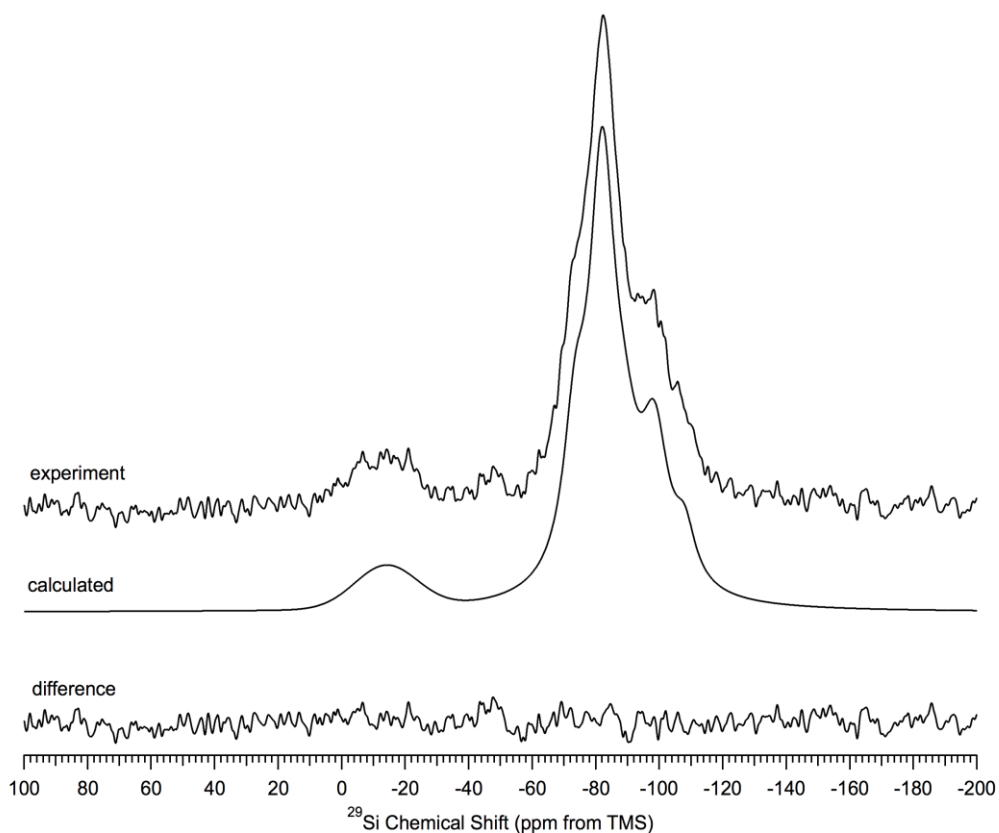


Figure 5.10. Experimental and simulated proton-decoupled ^{29}Si (71.5 MHz) CP/MAS NMR spectra of *np*-Si evacuated at 150 °C and their difference spectrum. A CP contact time of 1.0 ms and a MAS speed of 7.0 kHz were used.

Figure 5.11 shows the experimental and simulated proton-coupled ^{29}Si CP/MAS NMR spectra of *np*-Si evacuated at 150 °C. The experimental spectrum was recorded with proton coupling and using the same long CP contact time as used in Figure 5.9 (14 ms).

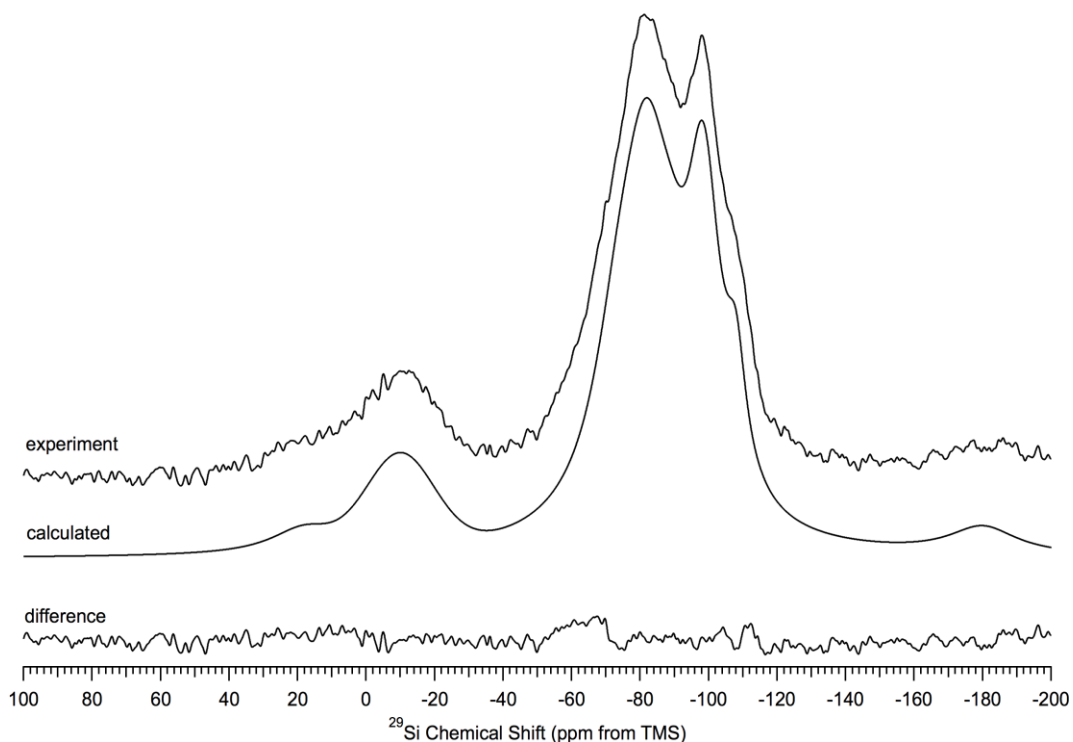


Figure 5.11. Experimental and simulated proton-coupled ^{29}Si (71.5 MHz) CP/MAS NMR spectra of *np*-Si evacuated at 150 °C and their difference spectrum. A CP contact time of 14 ms and a MAS speed of 7.0 kHz were used.

Figure 5.12 shows the experimental and simulated proton-decoupled ^{29}Si CP/MAS NMR spectra of $^2\text{H}_2\text{O}$ -treated *np*-Si, obtained using a long CP contact time (14 ms). The simulated spectrum of Figure 5.12 consists of five heavily overlapping signals

whose spectral characteristics are summarized in Table 5.1. The signal at -14 ppm exhibits a Gaussian line shape. Signals at -74, -83, -89, -99 and -108 ppm have Lorentzian line shapes. The use of a mixed line shape for any of the signals did not improve the match between the experimental and simulated spectra.

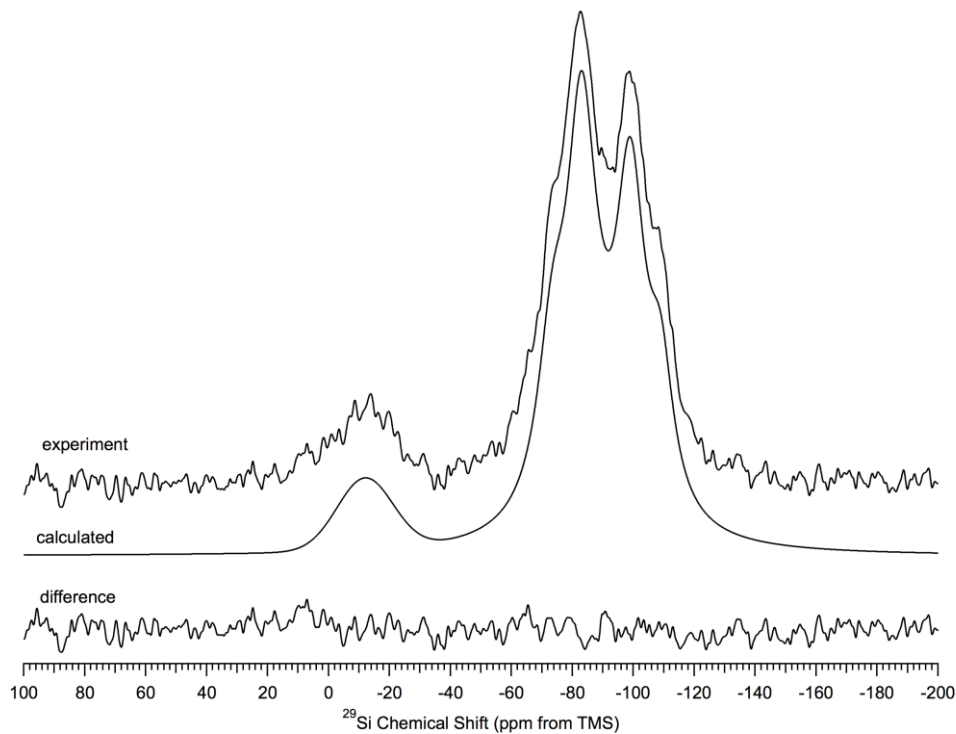


Figure 5.12. Experimental and simulated ^{29}Si (71.5 MHz) CP/MAS proton decoupled NMR spectra of $^2\text{H}_2\text{O}$ -treated *np*-Si and their difference spectrum. A CP contact time of 14 ms and a MAS speed of 7.0 kHz were used.

Figure 5.13 shows the experimental and simulated proton-decoupled ^{29}Si CP/MAS NMR spectra of oxidized *np*-Si, obtained using a long CP contact time (14 ms). The simulated spectrum of Figure 5.13 consists of three heavily overlapping signals whose spectral characteristics are summarized in Table 5.1. The signals at -89, -99 and -109 ppm have Lorentzian line shapes. All of the other signals (-14, -74 and -83 ppm) seen

in the spectra of the 150 °C evacuated samples are absent in the spectrum of this sample. The use of a mixed line shape for any of the signals did not improve the match between the experimental and simulated spectra.

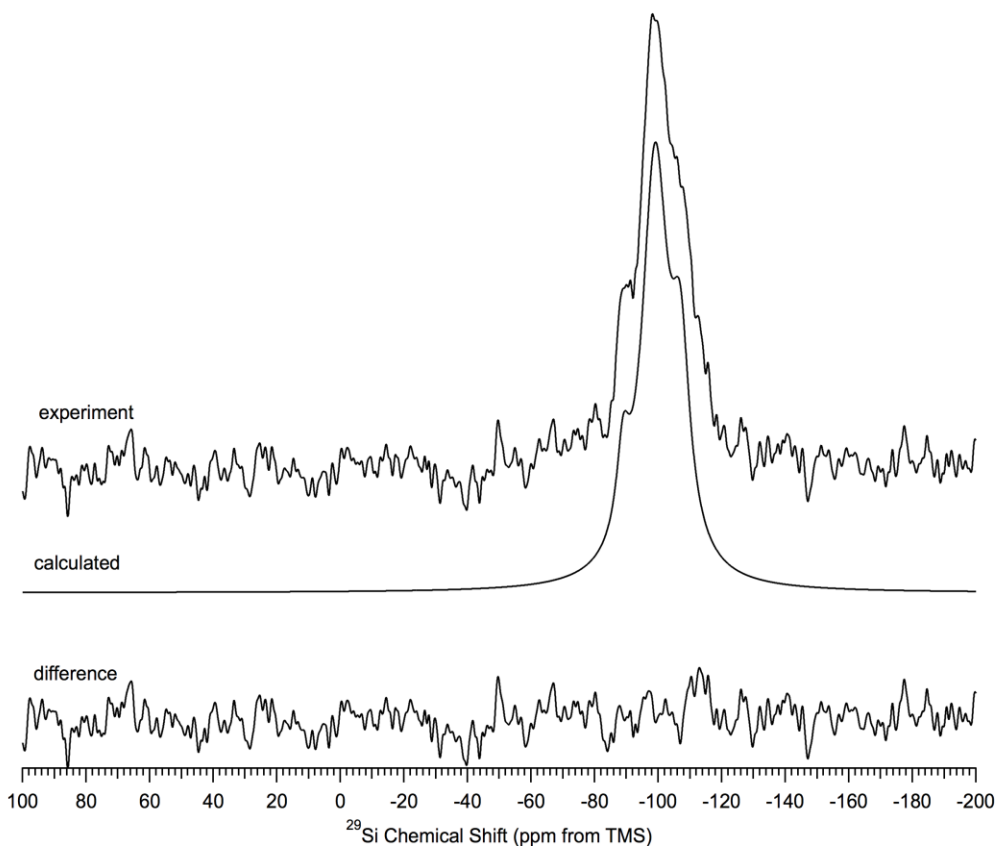


Figure 5.13. Experimental and simulated proton decoupled ^{29}Si (71.5 MHz) CP/MAS NMR spectra of oxidized *np*-Si and their difference spectrum. A CP contact time of 14 ms and a MAS speed of 7.0 kHz were used.

Figure 5.14 shows the experimental and simulated ^{29}Si CP/MAS proton-decoupled NMR spectra of oxidized-and- $^1\text{H}_2\text{O}$ -treated *np*-Si, obtained using a long CP contact time (14 ms). The simulated spectrum of Figure 5.14 consists of three heavily overlapping signals whose spectral characteristics are summarized in Table 5.1. Signals

at -89, -99 and -109 ppm have Lorentzian line shapes. The use of a mixed line shape for any of the signals did not improve the match between the experimental and simulated spectra.

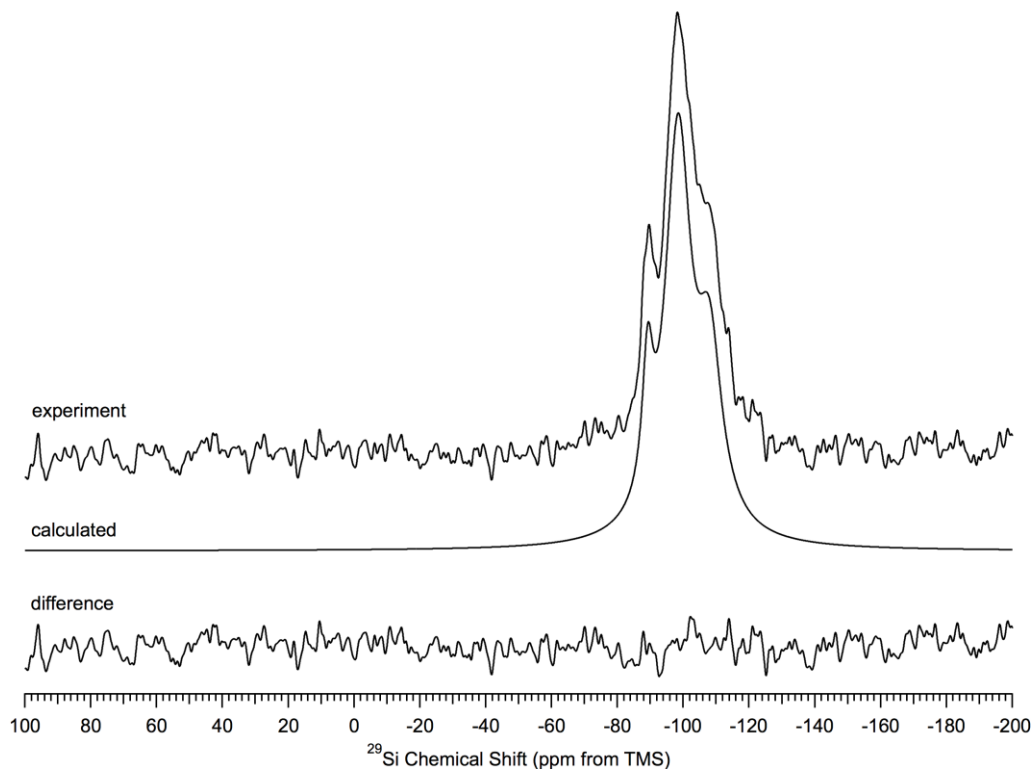


Figure 5.14. Experimental and simulated proton-decoupled ^{29}Si (71.5 MHz) CP/MAS NMR spectra of oxidized and $^1\text{H}_2\text{O}$ -treated *np*-Si and their difference spectrum. A CP contact time of 14 ms and a MAS speed of 7.0 kHz were used.

Figure 5.15 shows the experimental and simulated proton-decoupled ^{29}Si CP/MAS NMR spectra of *np*-Si that has been treated with $^1\text{H}_2\text{O}$, obtained using a long CP contact time (14 ms). The calculated spectrum of Figure 5.15 consists of six heavily

overlapping signals whose spectral characteristics are summarized in Table 5.1. The signal at -14 ppm exhibits a Gaussian line shape. Signals at -74, -83, -89, -99 and -109 ppm have Lorentzian line shapes. The use of a mixed line shape for any of the signals did not improve the match between the experimental and simulated spectra.

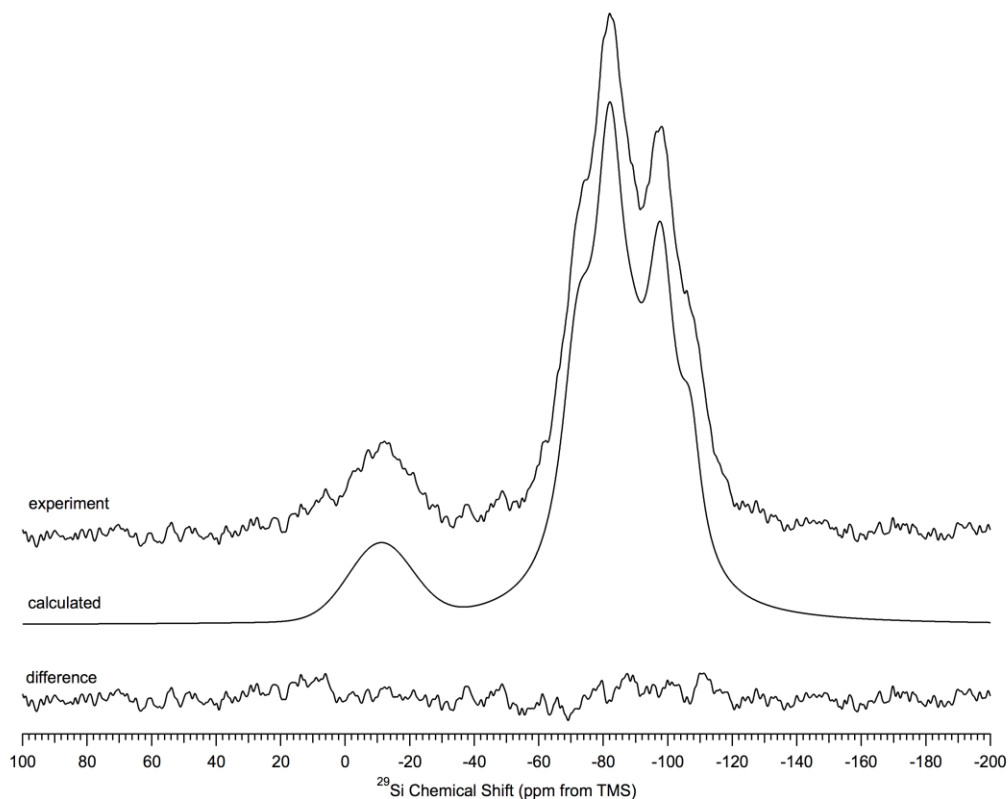


Figure 5.15. Experimental and simulated ^{29}Si (71.5 MHz) CP/MAS proton decoupled NMR spectra of $^1\text{H}_2\text{O}$ -treated *np*-Si and their difference spectrum. A CP contact time of 14 ms and a MAS speed of 7.0 kHz were used.

Carbon Analysis by ^{13}C CP/MAS Spin Counting

Figure 5.16 shows the ^{13}C CP/MAS spectra of 1% hexamethylbenzene (HMB) in silica gel and the ^{13}C CP/MAS spectra of as-received *np*-Si to determine the carbon content in the *np*-Si. Based on the integrations, it was determined that the *np*-Si contains < 1.0% carbon.

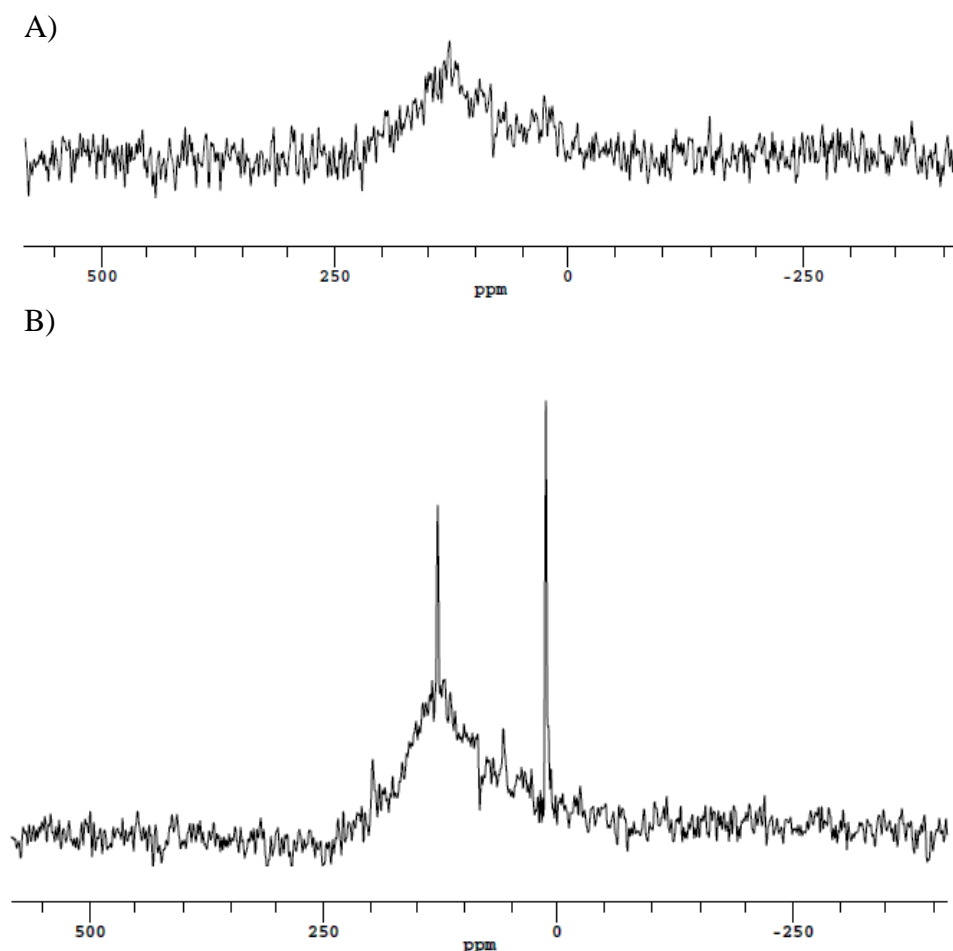


Figure 5.16. A) ^{13}C (50 MHz) CP/MAS spectrum of as-received *np*-Si. B) ^{13}C (50 MHz) CP/MAS spectrum of 1% HMB in silica gel for comparison. A CP contact time of 1 ms and a MAS speed of 3.5 kHz were used in both with 15,000 acquisitions and are displayed at the same vertical intensity with background subtraction. Based on the integration of the as-received *np*-Si and 1% HMB samples, it was determined that the as-received *np*-Si contains less than 1.0% carbon content.

CHAPTER 6

The Search for Better NMR Characterization Techniques

As is evident in the literature, one of the primary research focuses on semiconductor nanoparticles, such as silicon, is on the photoluminescent properties they possess.⁶³ Because the photoluminescence is due to quantum confinement effects, synthetic control of size is important.⁶³ Given that it is the photoluminescent properties, thus size, that is of interest to most nanoparticles silicon researchers, the majority of the literature on solution synthesis reactions for silicon nanoparticles focuses on the size aspect of the synthesis, studied via UV-VIS and TEM, with little support and proof presented for the production of chemically well characterized material. There is also limited information regarding side reactions that may possibly occur throughout the synthesis. Size control and photoluminescence are not our primary concerns; first and foremost, chemical identity (and purity) of the sample is. We hope to develop NMR techniques that would make it possible to fill in some of the large information gaps regarding what occurs throughout the synthesis, as well as perform a more detailed characterization of the product at each step.

Something that became very evident upon studying each of the systems represented above was the lack of reliable information in the literature regarding assignment of ²⁹Si NMR chemical shifts relevant to possible surface sites on crystalline

silicon. This lack of information regarding the ^{29}Si NMR chemical shifts renders difficult the assignment of peaks in the experimental spectra obtained. The specific structural moieties of interest throughout this project are primarily (Si)-H and (Si)-OH, with (Si) representing the silicon atoms of interest on the surface. Also of interest are the chemical shifts of the structures shown in Figure 2.1b and 2.1c. Although some of the literature indicates that the oxidized surfaces of the crystalline silicon samples have a structure similar to that of silica, as shown in Figure 2.1a, it is not clear, however, if the surface has other structural variations, like those shown in Figure 2.1b or 2.1c. There is a multitude of structural combinations possible, and in order for ^{29}Si ssNMR to be useful, it is highly desirable to be able to assign the chemical shifts or other spectroscopic parameters. The lack of reliable ^{29}Si chemical shift information in the literature prompted the process of building a ^{29}Si chemical shift database of our own, based on a combination of a) information from the literature, b) studying standard samples, c) information obtained from the development of new spectroscopic techniques and d) quantum-chemical calculations. One spectroscopic technique that can be useful for assigning ^{29}Si chemical shifts, which became a significant part of this thesis project, is heteronuclear $^1\text{H}\rightarrow^{29}\text{Si}$ correlation spectroscopy. A technique of this type has never been reported previously for *np*-Si.

A. $^1\text{H}\rightarrow^{29}\text{Si}$ Heteronuclear Correlation Spectroscopy

Heteronuclear correlation (HetCor) is a type of two-dimensional NMR spectroscopy used to show the internuclear connectivity or proximity within a compound. HetCor in solution is based on heteronuclear J-coupling, whereas in SSNMR it is typically based on heteronuclear dipolar coupling. By exploiting the dipolar couplings,

information on internuclear distances can be determined. Whereas HetCor has been predominately used to show correlations between ^1H and ^{13}C ,⁶⁴⁻⁶⁶ we are specifically interested in developing a HetCor technique to demonstrate correlations between ^1H and ^{29}Si .

A 2-dimensional timing sequence is generally divided into four main periods. These periods are generally denoted as the preparation period, evolution period, mixing period and the detection period. Each of these periods can be implemented in different ways to probe the different interactions that may be explored or exploited in the experiment. In $^1\text{H} \rightarrow ^{29}\text{Si}$ HetCor the preparation period is typically a $\pi/2$ ^1H pulse, which generates transverse ^1H magnetization. During the evolution period, t_1 , the protons evolve under their chemical shifts. After the ^1H have evolved under their chemical shifts, the encoded ^1H chemical shift information is transferred to the ^{29}Si spin set during a mixing period (some type of cross polarization in the case of solid state HetCor). The mixing times can be varied to discriminate different heteronuclear dipolar coupling strengths. The stronger the ^1H - ^{29}Si dipolar interaction is, the faster the $^1\text{H} \rightarrow ^{29}\text{Si}$ cross polarization will occur. The ^{29}Si chemical shift information is then collected during the detection period, represented by the time variable t_2 . A general HetCor pulse sequence is shown in Figure 6.1.

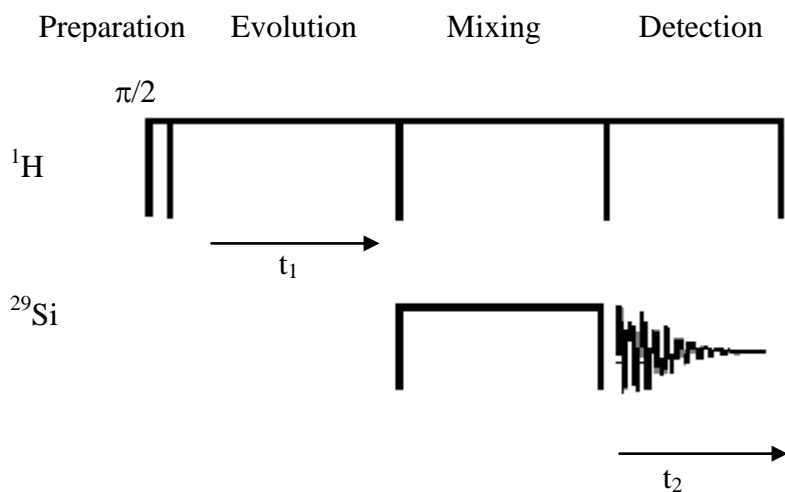


Figure 6.1. Generic $^1\text{H} \rightarrow ^{29}\text{Si}$ HetCor pulse sequence.

During the evolution period a homonuclear ^1H decoupling technique is frequently used to reduce the effects of homonuclear ^1H - ^1H dipolar coupling. This can be accomplished through multiple-pulse techniques such as MREV8, BLEW24, BR-24 or a Lee-Goldburg technique.⁶⁵⁻⁶⁷ It may also be necessary to remove the homonuclear dipolar coupling of ^{29}Si , and homonuclear ^{29}Si decoupling can be applied through a multiple-pulse sequence such as that referred to as BB24.^{65,67} The multiple-pulse techniques work in a manner in which the spin Hamiltonian is effectively manipulated to greatly reduce the effective (average) homonuclear dipolar interaction.^{65,67}

Homonuclear dipolar decoupling techniques referred to as ‘off-resonance techniques’, such as the Lee-Goldburg (LG) techniques, can also be used to remove the homonuclear dipolar coupling.⁶⁸ LG is a technique in which an offset r.f. irradiation is applied to the proton channel such that the effective ^1H field lies at 54.74° , the magic angle, relative to the z axis. It is well established that applying such an offset irradiation

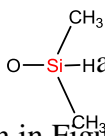
at the magic angle strongly attenuates the homonuclear dipolar coupling.⁶⁸ During evolution, this is accomplished in a manner in which the ^1H magnetization and ^1H effective field are orthogonal to each other, so spin precession and nutation occur about the effective field, which is at the magic angle.

During the mixing period it is often necessary to suppress ^1H - ^1H dipolar interactions in order to ensure that $^1\text{H}\rightarrow^{29}\text{Si}$ cross polarization is properly representative of the individual proton spin sets. This can also be accomplished through multiple-pulse techniques, as well as off-resonance techniques. The multiple-pulse technique, WIM-24, has been shown to effectively transfer polarization while suppressing ^1H - ^1H spin diffusion.^{65,66,69} WIM-24 imposes limitations on spinning speed and has a very extensive set up, making it less popular than other techniques.^{66,69} Because of this, the off-resonance Lee-Goldburg techniques have become much more popular in solid-state HetCor experiments, typically based on ^1H and ^{13}C . In using the Lee-Goldburg technique, during the mixing period, the r.f. offset is applied such that the ^1H magnetization and ^1H effective field are collinear and spin locking occurs, causing a transfer of polarization, instead of precession, relative to the effective r.f. field axis. In both multiple-pulse and Lee-Goldburg techniques the homonuclear dipolar coupling is strongly attenuated, facilitating selectivity in the polarization transfer.⁶⁹

The Lee-Goldburg technique is much more 'robust' than the multiple-pulse techniques, with significantly less set up and optimization required, so it has become the most popular technique in solid state HetCor experiments. The necessity of synchronizing multiple-pulse sequences with MAS spinning complicates the set-up of multiple-pulse techniques. LG techniques have their limitations, such as the requirement of specialized

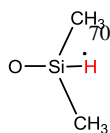
instrumentation for producing a frequency offset. What is not clear from the literature is if Lee-Goldburg is truly a superior technique or if it has just surpassed the multiple-pulse techniques in popularity due to its relative ease of implementation. As part of my thesis project, I hope to provide, for the first time, a direct and careful comparison of the two techniques, both implemented for $^1\text{H} \rightarrow ^{29}\text{Si}$ HetCor, to determine which technique serves our purposes best.

The specific application of $^1\text{H} \rightarrow ^{29}\text{Si}$ HetCor in which I am most interested is the identification of directly bonded silicon-proton pairs. The compound I have chosen for developing $^1\text{H} \rightarrow ^{29}\text{Si}$ HetCor is octakis(dimethylsiloxy)-T8-silsesquioxane, Q8M8_H, shown in Figure 6.2. The ^{29}Si CP/MAS spectrum of Q8M8_H is shown in Figure 6.3. The

peak at -0.1 ppm is assigned to  and the peak at -107 ppm is assigned to .

The ^1H MAS spectrum is shown in Figure 6.4. Faster spinning speeds were also used (up to 15 kHz), with comparable results. The peak at 0.2 ppm is assigned to  and the

peak centered at 4.8 ppm is assigned to



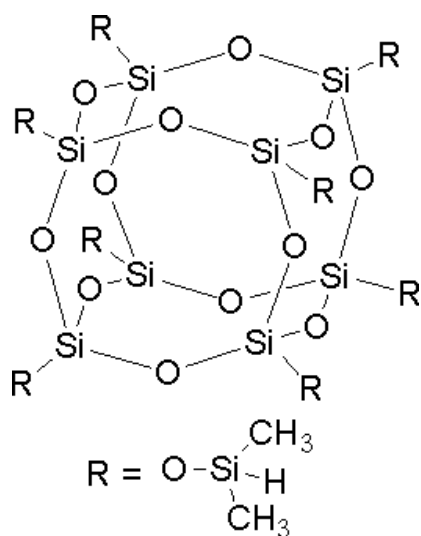


Figure 6.2. The structure of octakis(dimethylsiloxy)-T8-silsesquioxane, Q8M8_H.

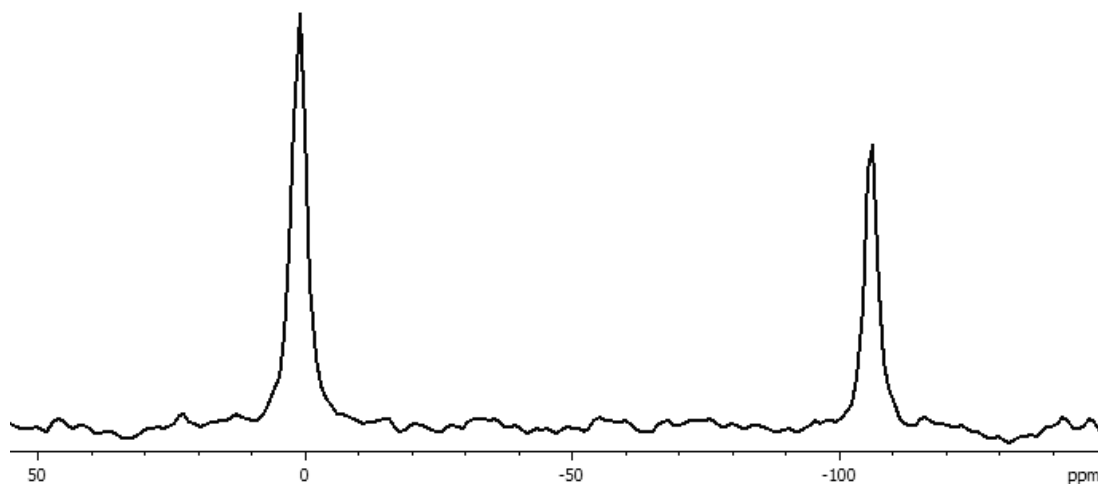


Figure 6.3. ²⁹Si CP/MAS spectrum of Q8M8_H taken at 8.5 T with 16 acquisitions, a recovery time of 20 seconds, a CP contact time of 10.0 ms, and a spinning speed of 5.33 kHz.

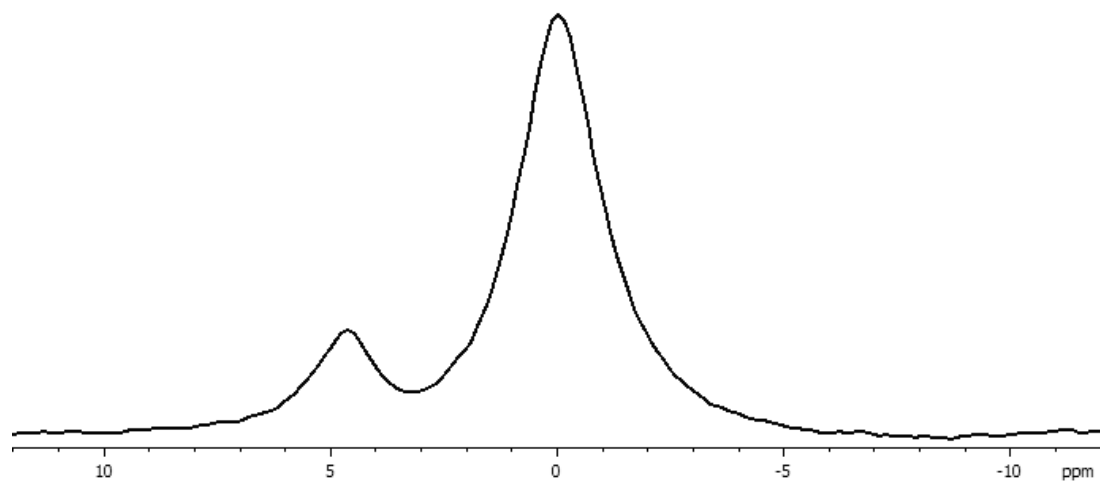


Figure 6.4. ^1H MAS spectrum of Q8M8_H taken at 8.5 T with 4 acquisitions, a recovery time of 20 s, and a spinning speed of 5.33 kHz.

$^1\text{H}\rightarrow^{29}\text{Si}$ HetCor experiments were performed on Q8M8_H to demonstrate the ability of the technique to show ^1H - ^{29}Si correlations and to determine the relevant mixing times necessary to best see these correlations. For the standard compound, Q8M8_H, both the ^1H and ^{29}Si chemical shifts are known in the literature and are in agreement with the values given above.⁷⁰ Known chemical shift identifications for both ^{29}Si and ^1H makes Q8M8_H an optimal candidate as a test standard to develop $^1\text{H}\rightarrow^{29}\text{Si}$ HetCor; it is one of few commercially available solids containing silicon with directly bonded hydrogen. The relevant pulse sequences used throughout the study are shown below, in Figure 6.5.

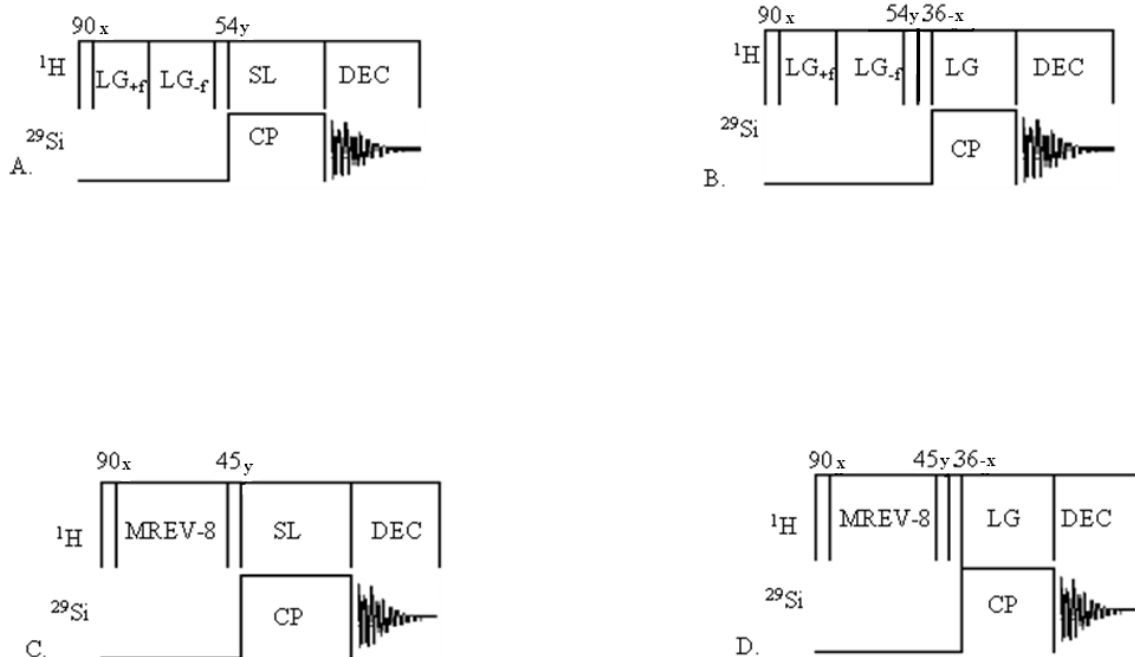
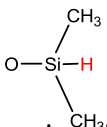
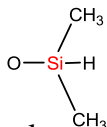
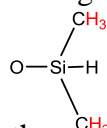
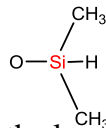


Figure 6.5. $^1\text{H} \rightarrow ^{29}\text{Si}$ HetCor pulse sequences under various conditions. **A.** Lee-Goldburg during the evolution period and Hartmann-Hahn cross polarization during the mixing period. **B.** Lee-Goldburg during the evolution period and Lee-Goldburg cross polarization during the mixing period. **C.** MREV-8 during the evolution period and Hartmann-Hahn cross polarization during the mixing period. **D.** MREV-8 during the evolution period and Lee-Goldburg cross polarization during the mixing period.

B. Comparison of $^1\text{H} \rightarrow ^{29}\text{Si}$ Hetcor Techniques via direct (X) detection

The first set of $^1\text{H} \rightarrow ^{29}\text{Si}$ HetCor spectra obtained on Q8M8_H are shown in Figure 6.6 with the same information displayed in a different format in Figure 6.7. These spectra were obtained under Lee-Goldburg conditions during the evolution period and Hartmann-Hahn cross polarization during the mixing period. The pulse sequence used to acquire these data is shown in Figure 6.5A. A series of mixing times were examined (0.2 ms, 1.0 ms, 2.0 ms, and 5.0 ms) and the resulting contour plots are shown in Figure 6.6. Figure 6.6 also shows the corresponding projection views of both the indirect and direct

dimensions. The direct dimension is along the horizontal axis and is the ^{29}Si chemical shift dimension. The indirect dimension is along the vertical axis and is the ^1H chemical shift dimension. At what is considered to be a short mixing time, 0.2 ms, a strong correlation is seen between  at 4.8 ppm, and  at -0.1 ppm. This is shown in Figure 6.6. As the mixing time is increased to the largest value of 5.0 ms shown in Figure 6.6, a stronger correlation is seen between  at 0.2 ppm and  at -0.1 ppm. Shorter mixing times discriminate against the methyl protons due to the longer internuclear Si-H distances (and rapidly rotating methyl group) and therefore weaker dipolar coupling.

Contour plots, like those shown in Figure 6.6, are what are typically shown in the literature. The problem is that they are often not as telling about the data as are corresponding stacked plots (*vide infra*). The ‘floor level’ (threshold) of a contour plot is chosen such that all that is shown in the contour plot is any intensity above the floor, allowing for the possibility of many undesirable features to be hidden. While contour plots are useful in seeing strong correlations easily, when looking for weak correlations one needs to be confident of the significance of weak signals, especially when comparing different techniques. Stacked plots allow for a more fair and accurate evaluation. The same data that are shown in Figure 6.6 in a contour plot are represented in Figure 6.7 as stacked plots.

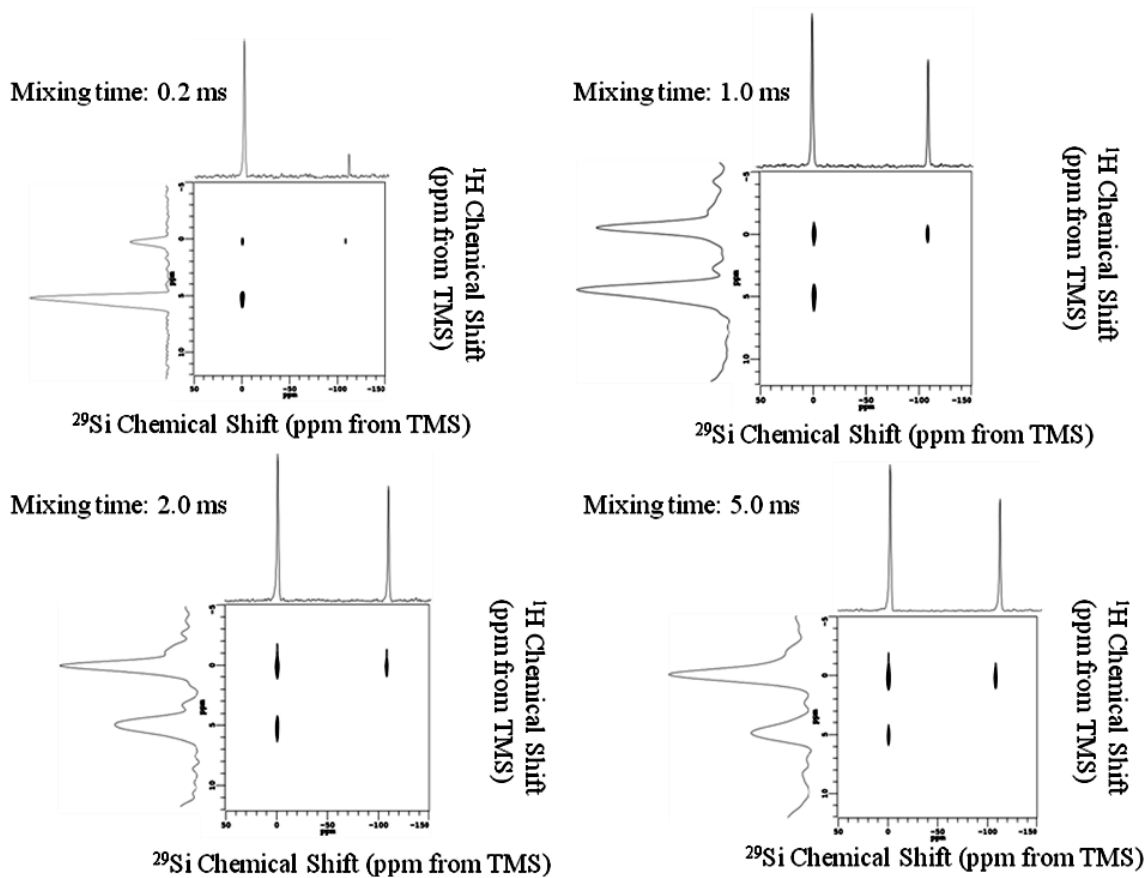


Figure 6.6. Contour plots of $^1\text{H} \rightarrow ^{29}\text{Si}$ HetCor spectra of Q8M8_H, obtained with Lee-Goldburg applied during the evolution period and Hartmann-Hahn cross polarization during the mixing period. Various mixing times were examined. The spectra were acquired at 8.5 T with 16 acquisitions and a recovery time of 30 s.

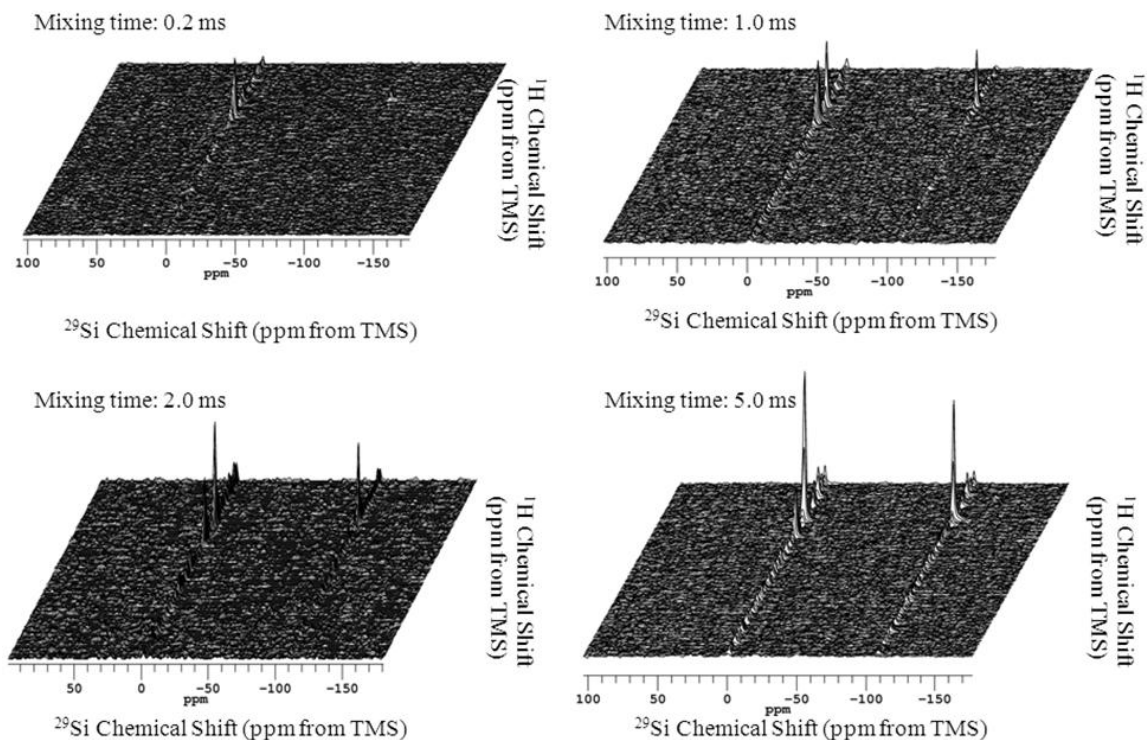


Figure 6.7. Stacked plots of $^1\text{H} \rightarrow ^{29}\text{Si}$ HetCor spectra of Q8M8_H with Lee-Goldburg applied during the evolution period and Hartmann Hahn cross polarization during the mixing period. Various mixing times were examined. The spectra were acquired at 8.5 T with 16 acquisitions and a recovery time of 30 s.

In addition to the data shown above, Q8M8_H was also studied by the HetCor pulse-sequence shown in Figure 6.5B. This pulse-sequence utilizes Lee-Goldburg during the evolution period to reduce ^1H - ^1H coupling, as well as during the mixing period (cross polarization) to ensure selectivity of polarization transfer. Contour plots of the HetCor spectra obtained on Q8M8_H by HetCor with Lee-Goldburg in both the evolution period and the mixing period are seen in Figure 6.8 with the corresponding stacked plot shown in Figure 6.9. The f_1 ridge is larger when Lee-Goldburg is used during both the evolution period and the mixing period (Figure 6.5B) than when Lee-Goldburg is used on during the evolution period and Hartmann-Hahn cross polarization

(Figure 6.5A) is employed, but still allows for identifications to be made. The changes in the f_1 ridge at short contact times, which are the mixing times of primary interest, are not as large as at larger contact times.

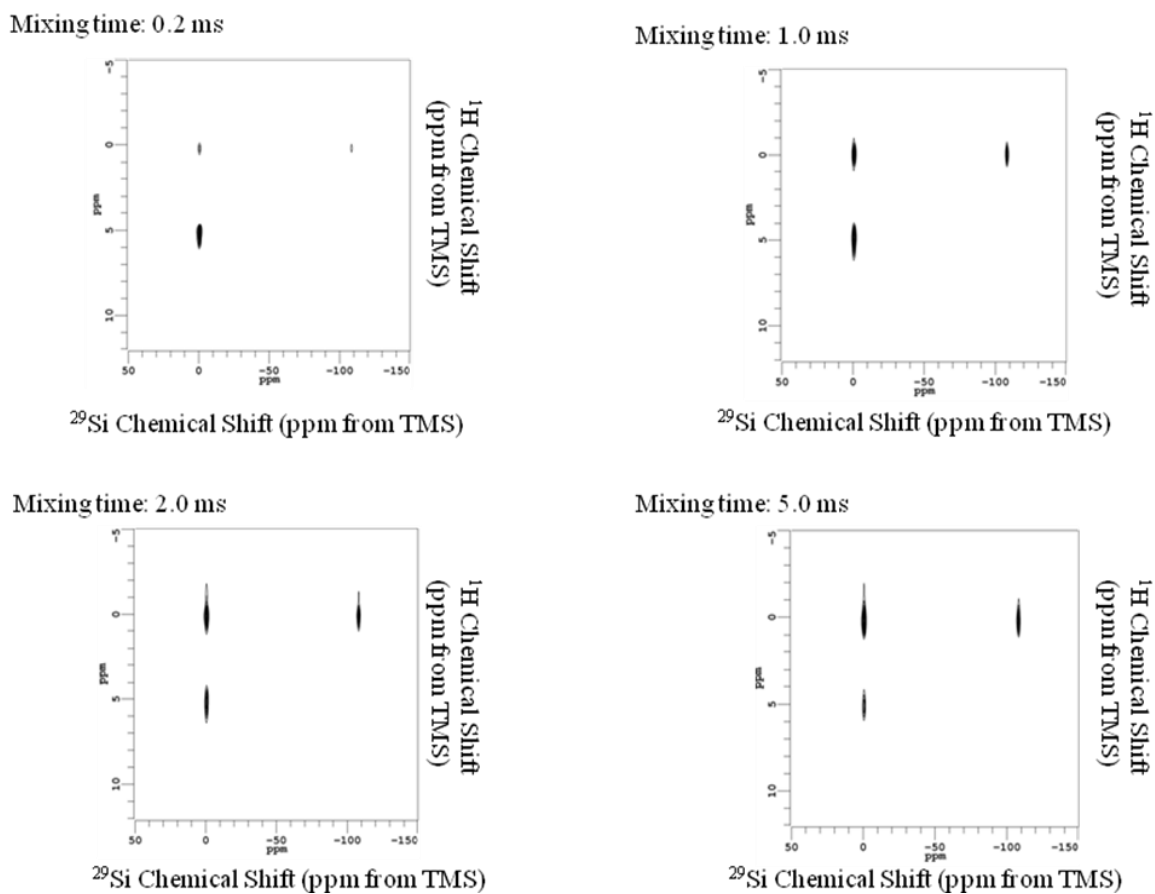


Figure 6.8. Contour plots of $^1\text{H} \rightarrow ^{29}\text{Si}$ HetCor spectra of Q8M8_H obtained with LG applied during the evolution period and LG cross polarization during the mixing period. Various mixing times were examined. The spectra were acquired at 8.5 T with 16 acquisitions and a recovery time of 30 s.

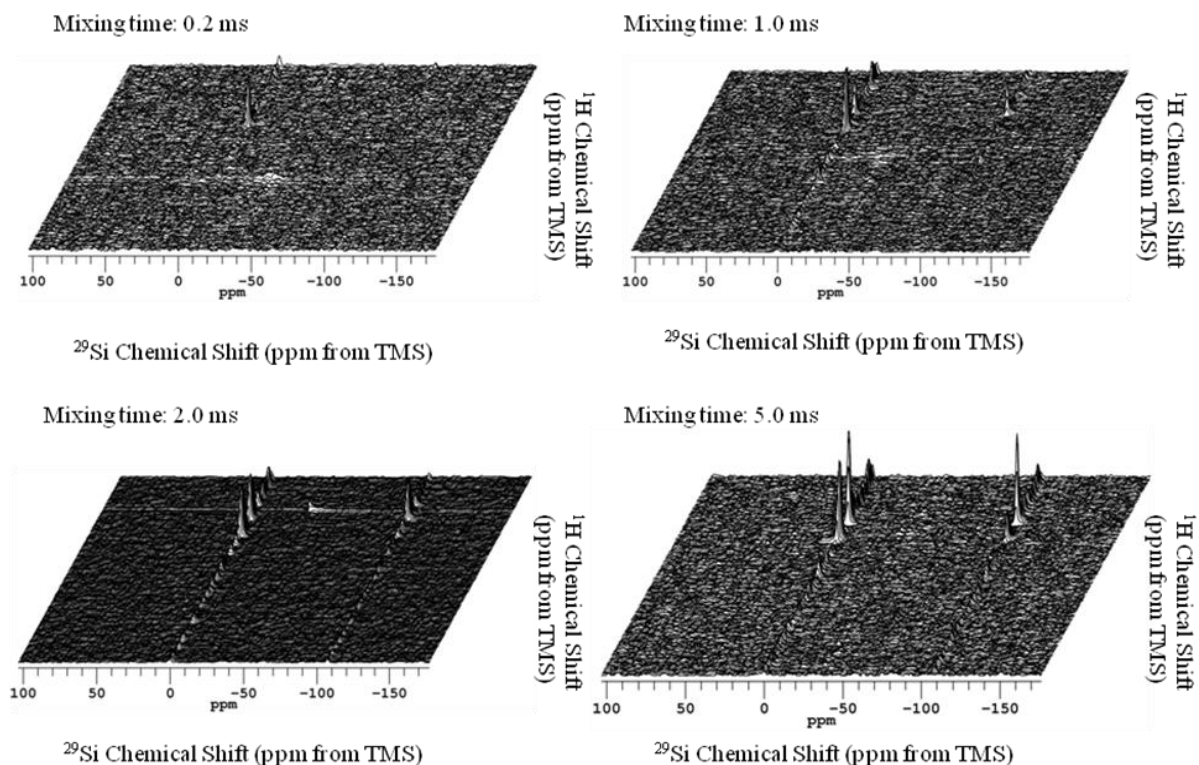
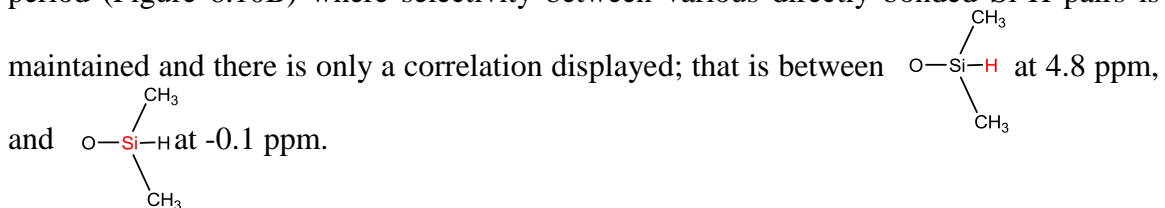


Figure 6.9. Stacked plots of $^1\text{H} \rightarrow ^{29}\text{Si}$ HetCor spectra of Q8M8_H with LG applied during the evolution period and Lee-Goldburg cross polarization during the mixing period. Various mixing times were examined. The spectra were acquired at 8.5 T with 16 acquisitions and a recovery time of 30 s.

Since Lee-Goldburg cross polarization was utilized during the mixing period to attenuate spin diffusion and enhance selectivity in the HetCor experiments that generated Figures 6.8 and 6.9, one would expect that this technique would provide spectra that are more selective for the Si-H interaction than are HetCor spectra obtained when Hartmann-Hahn cross polarization (without LG) is utilized during the mixing period, as shown in Figures 6.6 and 6.7. The advantage of Lee-Goldburg cross polarization over Hartmann-Hahn cross polarization is more easily seen by focusing in on the chemical shift region

that contains the Si-H correlations. In comparing when Lee-Goldburg was used during the evolution period with Hartmann-Hahn cross polarization during the mixing period (Figure 6.10A) and when Lee-Goldburg was used during both the evolution period and for cross polarization during the mixing period (Figure 6.10B) the selectivity of Lee-Goldburg for the Si-H interaction can be seen (pulse-sequence Figure 6.5A and Figure 6.5B respectively).

The use of Lee-Goldburg during the mixing period demonstrates that spin diffusion is suppressed. As can be seen in Figure 6.10A, when Hartmann-Hahn cross polarization (without LG) was used during the mixing period, a correlation is seen between $\text{O}-\text{Si}-\text{H}$ at 0.2 ppm and $\text{O}-\text{Si}-\text{H}$ at -0.1 ppm in addition to the correlation between $\text{O}-\text{Si}-\text{H}$ at 4.8 ppm, and $\text{O}-\text{Si}-\text{H}$ at -0.1 ppm. This is in contrast to the result obtained when Lee-Goldburg cross polarization was used during the mixing period (Figure 6.10B) where selectivity between various directly bonded Si-H pairs is maintained and there is only a correlation displayed; that is between $\text{O}-\text{Si}-\text{H}$ at 4.8 ppm, and $\text{O}-\text{Si}-\text{H}$ at -0.1 ppm.



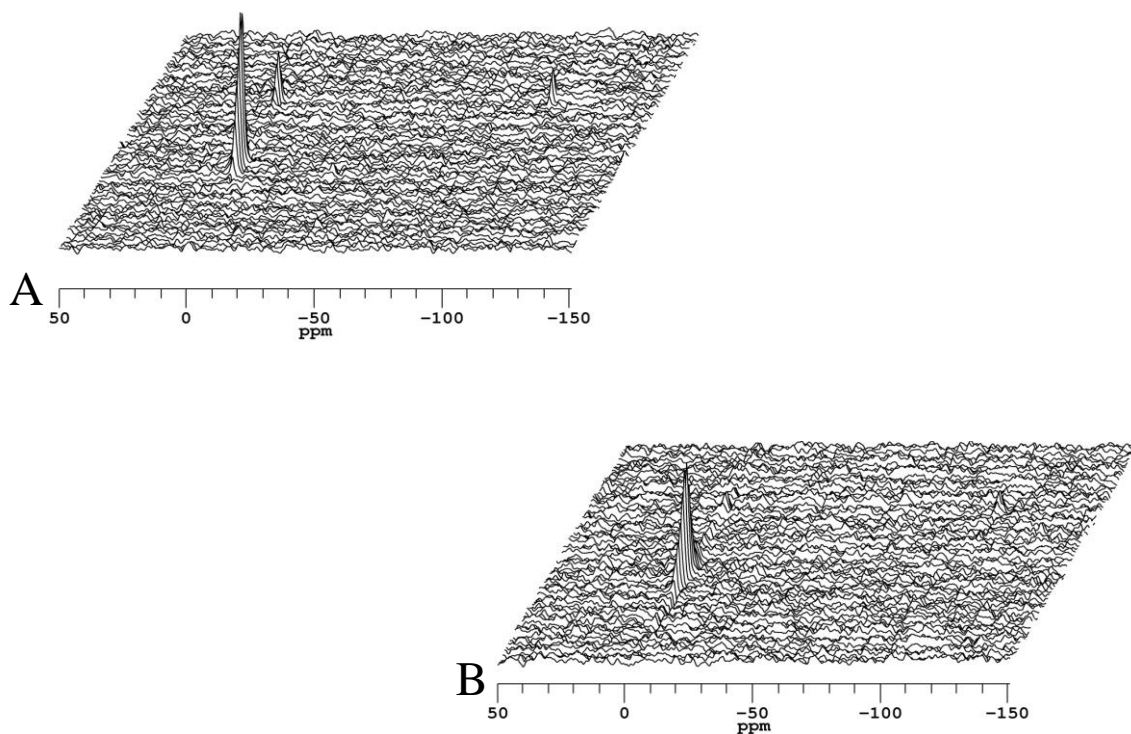
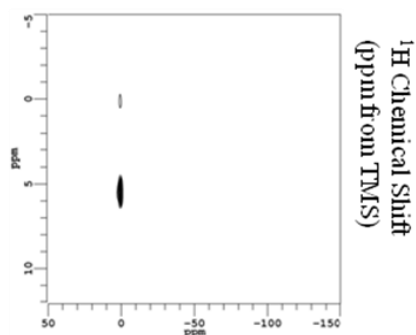


Figure 6.10. **A.** Region of interest for when Lee-Goldburg cross polarization was not used during the mixing period. **B.** Region of interest for when Lee-Goldburg cross polarization was used during the mixing period.

As previously mentioned, multiple-pulse techniques can also be used for the attenuation of ^1H - ^1H dipolar interactions. Figure 6.11 shows contour plots of a set of $^1\text{H} \rightarrow ^{29}\text{Si}$ HetCor spectra obtained with MREV-8, a multiple-pulse technique for removing ^1H - ^1H dipolar coupling,⁶⁷ applied during the evolution period and Hartmann-Hahn cross polarization (without any ^1H - ^1H suppression) used during the mixing period. The same set of data is represented in Figure 6.12 in stacked plot form. It is clear from looking at the spectra in Figure 6.12 that the f_1 ridge artifact is not as significant when MREV-8 was used during the evolution period as it is when Lee-Goldburg was used during the evolution period (Figure 6.9), allowing for a better S/N along the f_1 dimension in the former case. However, in my judgment, the advantage in S/N when MREV-8 was

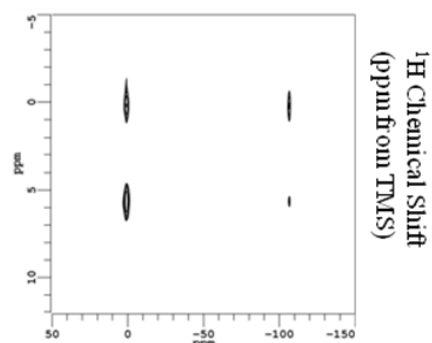
used during the evolution period is not significant enough to compensate for the extensive experimental set-up and optimization of the multiple-pulse techniques.

Mixing time: 0.2 ms



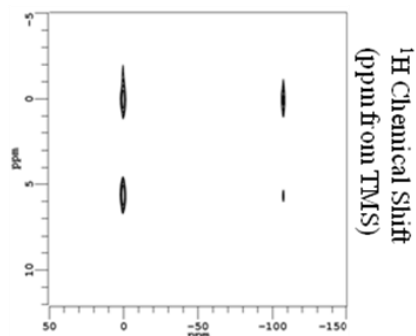
^{29}Si Chemical Shift (ppm from TMS)

Mixing time: 1.0 ms



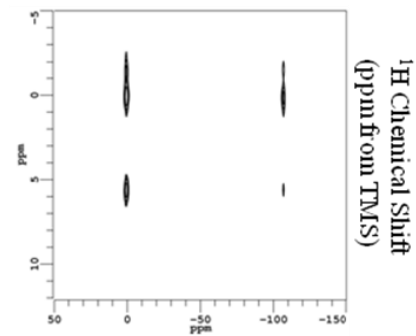
^{29}Si Chemical Shift (ppm from TMS)

Mixing time: 2.0 ms



^{29}Si Chemical Shift (ppm from TMS)

Mixing time: 5.0 ms



^{29}Si Chemical Shift (ppm from TMS)

Figure 6.11. Contour plots of $^1\text{H} \rightarrow ^{29}\text{Si}$ HetCor spectra of Q8M8_H obtained with MREV-8 applied during the evolution period and Hartmann-Hahn cross polarization during the mixing period. Various mixing times were examined. The spectra were acquired at 8.5 T with 16 acquisitions and a recovery time of 30 s.

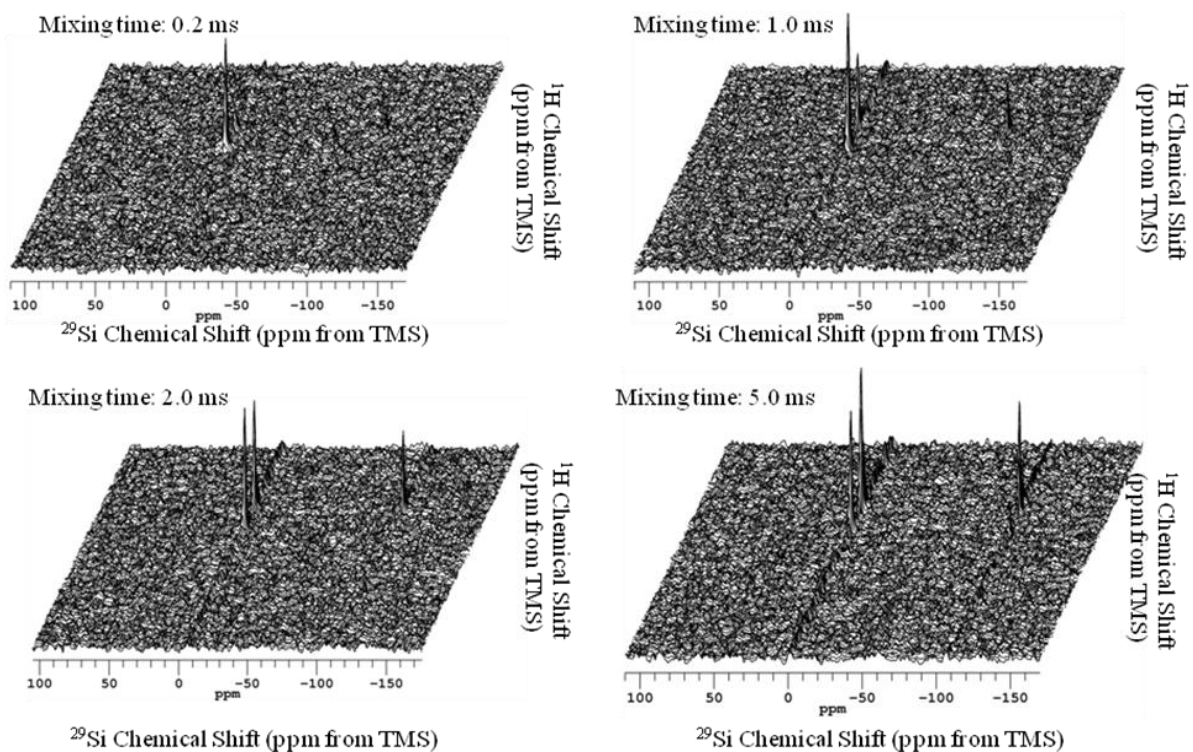


Figure 6.12. Stacked plots of $^1\text{H} \rightarrow ^{29}\text{Si}$ HetCor spectra of Q8M8_H obtained with MREV-8 applied during the evolution period and Hartmann-Hahn cross polarization during the mixing period. Various mixing times were examined. The spectra were acquired at 8.5 T with 16 acquisitions and a recovery time of 30 s.

The multiple-pulse sequence, MREV-8, was used during the evolution period in conjunction with Lee-Goldburg cross polarization during the mixing period (Figure 6.5D). It was found that when MREV-8 was used during the evolution period to attenuate ^1H - ^1H spin diffusion during evolution rather than Lee-Goldburg, the f_1 ridge was significantly less. By using MREV-8 during the evolution and Lee-Goldburg cross polarization during the mixing period, the ability of Lee-Goldburg to attenuate spin-diffusion during cross polarization can be evaluated. The contour plots of the resulting HetCor spectra are shown in Figure 6.13, with the corresponding stacked plots in Figure

6.14. As can be seen in the stacked plots obtained at the short contact time of 0.200 ms, selectivity was maintained, as evidenced by the absence of a correlation peak between 4.8 ppm (^1H) and -0.1 ppm (^{29}Si). The selectivity was also maintained at longer contact times, as can be seen by the fact that the correlation peak at 4.8 ppm (^1H), -0.1 ppm (^{29}Si) remains larger when Lee-Goldburg cross polarization was used during the mixing period (Figure 6.14) than when Lee-Goldburg cross polarization was not used during the mixing period (Figure 6.7).

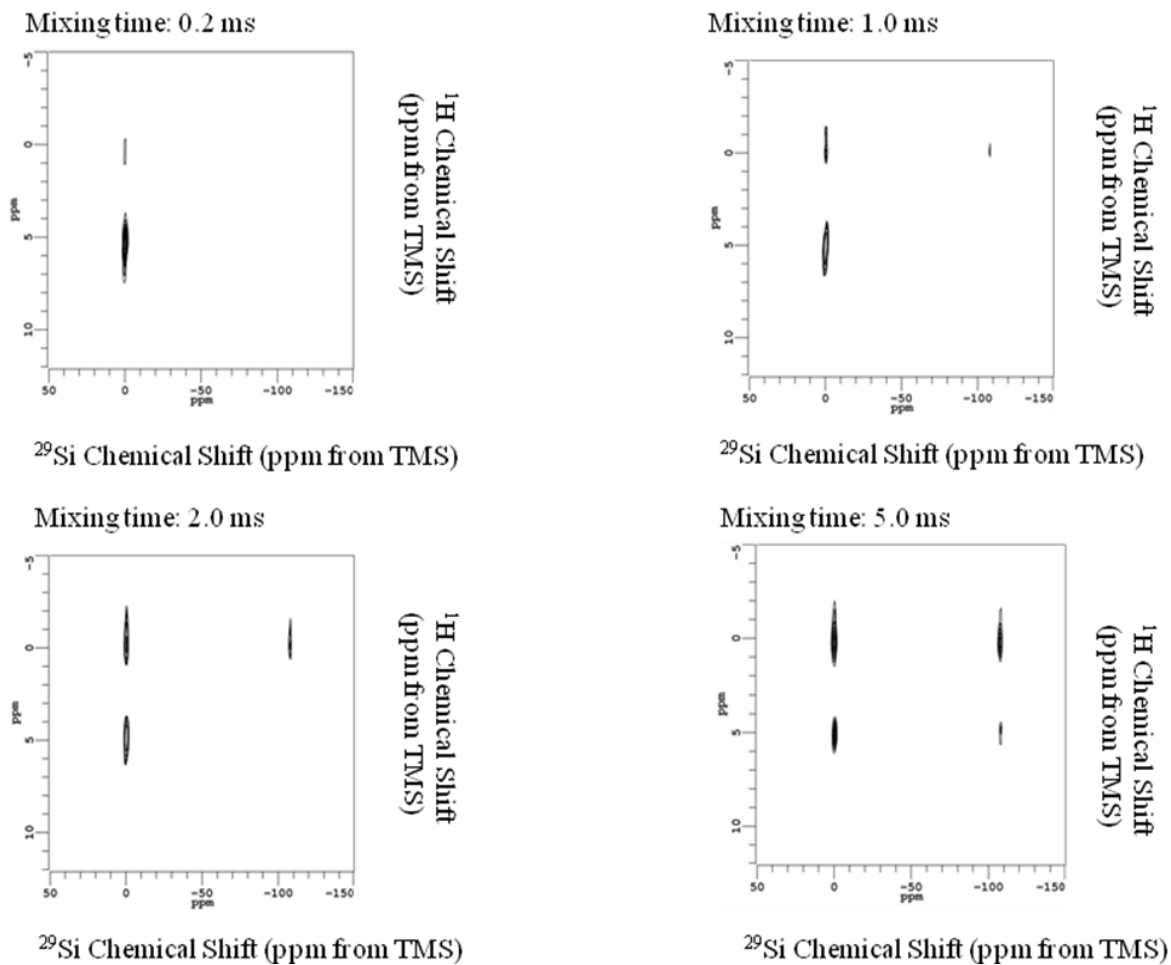


Figure 6.13. Contour plots of $^1\text{H} \rightarrow ^{29}\text{Si}$ HetCor spectra obtained with MREV-8 applied during the evolution period and Lee-Goldburg cross polarization during the mixing period. Various mixing times were examined. The spectra were acquired at 8.5 T with 16 acquisitions and a recovery time of 30 s.

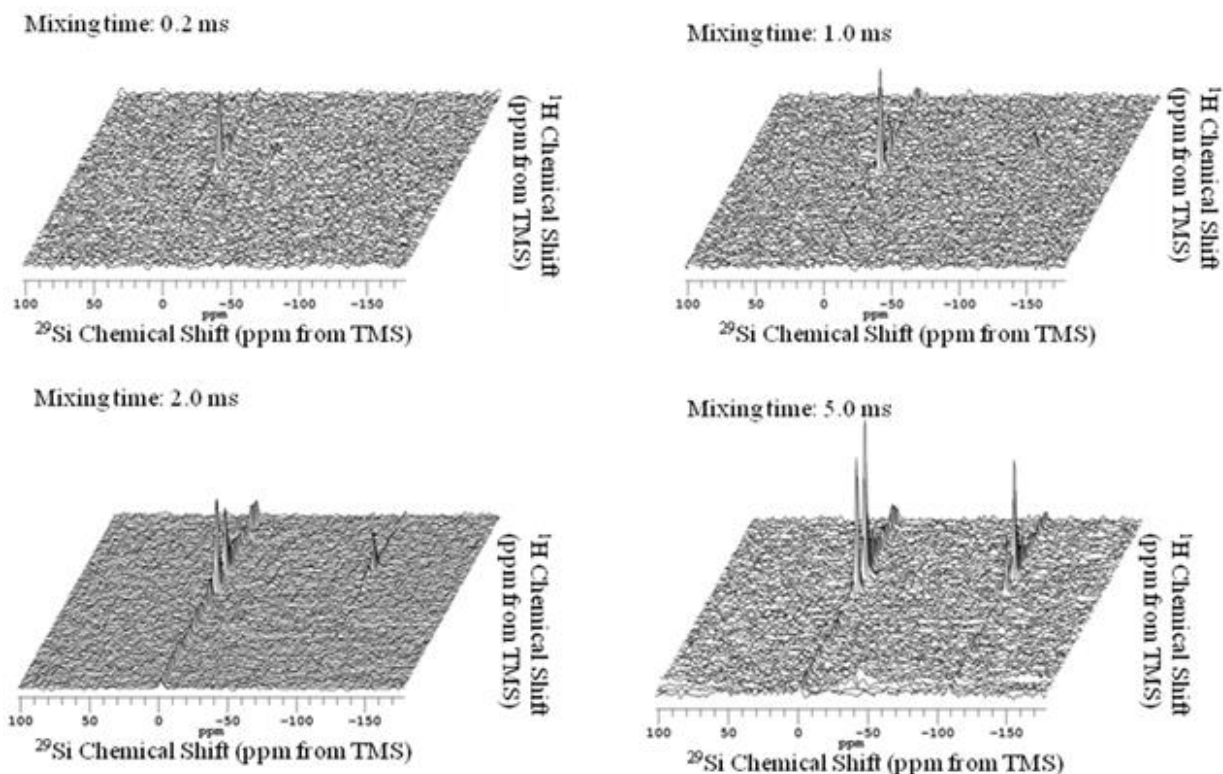


Figure 6.14. Stacked plots of $^1\text{H} \rightarrow ^{29}\text{Si}$ HetCor spectra obtained with MREV-8 applied during the evolution period and Lee-Goldburg cross polarization during the mixing period. Various mixing times were examined. The spectra were acquired at 8.5 T with 16 acquisitions and a recovery time of 30 s.

A comparison of the region of interest for short mixing periods for the four different pulse sequences of Figure 6.5 can be seen in Figure 6.15. It can be seen that use of either Lee-Goldburg or MREV-8 during the evolution period is sufficient to reduce the ^1H - ^1H dipolar coupling and provide line narrowing in the ^1H dimension. It can also be seen that, regardless of whether a multiple-pulse technique or a Lee-Goldburg technique is used during the evolution period, when Lee-Goldburg cross polarization is implemented during the mixing period, selectivity is maintained; i.e., a correlation peak is seen between 4.8 ppm (^1H) and -0.1 ppm (^{29}Si).

In addition to Lee-Goldburg cross polarization techniques for use during the mixing period, there are multiple-pulse cross polarization techniques for reducing the spin-diffusion and maintaining selectivity of polarization transfer. One such multiple-pulse technique for ensuring selectivity is WIM-24.⁶⁶ The use of WIM-24 for cross polarization was tried as a 1-D experiment and, as compared to Hartmann-Hahn polarization transfer, provided a relative efficiency of 21%. Although not documented in the literature, after discussion with the few that have used this technique, this is near optimum efficiency for WIM-24.^{66,71} This is shown in Figure 6.16. It was also determined that Hartmann-Hahn cross polarization at contact times that are short enough could still provide selectivity, but with a slightly better S/N. This is also shown in Figure 6.16. Given that the efficiency of WIM-24 is low and Hartmann-Hahn cross polarization at low contact times provides the same selectivity with better S/N, it was concluded that WIM-24 is not the optimal technique for selective cross polarization.

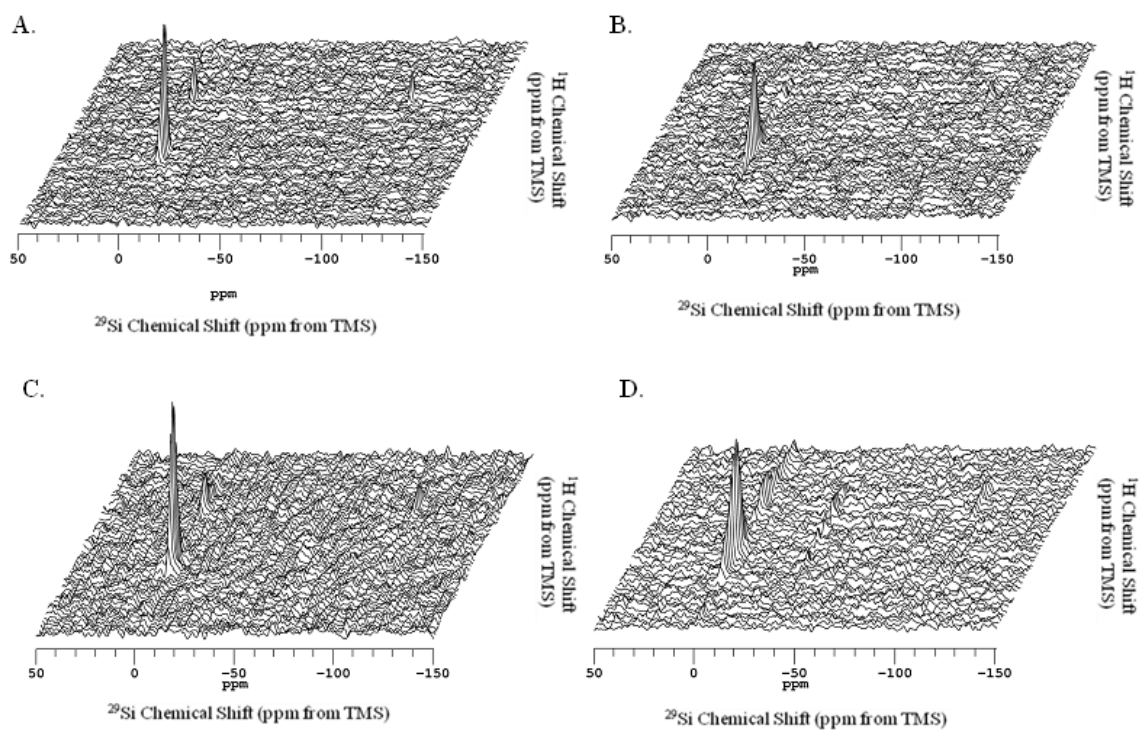


Figure 6.15. Comparison of the region of interest (0.2 ms ct) corresponding to the pulse-sequences shown in Figure 6.5. A. Based on the sequence shown in Figure 6.5A. B. Based on the sequence shown in Figure 6.5B. C. Based on the sequence shown in Figure 6.5C. D. Based on the sequence shown in Figure 6.5D.

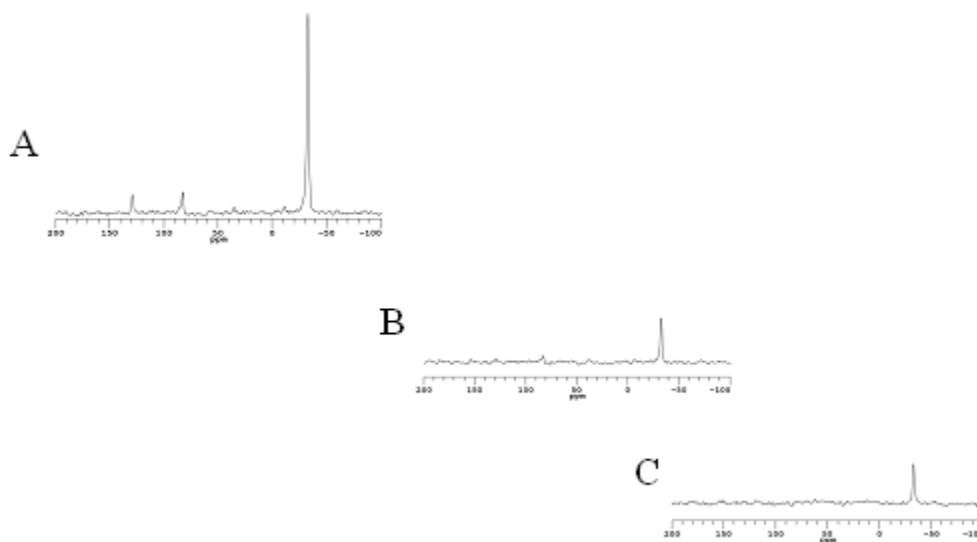


Figure 6.16. A comparison of the efficiency of WIM-24 for polarization transfer with Hartmann-Hahn polarization transfer. A. The ^{13}C CP/MAS spectrum of hexamethylbenzene taken with a contact time of 0.120 ms. B. The ^{13}C CP/MAS spectrum of hexamethylbenzene taken with a contact time of 0.35 ms using Hartmann-Hahn cross polarization. C. The ^{13}C CP/MAS spectrum of hexamethylbenzene taken with one WIM-24 cycle, a contact time of 0.120 ms.

In comparing the different pulse sequences represented in Figure 6.15 (and shown in Figure 6.5), it was decided that the pulse sequence/techniques that best suits our interest is Lee-Goldburg during the evolution with either Hartmann-Hahn cross-polarization (Figure 6.5A) or Lee-Goldburg cross polarization (Figure 6.5B). This is because of the fact that Lee-Goldburg is much easier to implement and yields results comparable to that of the multiple-pulse technique, MREV-8. Should it be necessary to use a cross polarization technique during the mixing period that suppresses spin-diffusion, Lee-Goldburg during the evolution period and Lee-Goldburg cross polarization during the mixing period (Figure 6.5B) can be used.

In order to provide additional information on the performance of $^1\text{H} \rightarrow ^{29}\text{Si}$ HetCor, a test sample that is a combination of Q8M8_H with t-butyl trichlorosilane,

$(\text{CH}_3)_3\text{CSiCl}_3$, was examined. T-butyl trichlorosilane was chosen because both the ^1H and ^{29}Si chemical shifts are different than the corresponding chemical shifts of Q8M8_H, with a ^1H MAS chemical shift of 1 ppm and a ^{29}Si CP/MAS chemical shift of 16 ppm. t-butyl trichlorosilane also differs from Q8M8_H in that the closest ^{29}Si - ^1H pair is three bonds apart. This is in contrast to Q8M8_H where silicon has directly bonded protons as well as ^{29}Si , ^1H pairs that are two bonds away. A mixture of t-butyl trichlorosilane and Q8M8_H provides a good test of the HetCor pulse-sequence consisting of Lee-Goldburg during the evolution and Hartmann-Hahn cross polarization (Figure 6.5A) because it allows for a comparison of silicon that has directly bonded protons as well as ^{29}Si , ^1H pairs that are two and three bonds apart. A series of mixing times were studied, ranging from 0.2 ms to 7 ms, and the contour plots of the results are shown in Figure 6.17. Stacked plots corresponding to the same set of data are shown in Figure 6.18. For a short contact time of 0.200 ms, it can be seen in Figure 6.17 and 6.18 that there is a strong correlation between directly-bonded ^{29}Si , ^1H pairs. As the contact time is increased to 2.0 ms, one sees strong correlations between ^{29}Si , ^1H pairs that are two bonds apart and weak correlations beginning to show at (1.0 ppm (^1H), 16.0 ppm (^{29}Si)) from ^{29}Si , ^1H pairs that are three bonds apart. By the time the contact time is increased to 7.0 ms, even correlations between ^{29}Si , ^1H pairs that are three bonds apart are strong.

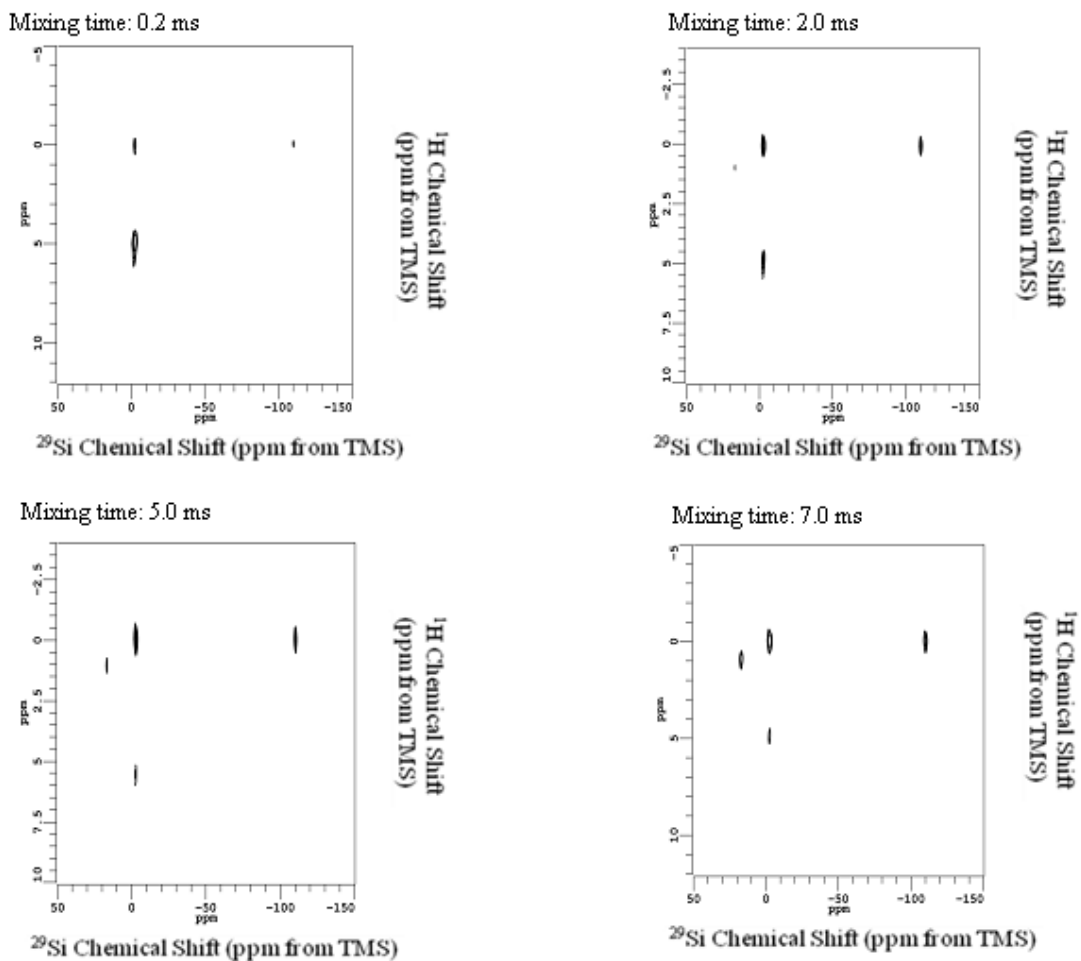


Figure 6.17. Contour plots of $^1\text{H} \rightarrow ^{29}\text{Si}$ HetCor spectra a Q8M8_H/t-butyl trichlorosilane mixture, obtained with Lee-Goldburg applied during the evolution period and Hartman-Hahn cross polarization during the mixing period. Various mixing times were examined. The spectra were acquired at 8.5 T with 16 acquisitions and a recovery time of 30 s.

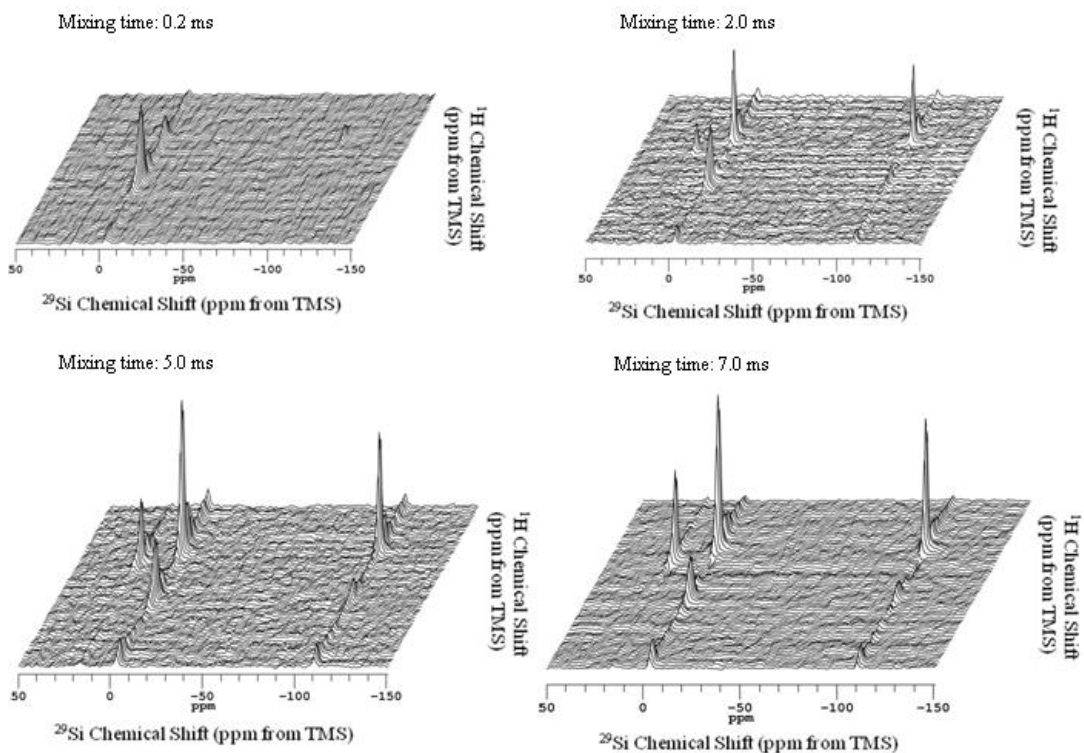


Figure 6.18. Stacked plots of $^1\text{H} \rightarrow ^{29}\text{Si}$ HetCor spectra a Q8M8_H/t-butyl trichlorosilane mixture, obtained with Lee-Goldburg applied during the evolution period and Hartman-Hahn cross polarization during the mixing period. Various mixing times were examined. The spectra were acquired at 8.5 T with 16 acquisitions and a recovery time of 30 s.

A HetCor sequence consisting of Lee-Goldburg during the evolution period and Lee-Goldburg during the mixing period (Figure 6.5B) was also applied to the t-butyl trichlorosilane/ Q8M8_H mixture. The contour plot is shown in Figure 6.19, with the corresponding stacked plot in Figure 6.20. The use of Lee-Goldburg cross polarization demonstrates that at short contact times of 0.2 ms spin-diffusion is suppressed and only the directly bonded ^{29}Si - ^1H pairs are seen. It can also be seen that selectivity for directly bonded protons was maintained by the stronger correlation between silicon and the directly bonded protons at (4.8 ppm (^1H), -0.1 ppm (^{29}Si)) as the contact time increased,

when Lee-Goldburg cross polarization was used during the mixing period (Figure 6.19), as compared to Hartmann-Hahn cross polarization during the mixing period (Figure 6.17).

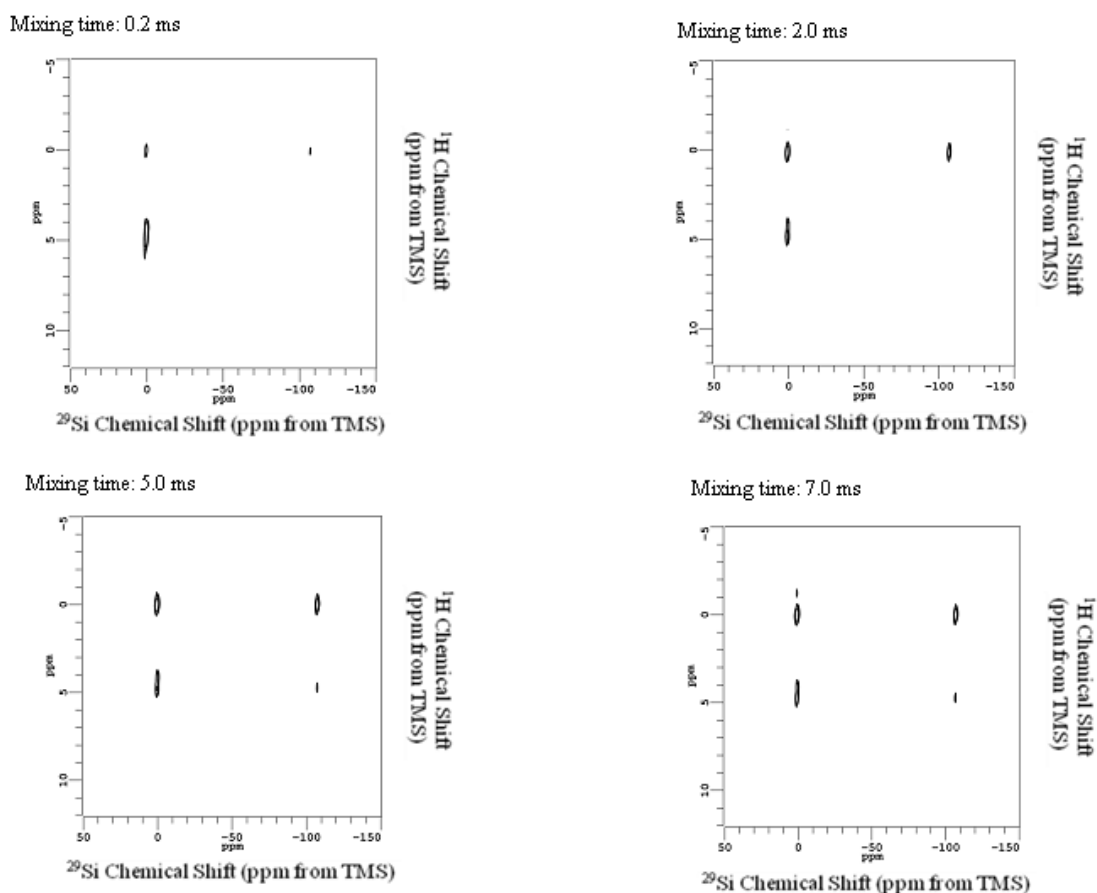


Figure 6.19. Contour plots of $^1\text{H} \rightarrow ^{29}\text{Si}$ HetCor spectra a Q8M8_H/t-butyl trichlorosilane mixture, obtained with Lee-Goldburg applied during the evolution period and Lee-Goldburg cross polarization during the mixing period. Various mixing times were examined. The spectra were acquired at 8.5 T with 16 acquisitions and a recovery time of 30 s.

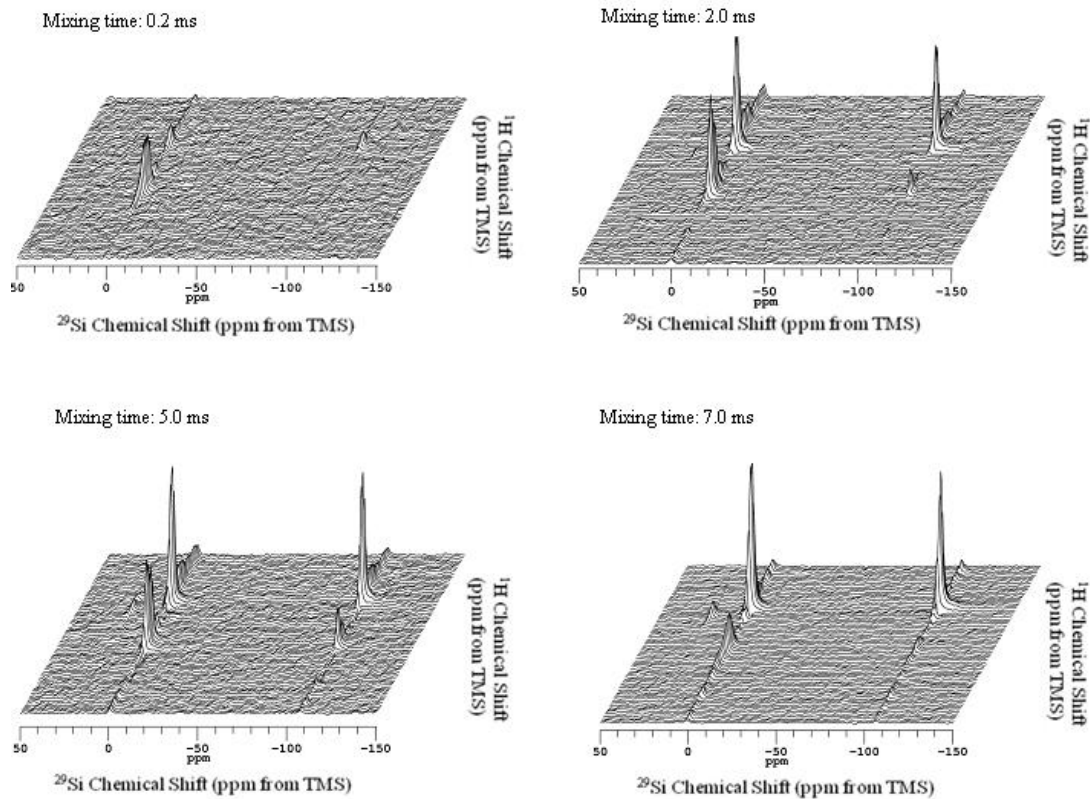


Figure 6.20. Stacked plots of $^1\text{H} \rightarrow ^{29}\text{Si}$ HetCor spectra a Q8M8_H/t-butyl trichlorosilane mixture, obtained with Lee-Goldburg applied during the evolution period and Lee-Goldburg cross polarization during the mixing period. Various mixing times were examined. The spectra were acquired at 8.5 T with 16 acquisitions and a recovery time of 30 s.

C. Indirect Detection $\{^{29}\text{Si} \rightarrow ^1\text{H}\}$ HetCor

A continuing difficulty we face is low S/N during $^1\text{H} \rightarrow ^{29}\text{Si}$ HetCor experiments due to the low surface areas of the commercially available forms of crystalline silicon. The commercially available form of crystalline silicon with the largest surface area, silicon nanopowder, has a surface area that is still low ($\sim 86.5 \text{ m}^2/\text{g}$) compared to what is desired (e.g., hundreds of m^2/g). The S/N difficulties of silicon nanopowder, as shown in Figures 5.2 and 5.3, have been discussed above. There are detection techniques that can serve to enhance the sensitivity. One such method I hope to develop is *indirect detection* for ^{29}Si .⁷²⁻⁷⁵ With indirect detection, ^1H is detected, rather than ^{29}Si . There is an inherent sensitivity gain, because of the difference in gyromagnetic ratios of these two nuclides (and the corresponding effects on the Boltzmann factor and transition probabilities).⁷²⁻⁷⁵ Figure 6.21 shows a generic pulse sequence for an indirect detection technique.

In indirectly detected HetCor sequence, as documented in the literature,⁷⁴ proton magnetization is first transferred by $^1\text{H} \rightarrow ^{29}\text{Si}$ cross polarization to generate ^{29}Si magnetization. During the t_1 period the ^{29}Si spins evolve under their chemical shifts. The ^{29}Si chemical shift information is then stored, with necessary storage steps, while any residual ^1H magnetization is then allowed to dephase. This step, however, causes a loss of $\frac{1}{2}$ the magnetization, as only one component is stored. The ^{29}Si magnetization can then be efficiently transferred through cross polarization back to ^1H for detection. ^1H detected $^1\text{H} \rightarrow ^{29}\text{Si}$ HetCor can utilize Lee-Goldburg cross polarization during the second mixing period to ensure selectivity during cross polarization as well as have a multiple pulse technique incorporated into the t_2 dimension to reduce the effects of spin diffusion in the ^1H dimension.

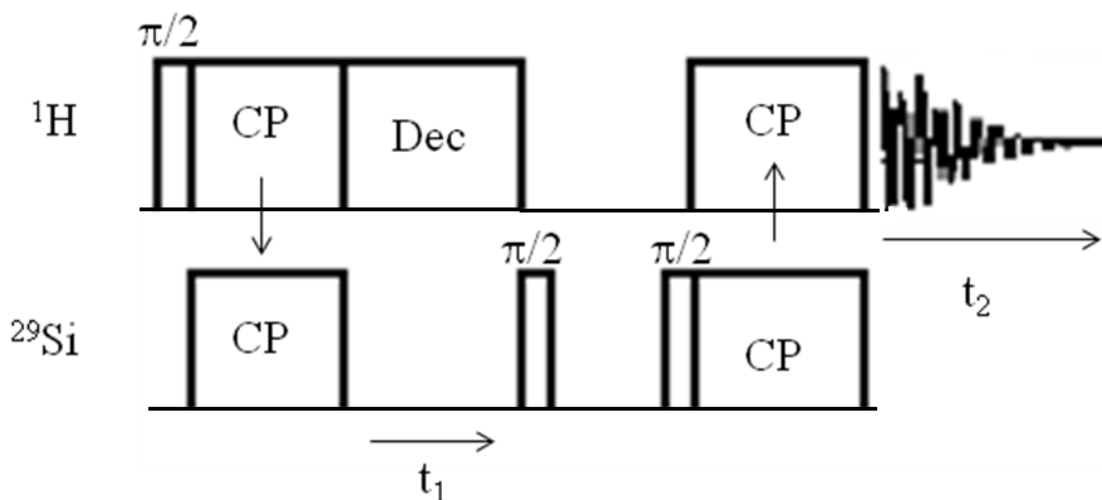


Figure 6.21. Pulse sequence for an indirect detection $\{^{29}\text{Si} \rightarrow ^1\text{H}\}$ HetCor technique.

The test sample used to demonstrate the signal enhancement of indirect detection techniques is a mixture of hexamethylbenzene and adamantane. These two compounds were used because of their differing ^{13}C locations and ^1H location, allowing for correlations within the compounds to be demonstrated and differentiated from each other. A direct detection measurement was made with cw (continuous wave) decoupling during the evolution period and detection and Hartmann-Hahn cross polarization during the mixing period. This is in contrast to above where Lee-Goldburg was used during the evolution period to reduce spin-diffusion. This will provide a spectrum for comparison with various indirectly detected pulse sequences. The contour plot using direct detection HetCor of the mixture of hexamethylbenzene and adamantane is shown in Figure 6.22. A slice was taken along the ^{13}C dimension for comparison with indirectly detected spectra, is shown in Figure 6.23. The S/N, as measured by the spectrometer, was determined to be 35.3.

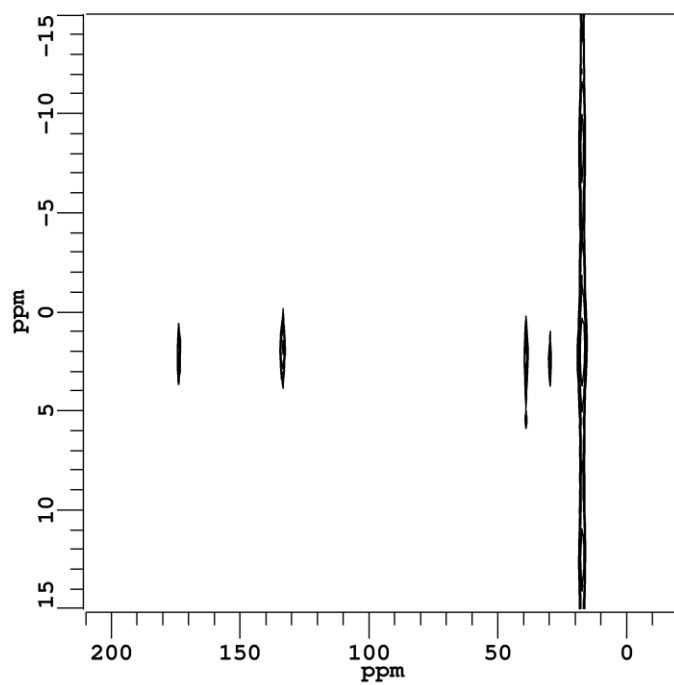


Figure 6.22. Contour plot of $\{^1\text{H} \rightarrow ^{13}\text{C}\}$ HetCor spectrum of a hexamethylbenzene and adamantane mixture, obtained using direct detection.

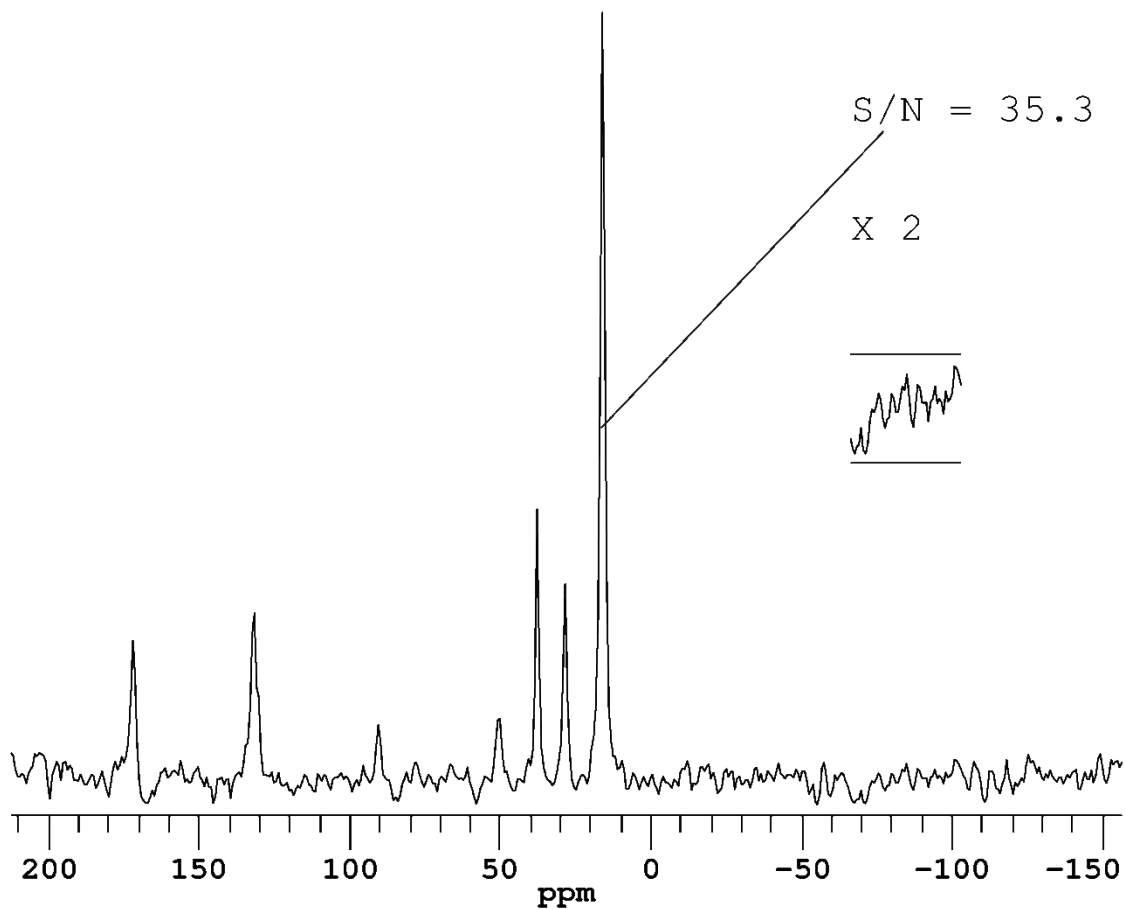


Figure 6.23. Slice, of HetCor spectrum shown in Figure 6.22, at a proton chemical shift of 2ppm.

The first test of the indirect detection sequence was evaluated was using the sequence shown in Figure 6.21 with ^{13}C decoupling during detection on a mixture of hexamethylbenzene and adamantane. The contour plot is shown below in Figure 6.25. A slice was taken from the ^{13}C dimension as shown in Figure 6.26 to compare to when the direct detection sequence was used and is seen in Figure 6.23. The S/N as determined by the computer is 69.4 for Figure 6.26; approximately twice as good as the S/N was in Figure 6.23. By visual observation, the S/N increase is slightly less than 2.

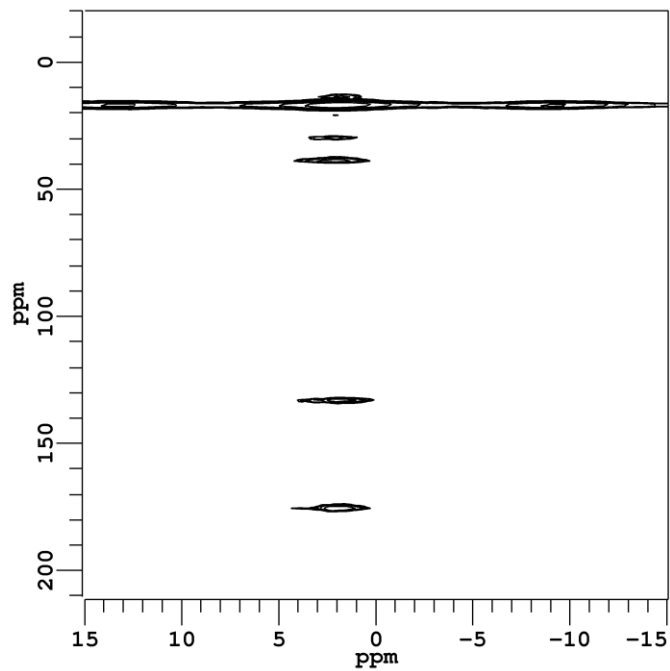


Figure 6.25. Contour plot of $\{^{13}\text{C}\rightarrow^1\text{H}\}$ HetCor spectrum obtained using indirect detection and with cw decoupling during detection, on a mixture of hexamethylbenzene and adamantane.

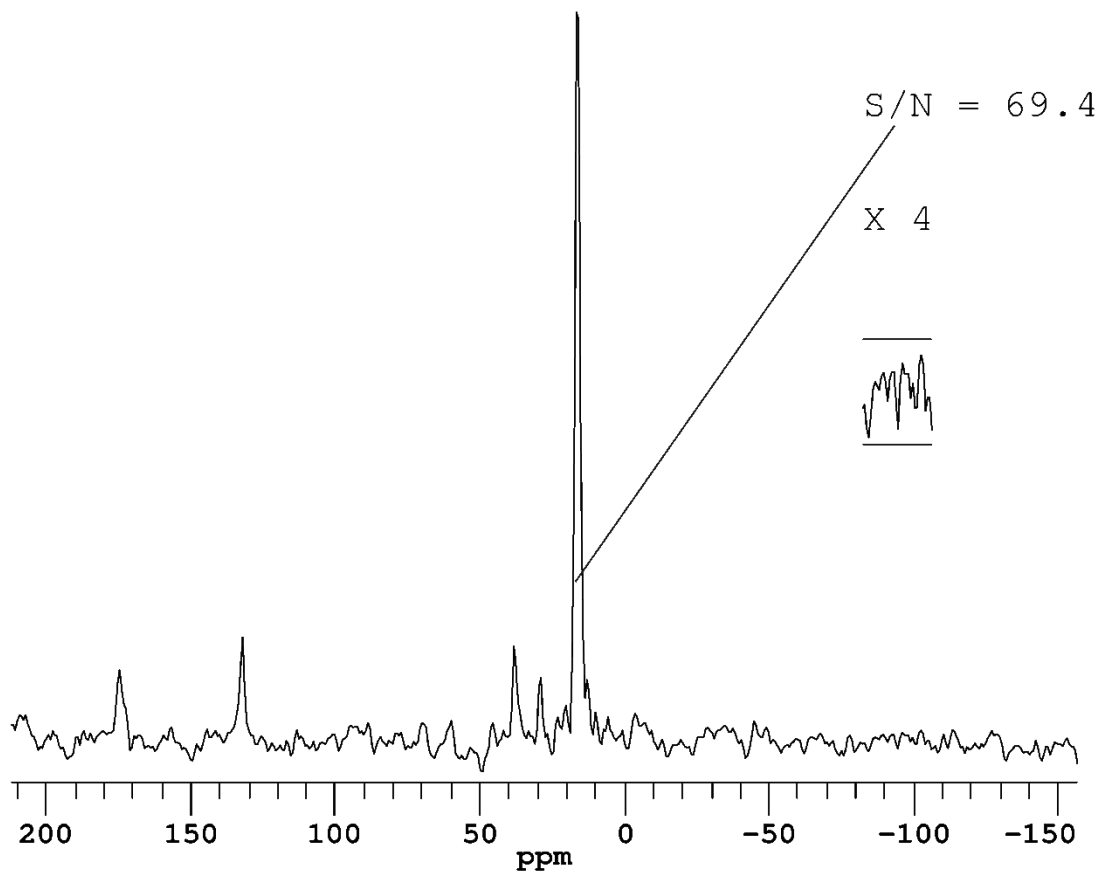


Figure 6.26. Slice, of the HetCor spectrum shown in Figure 6.25, at a ^1H chemical shift of 2ppm.

The second type of indirect detection sequence that was explored used two pulse phase modulation (TPPM) on ^{13}C during detection.⁷⁶ Two pulse phase modulation is a type of heteronuclear decoupling that is often implemented during detection to remove ^1H - ^{13}C coupling. The contour plot of an indirect detection sequence with TPPM decoupling on ^{13}C during detection is seen in Figure 6.27.⁷⁶ A slice through the ^{13}C dimension (Figure 6.28) of the indirect detection spectrum with TPPM during detection (Figure 6.27) shows a signal enhancement of greater than 2 over the spectrum shown in

Figure 6.23.⁷⁶ In a visual comparison of the spectra shown in Figure 6.28 and Figure 6.23 a significant improvement in S/N can be seen.

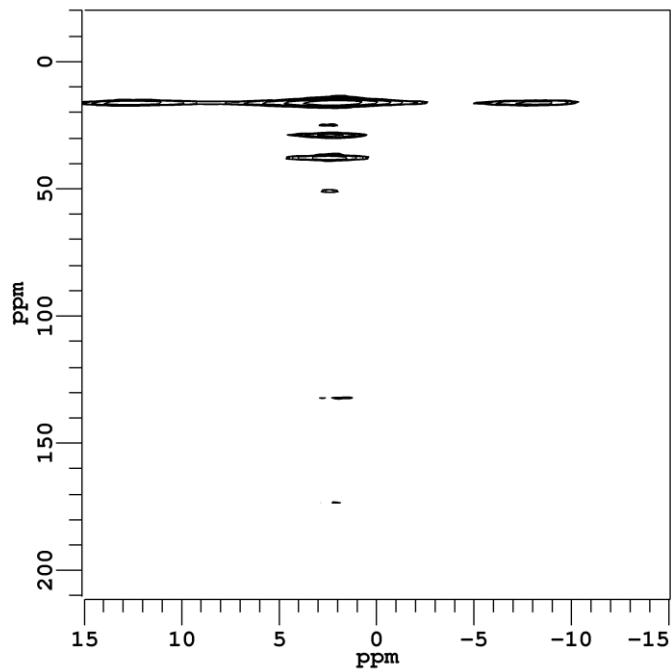


Figure 6.27. Contour plot of an indirect detection $\{^{13}\text{C} \rightarrow ^1\text{H}\}$ HetCor, obtained with TPPM decoupling during detection, on a mixture of hexamethylbenzene and adamantane mixture.

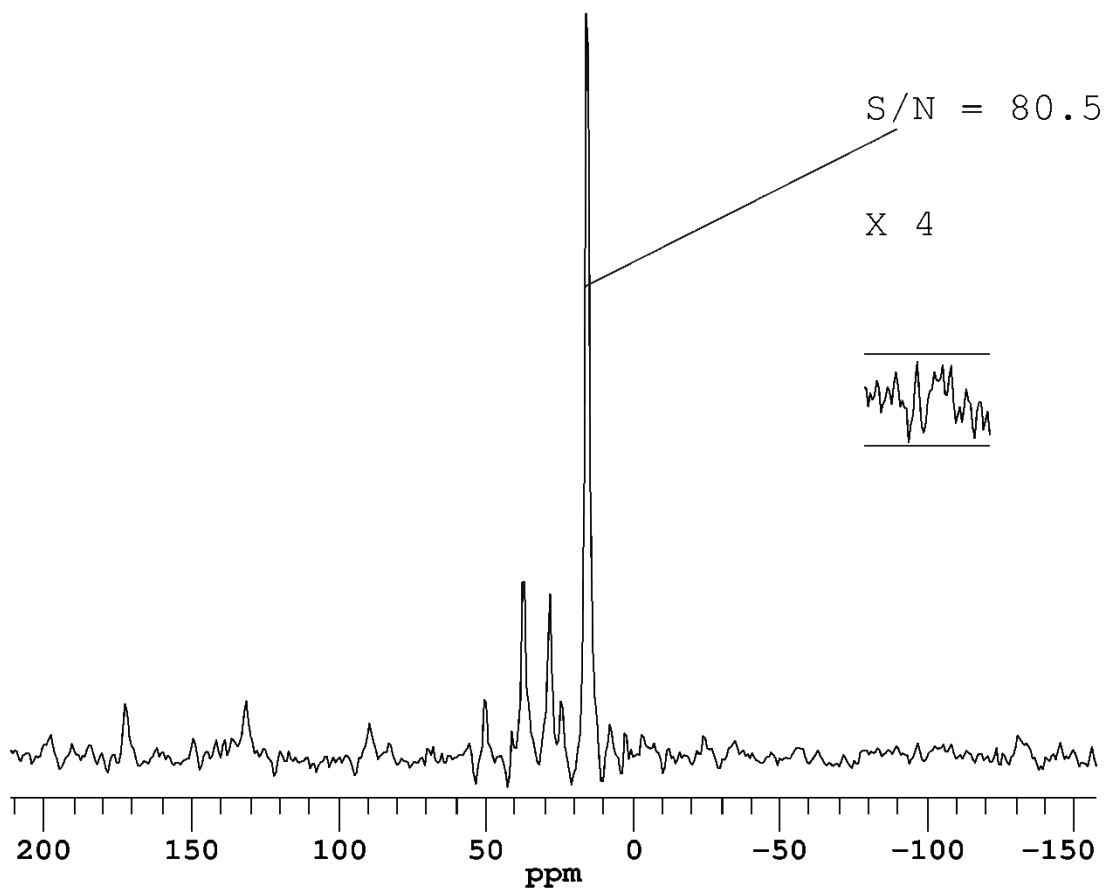


Figure 6.28. Slice, of the HetCor spectrum shown in Figure 6.27, at a proton chemical shift of 2 ppm.

A third type of decoupling during the detection period of the indirect detection sequence was evaluated: Spinal-64.⁷⁷ Spinal-64, or small phase incremental alteration, is a variant of TPPM. The contour plot for this pulse-sequence is shown in Figure 6.29. A slice through the ¹³C dimension is shown in Figure 6.30 and when compared to the slice through the ¹³C dimension of the direct detection spectrum (Figure 6.23) it can be determined that there is a S/N enhancement was over a factor of two.

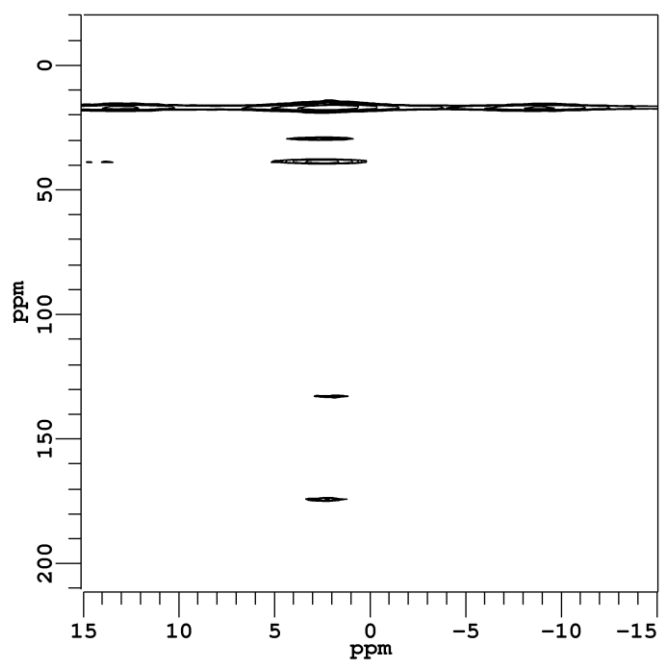


Figure 6.29. Contour plot of an indirect detection $\{^{13}\text{C} \rightarrow ^1\text{H}\}$ HetCor experiment, obtained with Spinal-64 decoupling during detection, on a mixture of hexamethylbenzene and adamantane.

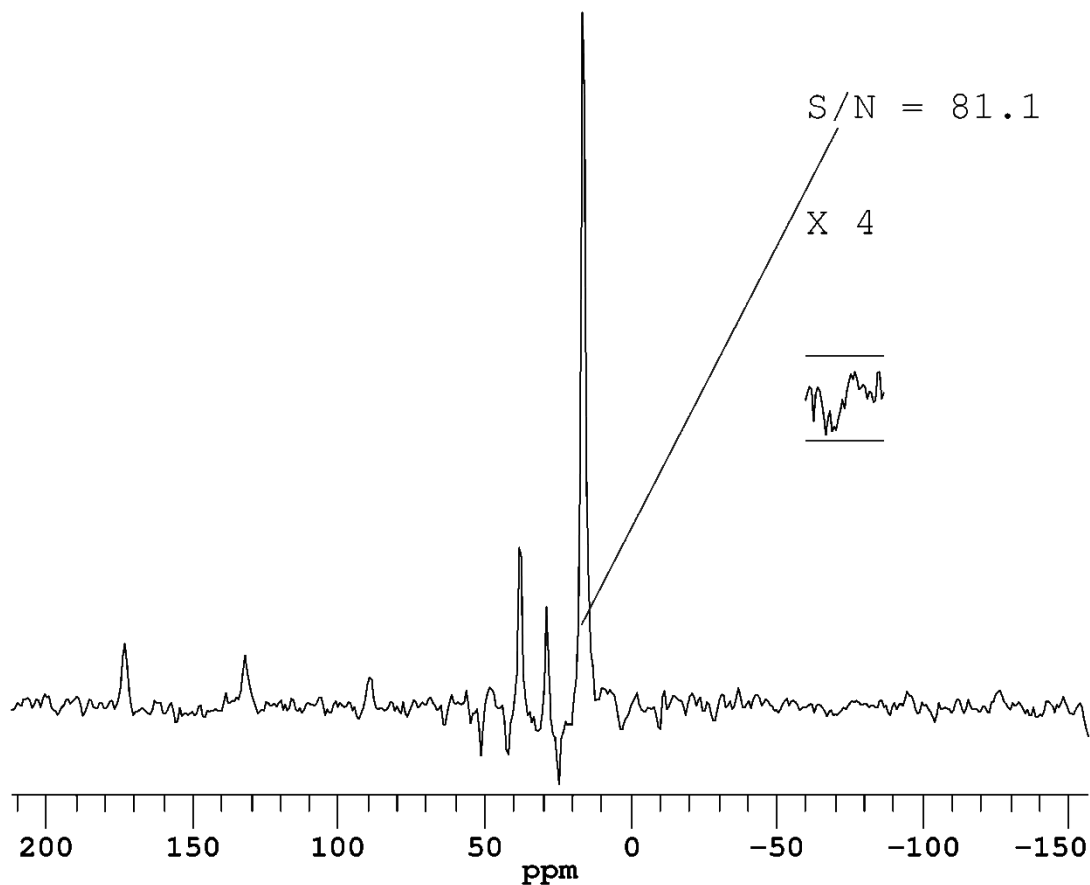


Figure 6.30. Slice, of the HetCor spectrum shown in Figure 6.29, at a proton chemical shift of 2ppm.

The use of Lee-Goldburg during the evolution period for indirect detection is likely not as necessary as it was in the direct detection version due to the fewer number of ^{13}C evolving and interfering with one another. Lee-Goldburg cross polarization can be incorporated into the second cross-polarization period to ensure selectivity in the cross polarization if necessary. It may also be possible to use a multiple pulse line narrowing technique, such as BR-24,⁷⁸ during detection to reduce ^1H - ^1H communication.

D. Overall summary of HetCor comparisons

A number of direct detection $^1\text{H} \rightarrow ^{29}\text{Si}$ HetCor experiments were compared, as shown in Figure 6.5 with the regions of interest shown in Figure 6.15. These included several techniques that are frequently used during direct detection HetCor, including Lee-Goldburg and a multiple-pulse technique, MREV8. It was concluded that the f_1 ridge was larger when LG was used during both the evolution period and the mixing period than when LG was used only during the evolution period, but when used during the mixing period LG allowed for better selectivity of directly bound protons, Si-H, pairs. It was also concluded that MREV8, was not advantageous enough to outweigh inherent difficulty of implementation. Through the use of a mixture of Q8M8_H/t-butyl trichlorosilane mixture the selectivity of the sequences was verified. A comparison of the difference sequences (Figure 6.5) is shown in Figure 6.15 and for our purposes the pulse sequence that best suits our interest is Lee-Goldburg during the evolution with either Hartmann-Hahn cross-polarization (Figure 6.5A) or Lee-Goldburg cross polarization (Figure 6.5B) depending on whether it is necessary to use a cross polarization technique that suppresses spin-diffusion.

In a comparison of direct detection $^1\text{H} \rightarrow ^{13}\text{C}$ HetCor experiments and indirect detection $^{13}\text{C} \rightarrow ^1\text{H}$ HetCor a signal enhancement of 2 was achieved, approximately what is expected. A number of decoupling techniques during indirect detection HetCor were also compared. CW decoupling, TPPM, and SPINAL-64 were each compared to reduce heteronuclear coupling. It was found that the multiple pulse techniques of TPPM and SPINAL-64 were advantageous over CW decoupling, but did not have significant advantages over each other.

References:

- (1) Bleyakov, V. A.; Burdor, V. A. *Phys. Lett. A* **2007**, *367*, 128.
- (2) Caravatti, P.; Bodenhausen, G.; Ernst, R. R. *Chem. Phys. Lett.* **1982**, *89*, 363.
- (3) Burum, D. P.; Bielecki, A. *J. Magn. Reson.* **1991**, *94*, 645.
- (4) Bronnimann, C. E.; Ridenour, C. F.; Kinney, D. R.; Maciel, G. E. *J. Magn. Reson.* **1992**, *97*, 522.
- (5) Burum, D. P.; Linder, M.; Ernst, R. R. *J. Magn. Reson.* **1981**, *44*.
- (6) Lee, M.; Goldberg, W. I. *Phys. Rev.* **1965**, *140*, 1261.
- (7) Burum, D. P.; Bielecki, A. *J. Magn. Reson.* **1991**, *94*, 184.
- (8) Moran, M.; Casado, C. M.; Cuadrado, I. *Organomet.* **1993**, *12*, 4327.
- (9) Bronnimann, C. E.; Hawkins, B. L.; Zhang, M.; Maciel, G. E. *Anal. Chem* **1988**, *60*, 1743.
- (10) Mishkovsky, M.; Frydman, L. *Chem. Phys. Chem.* **2004**, *5*.
- (11) Khitrin, A. K.; Fung, B. M. *J. Magn. Reson.* **2001**, *152*, 185.
- (12) Ishii, Y.; Tycko, R. *J. Magn. Reson.* **2000**, *142*, 199.
- (13) Cavadini, S.; Antonijevic, S.; Lupulescu, A.; Bodenhausen, G. *Chem. Phys. Chem.* **2007**, *8*, 1363.
- (14) Bennett, A. E.; Rienstra, C. M.; Auger, M.; Lakshmi, K. V.; Griffin, R. G. *J. Chem. Phys.* **1995**, *103*, 6951.
- (15) Fung, B. M.; Khirtrin, A. K.; Ermolaev, K. *J. Magn. Reson.*, **2000**, *142*, 97.
- (16) Barbara, T. M.; Baltusis, L. *J. Magn. Reson.* **1994**, *106*, 182.

CHAPTER 7

General Conclusions Regarding the Silicon Surface

It was quickly evident that silicon wafers were not going to have sufficient surface area to be studied by ssNMR via standard ^{29}Si CP/MAS and ^1H DP/MAS techniques. Development of a specialized, low-temperature apparatus was not going to be possible in the time frame of this project. Because of this, other types of silicon samples with higher surface areas were studied; it was hoped that these other types of silicon samples would have similar structural features on the surface. These other silicon materials are hydride-capped silicon powder, synthesized silicon nanoparticles (supposedly methoxy-capped), and commercially available hydride-capped silicon nanoparticles (*np*-Si). The sample providing the most conclusive insight to the surface moieties on the silicon surface as studied by ssNMR was the commercially available hydride-capped silicon nanoparticles (*np*-Si).

As shown in Chapter 5, the combination of ^{29}Si and ^1H chemical shift results and time-domain NMR data (based on magnetic dipole-dipole interactions) yielded for *np*-Si a self-consistent interpretation of the surface chemical structure of *np*-Si and various treated *np*-Si samples. This combination of NMR-derived information leads to a picture of the surface of as-received *np*-Si as consisting of a dominant contribution of a Si-H

layer, with a small but significant contribution of surface silanols; these types of ‘surface sites’ are connected to a crystal-like silicon core by Si-O-Si bridges and Si-Si bonds.

When a $\text{H-Si}(-\text{Si})_3$ surface is oxidized, the formation of $\text{H-Si}(-\text{Si})_n(-\text{O-Si})_{3-n}$ is energetically favored, compared to formation of a surface hydroxyl, i.e., $\text{H-O-Si}(-\text{Si})_3$, configuration. Thus, the broad -80 ppm contribution that is dominant in the ^{29}Si CP/MAS spectra of samples that have not been deliberately oxidized (500°C O_2) (Figure 5.3) is assigned to a monohydride silicon atoms that are each bonded to three bridging oxygen atoms, $(\text{Si-O})_3\text{Si-H}$ (with intensity probably centered at about -85 ppm), and the related $(\text{Si-O})_2\text{Si(H)OH}$ sites (with intensity centered at about -75 ppm); these assignments are supported by quantum mechanical calculations of ^{29}Si chemical shifts. Such calculations also suggest that a ^{29}Si CP/MAS spectral contribution at about -14 ppm in the spectrum of unmodified *np*-Si may be due to structures of the type $(\text{Si-O})_2\text{Si(H)}(-\text{Si})$ and/or $(\text{Si-O})\text{Si(H)}(-\text{Si})_2$. Comparing integrated intensities of the various contributions to the ^{29}Si CP/MAS spectra of 150°C evacuated *np*-Si (Table 5.1) suggest the following qualitative order of site populations: $(\text{Si-O})_3\text{Si-H} >$ sites with the same ^{29}Si chemical shift (-99 ppm) as $(\text{Si-O})_3\text{SiOH}$ (which is included as a small contribution) $>$ $(\text{HO})_n\text{Si}(\text{Si})_m(-\text{OSi})_{4-m-n} \sim (\text{Si-O})_2\text{Si(H)OH} >$ sites with the same ^{29}Si chemical shift (-89 ppm) as $(\text{Si-O})_2\text{Si}(-\text{OH})_2$ (which is included as a small contribution) $>$ sites with the ^{29}Si chemical shift of $(\text{Si-O})_4\text{Si}$ (-109 ppm). A combination of ^1H and ^2H MAS experiments (Figures 5.4, 5.5, and 5.8) provide strong evidence for small contributions of silanol groups, along with the dominant Si-H sites, on the surface of unmodified *np*-Si; these silanol sites are dramatically increased by deliberate oxidation (500°C O_2).

This combination of experiments provides a self-consistent view of the generation or elimination of silanols under hydrolysis, oxidation and condensation reactions. It would be expected that Si-H bonds on the surface of a hydride-capped silicon nanoparticle would react similarly to Si-H of a hydride-capped silicon powder, as well as a hydride-capped silicon wafer, resulting in similar surface moieties on hydride-capped silicon surfaces.

A potentially useful technique for detecting directly bound ^1H - ^{29}Si is $^1\text{H} \rightarrow ^{29}\text{Si}$ Heteronuclear Correlation Spectroscopy (HetCor). While its applicability has been demonstrated in this project with reference compounds, the direct-detection $^1\text{H} \rightarrow ^{29}\text{Si}$ HetCor technique was clearly not going to be applicable to *np*-Si due to its low surface area ($\sim 86.3 \text{ m}^2/\text{g}$) and the resulting time requirements. While the use of indirect-detection $^{29}\text{Si} \rightarrow ^1\text{H}$ HetCor provided a signal enhancement of 2, time was still going to be a limiting factor. To run an indirect-detection $^{29}\text{Si} \rightarrow ^1\text{H}$ HetCor experiment with S/N in the direct dimension comparable to that of Figure 6.7 would take ~ 45 days. Due to instrumental limitations, this experiment would likely not be possible. Optimization of the indirect detection $^{29}\text{Si} \rightarrow ^1\text{H}$ HetCor technique, such as in the magnetization storage step, has the potential for improvement by reducing the loss of magnetization and increasing the likelihood of applicability to *np*-Si. As with all of these experiments, working with smaller nanoparticles, therefore increasing the surface area, increases the applicability of the technique.

APPENDIX I

Saving Transverse Magnetization

The contents of this chapter are a reformatted paper titled Saving Transverse Magnetization published in Solid State Nuclear Magnetic Resonance, Volume 36, Issue 4, Pages 202-208.

Saving Transverse Magnetization

Takeshi Kobayashi, Joseph A. DiVerdi, Rebecca A. Faulkner, and Gary E. Maciel*

Department of Chemistry, Colorado State University, Fort Collins, Colorado 80523 USA

Corresponding author: E-mail: gary.maciel@colostate.edu,

Tel: +1-(970) 491-6480. Fax: +1-(970) 491-1801.

Key Word: magnetization storage, transverse magnetization, Carr-Purcell sequence, store-and-restore

Overview.

A magnetization storage sequence, ALT-1 (Alternating Longitudinal and Transverse components), is reported. The ALT-1 sequence is a hybrid of two types of storage sequences, the Carr-Purcell type and store-and-restore sequences. During incremental storage periods within the ALT-1 sequence, essentially half of the initially

transverse magnetization is stored along the z axis and the other half is prolonged by an echo-generating pulse. The portions of initial magnetization that are stored as longitudinal components or transverse components are alternated by a $\pi/2$ pulse during the cycle. Both transverse components of the initial magnetization are treated the same in the ALT-1 sequence and orientational (phase) information of the initial magnetization is kept during the storage period. The ALT-1 sequence can preserve magnetization more effectively than a published class of modified Carr-Purcell type sequences, because essentially half of the magnetization during incremental storage periods is not subjected to relaxation from T_2 effects.

Introduction.

In some NMR techniques one wish is to ‘save’ or ‘store’ transverse magnetization at some stage of an experiment and subsequently have it available for further manipulation and/or detection. Typically the ‘storage period’ is introduced in order to permit the imposition of some operation that is time consuming, relative to the time scale of normal spin evolution, especially in solid-state NMR experiments. Such operations have included hopping of a rotor about the magic angle⁷⁹⁻⁸¹, flipping of a rotor axis⁸²⁻⁸⁵, reorienting a single crystal⁸⁶, switching gradients^{87,88} and remote-sensing NMR^{89,90}, and could be any change of conditions that one wishes to impose on the sample during the NMR experiment. In such cases the effectiveness of the ‘saving/storage’ technique in preserving the transverse magnetization over a desired time span is of crucial importance.

The earliest and most commonly applied methods for preserving or prolonging transverse magnetization by reducing a loss of magnetization due to inhomogeneous

effects have been based on a series of π pulses, typically some version of a Carr-Purcell sequence⁹¹⁻⁹³. The various modifications or elaborations of pulse sequences of the Carr-Purcell type typically differ in terms of the phases and ‘clustering’ of the π pulses involved and have been aimed at compensating for errors in pulse duration and/or phasing and for preserving more equally the two orthogonal components of a transverse magnetization. While such techniques can be effective for preserving transverse magnetization for periods much less than the characteristic T_2 values of the sample, these techniques lose a substantial fraction of the initial magnetization if the storage period equals or exceeds the relevant T_2 s.

An alternative type of method for the ‘storage’ of transverse magnetization is a combination of a $\pi/2$ pulse, which places one component of the initially transverse magnetization along the z axis for ‘storage’ for a period, τ_s (during which the other transverse magnetization component is destroyed by dephasing), after which one applies another $\pi/2$ pulse (of complementary phase) to restore the saved magnetization component back to the transverse plane⁷⁹⁻⁸⁵. This type of sequence has the feature that the ‘stored’ magnetization is not subjected to transverse relaxation (a major issue for solid samples) and instead is constrained only by longitudinal relaxation, which is typically much slower for solids; this method encodes the phase of the stored magnetization by selecting just one component. This sequence also suffers from the inescapable loss of nominally half of the available transverse magnetization, because half of it is sacrificed during the storage/dephasing period, τ_s .

Some experiments require, or at least benefit from, treating both transverse components of magnetization ‘the same’⁹⁴; yet a ‘storage’ sequence (e.g., the Carr-Purcell-Meiboom-Gill pulse sequence) may preserve well only one component of transverse magnetization⁹¹, because it loses one component due to an accumulation of the effects of imperfect π pulses. A class of pulse sequences of the Carr-Purcell type, such as XY-4⁹², XY-8 and XY-16⁹³, which use π pulses of both x and y phases, have been shown to compensate both components of magnetization equally for π pulse errors.

The ALT-1 sequence presented here is essentially a hybrid of the two types of storage sequences described above. In the ALT-1 sequence, essentially half of the initially transverse magnetization is stored along the z axis during any of the periods between pulses in the sequence and essentially half is subjected to T_2 effects.

Experimental.

NMR Experiments. Experiments were carried out at 50.2 MHz mainly on hexamethylbenzene (HMB, Aldrich) in a 9.5 mm (ID) Magic-Angle-Hopping (MAH)⁷⁹⁻⁸¹ rotor in a CP-MAH probe and in a 7.5 mm (ID) Magic-Angle-Spinning (MAS) rotor in a CP/MAS probe, using a modified 200 MHz (¹H) spectrometer of the Chemagnetics-Otsuka CMX-II type (Otsuka Electronics, now Varian, Fort Collins, CO). The MAH probe was employed for static or slow-spinning experiments. Solid-state ¹³C spectra were obtained by complex Fourier transformation of the sampled complex data and subsequent apodization with 50 Hz Lorentzian line broadening. The pulse durations were 5 and 10 μ s for the $\pi/2$ and π pulses, respectively. The contact time was 5 ms. The

recovery time used was 1.5 s. ^{13}C chemical shifts are reported in parts per million, referenced to liquid TMS (0.0 ppm).

Sample Preparation. A rose stem was dehydrated by freeze-drying; the rose stem was cooled by liquid nitrogen followed by evacuation (10^{-4} atm) overnight at dry-ice temperature (ca. -80 °C). Then, the rose stem was rehydrated with a 10 % solution of ^{13}C labeled methanol (99.9 atom %, Cambridge isotopes, MA) in water.

Results and Discussions.

Magnetization Storage for Static Samples. Figure AI.1 shows the sequence for the new technique, ALT-1, designed to preserve or prolong transverse magnetization. In the study presented here, the ‘initial’ transverse magnetization is generated by ^1H - ^{13}C cross polarization and preserved/prolonged by the ALT-1 sequence, although some other means (e.g., a single $\pi/2$ pulse) could be used to generate the initial transverse magnetization. The sequence consists of a repetitive cycle of two π pulses and two $\pi/2$ pulses, each with a suitably chosen phase, with time intervals τ inserted between each (π - $\pi/2$) pair of pulses. The repetitive sequence is initiated by a prior $\pi/2(-y)$ pulse and, after N repetitions of the sequence, it is terminated by a ‘final’ $\pi/2(y)$ pulse. For some applications of the ALT-1 sequence, the magnetization storage period may be preceded by additional operations and these operations may generate both x and y magnetization components⁷⁹⁻⁸¹. In such cases, the store pulse will put one component of the initially transverse magnetization along the z -axis and leave the other component in the transverse plane. The component left in the transverse plane is saved from inhomogeneous

dephasing by the first echo-generating π pulse. Then, the transverse component and the longitudinal component are alternated by the $\pi/2(x)$ pulse that follows. In the second cycle of the $\pi/2$ pulse phase cycling, the transverse component that was previously a longitudinal component is saved by the second echo-generating $\pi(y)$ pulse, and those two components are alternated again by the $\pi/2(x)$ pulse that follows. This sequence is repeated during the storage period, $\tau_s = N \times \tau_{\text{cycle}}$.

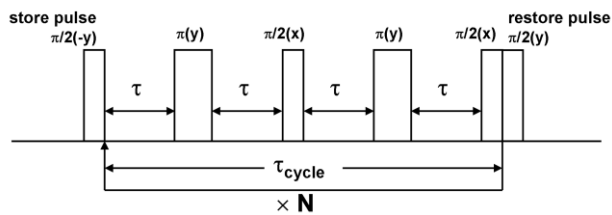


Figure AI.1. The pulse sequence, ALT-1, for preserving transverse magnetization without ^1H decoupling during the storage period, shown for the case of ‘initial’ transverse magnetization generated by cross polarization.

Figure AI.2 shows a vector diagram corresponding to the pulse sequence of Figure AI.1, based on the assumptions of no relaxation and infinitely short pulses. One sees that, for these assumptions, the ‘final’ $\pi/2(y)$ pulse regenerates the same transverse magnetization at time $a + 4\tau$ as existed at time a , just prior to the initial $\pi/2(-y)$ pulse that triggered the repetitive cycle. For each period τ , one component of the initially transverse magnetization is positioned along the z axis (and ‘safely’ in storage), while the other initially transverse component is placed along the x or y axis (of the rotating frame) and subject to partial, irreversible loss via homogeneous T_2 effects. Hence, qualitatively, one might hope that the overall preservation of initially transverse magnetization from time a would be somewhere between ‘perfect’ preservation and the preservation

efficiency of a $\pi/2 - \tau_s - (-\pi/2)$ store-and-restore approach⁷⁹⁻⁸⁵, which completely eliminates one of the initially transverse magnetization components. Of course, if the total storage period, $\tau_s = N \times (4\tau)$, is sufficiently long, both initially transverse components will be eliminated, because both components will in turn have been subjected to a long period of transverse relaxation.

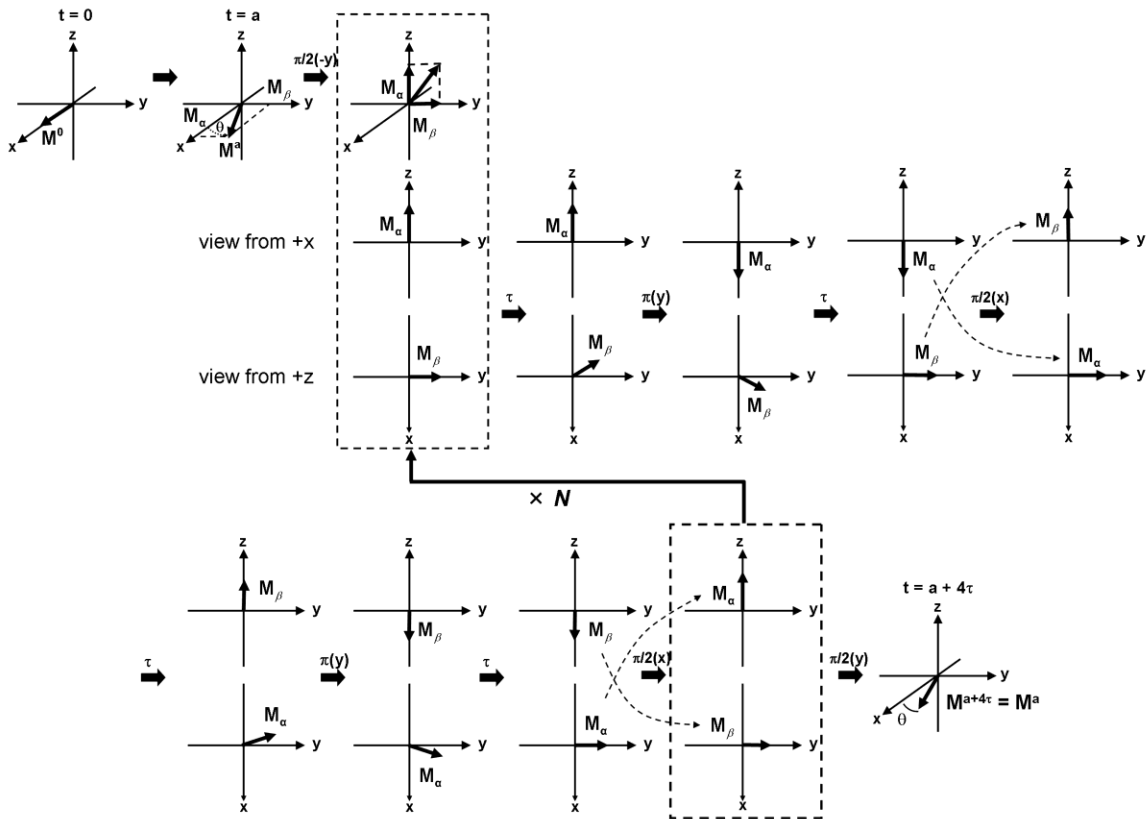


Figure AI.2. Vector diagram corresponding to ALT-1. M_α and M_β represent two orthogonal components of the ‘initial’ transverse magnetization, which is along the x or the y axis at $t = a$. In order to demonstrate that both transverse components of the initial magnetization are treated the same, an evolution period is inserted between the cross polarization period and the initial $\pi/2$ pulse (resulting in a phase accumulation, θ).

Figure AI.3 shows a comparison of the ‘storage efficiency’ of the ALT-1 sequence (Figure AI.3A and AI.3B), as represented by the ^{13}C NMR spectrum of static

hexamethylbenzene (HMB), as a function of storage time, τ_s , with the storage efficiency of a published sequence, XY16 (Figure AI.3C and AI.3D)⁹³ and the store-and-restore sequence (Figure AI.3E and AI.3F). The cycle time, τ_{cycle} , was 100 μs in the ALT-1 sequence and in the XY16 sequence. The pulse spacing, τ , was 17.5 or 7.5 μs for the ALT-1 sequence or the XY16, respectively.

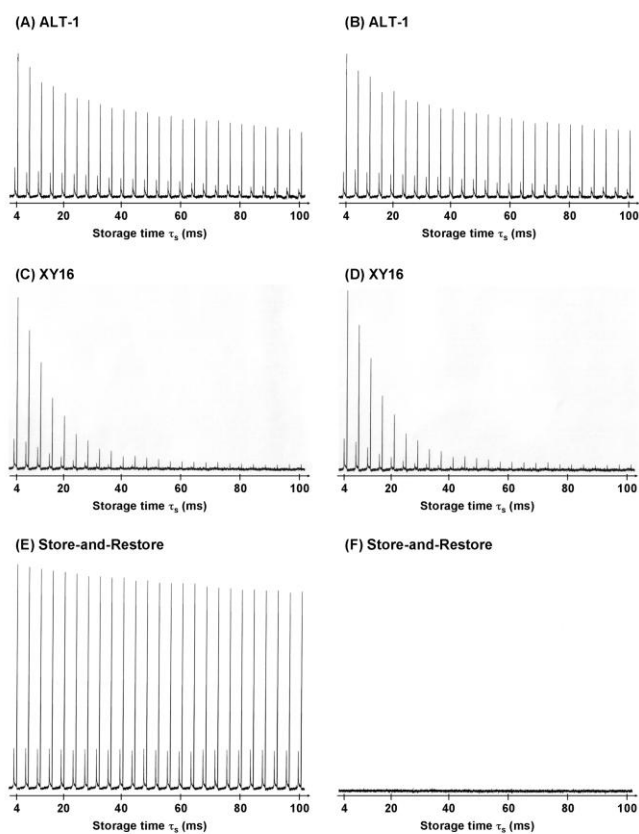


Figure AI.3. Comparison of the spectral intensities of the ^{13}C NMR spectrum of static hexamethylbenzene (HMB) as a function of storage time, τ_s . Phases of the initial transverse magnetizations differ by 90° between the left (A, C, E) and the right-hand (B, D, F) columns. The storage time τ_s is increased from 4.0 to 100 ms with 4.0 ms increments. Cycle times, τ_{cycle} , for ALT-1 and the XY16 were 100 μs .

In Figure AI.3, the phase of the ‘initial’ transverse magnetization (as determined by the phase of cross polarization at the beginning of the sequence shown in Figure AI.1)

differs by 90° between the left (A, C, E) and the right (B, D, F) columns. The storage time τ_s was varied from 4.0 to 100 ms by varying N; these values correspond to 40 to 1000 repetitions of the ALT-1 sequence ($\tau - \pi - \tau - \pi/2 - \tau - \pi - \tau - \pi/2$) or 10 to 250 repetitions of the XY16 sequence ($\tau - \pi - \tau - \tau - \pi - \tau - \dots$). One sees in Figure AI.3, as expected, that the ALT-1 sequence and the XY16 sequence preserve both components of the transverse magnetization equally, while the store-and-restore sequence completely eliminates one of the transverse components and preserves the other component very well. The storage efficiency for either component of the ALT-1 sequence or the XY16 sequences is lower than that of the surviving component of the store-and-restore sequence even for the shortest storage time ($\tau_s = 4.0$ ms), because of T_2 relaxation and an accumulation of the effects of imperfect pulses during the storage periods. The store-and-restore sequence, however, completely loses one component. In practice, the net magnetization storage efficiency is a combination of the efficiencies of *both* components.

Figure AI.4 plots the spectral area of the ^{13}C NMR spectrum of static HMB as a function of the storage time. In some techniques, e.g., Magic-Angle-Hopping⁷⁹⁻⁸¹, an ‘initial’ transverse magnetization right before the storage period could be anywhere in the transverse plane as a result of evolution. One sees that half of the spectral intensity is maintained by the ALT-1 sequence for a storage time of about 50 ms and the ALT-1 sequence with the cycle time $\tau_s = 100$ μs has higher storage efficiency than that of the store-and-restore sequence for total storage times up to about 40 ms. The ALT-1 sequence provides much higher magnetization storage efficiency than the XY16 sequence. During the storage period of the XY16 sequence, both components of the

initial magnetization are subjected to T_2 relaxation, while in the ALT-1 sequence essentially half of the magnetization is not subjected to transverse relaxation during storage periods.

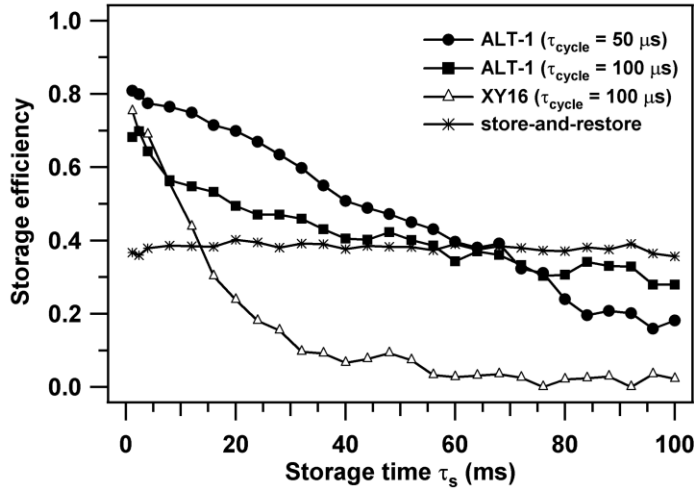


Figure AI.4. Comparison of storage efficiencies (in terms of the total area of the static HMB spectrum) for various magnetization storage sequences, as a function of storage time τ_s .

Figure AI.4 shows that the storage efficiency of the ALT-1 sequence is improved, for storage periods of 60 ms or less, by reducing the cycle time from 100 μs to 50 μs and the efficiency of this sequence is higher for $\tau_s = 50$ ms than that of the store-and-restore sequence. The storage efficiency of the ALT-1 sequence with the cycle time of 50 μs falls off more quickly than that of the same sequence with a cycle time of 100 μs , for storage times greater than about 80 ms. This is likely due to a larger number of pulses in the ALT-1 sequence for the shorter cycle time, potentially causing a larger cumulative effect of pulse (e.g., flip-angle) errors.

As represented in Figures AI.3 and AI.4, the ALT-1 magnetization storage sequence demonstrates higher storage efficiency than the store-and-restore or the XY16

sequences in a static solid sample for modest storage periods, e.g., 50 ms. The magnetization storage efficiency of the ALT-1 sequence in samples undergoing motion is also of interest in the context of a broad range of possible applications. This avenue is discussed in the following sections.

Effects of Molecular Motion. In the experimental results on HMB samples presented up to this point, ^1H decoupling was not included during the storage period. Methyl groups of HMB execute fast rotational motions about the C-CH₃ (C₃) axis and the entire HMB molecule undergoes a reorientational motion about its hexad axis (C₆),^{95,96} so that ^1H - ^{13}C dipole-dipole interactions are partially averaged. Assuming that the motions are continuous rotations and using 1.1 Å and 50° for the C-H bond distance and the angle between the C-H bond axis and the C₃ axis, respectively, one obtains a value of 1.4 kHz for the residual (averaged) ^{13}C - ^1H dipole-dipole coupling constant within the methyl group^{97,98}. For the dipole coupling between a methyl proton and an aromatic carbon, a value of 1.0 kHz for the residual coupling constant is obtained (C...H distance: 2.2 Å; 25° for the angle between the C₃ axis and the C_{aromatic}-H).

In the experiments reported here, the cycle time of the ALT-1 sequence is 100 μs, which corresponds to a 10 kHz frequency. This frequency is much larger than the frequencies that correspond to the residual ^1H - ^{13}C dipole-dipole couplings estimated above, so one expects that the dipole-dipole interaction is decoupled by the train of ^{13}C rf pulses used for magnetization storage. In many samples, the relevant ^1H - ^{13}C dipole-dipole interactions are much larger and whether they could be decoupled by the ^{13}C rf pulses used in the ALT-1 sequence is questionable. For those cases, using a shorter cycle

time or introducing ^1H decoupling during the storage period would be possible strategies; however, the former strategy could result in a larger cumulative effect of pulse errors. For the latter case, the ^1H - ^{13}C dipole-dipole interactions must be decoupled by mismatched decoupling during the ^{13}C pulses or no ^1H decoupling pulse during the ^{13}C rf pulses, in order to avoid a cross polarization between ^1H and ^{13}C during the storage period.

Magnetization storage under Magic-Angle-Spinning. The magnetization storage efficiency achieved using the ALT-1 sequence was measured on a HMB sample as a function of storage time, with various MAS rates. A priori, one expects the storage efficiency to be decreased by MAS, because the storage mechanism of transverse components over τ periods of the sequence shown in Figure AI.1 depends on the constancy of chemical shifts over each τ period. Figure AI.5 shows the storage efficiencies under MAS conditions with various spinning rates. One sees in Figure AI.5 that, as expected, the storage efficiency is attenuated by MAS to an extent that increases more or less monotonically with MAS speed (ω_r), except at $\omega_r = 5.0$ kHz, up to about 6 or 7 kHz; for large storage periods (> 60 ms) the storage efficiency at a MAS speed of 7.0 kHz is almost equivalent to that at 6.0 kHz. However, the storage efficiency at a MAS speed of 5.0 kHz is much lower than in these two cases.

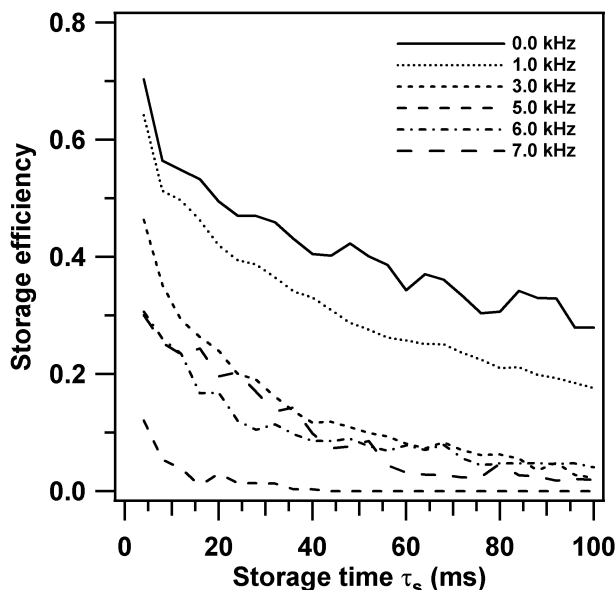


Figure AI.5. Effect of sample spinning on storage efficiency by ALT-1 on HMB. The experiments were carried out with the cycle time $\tau_{\text{cycle}} = 100 \mu\text{s}$, at 50.2 MHz using 7.5 mm MAS rotors. The storage efficiency was measured in terms of spectral area relative to the corresponding spectral area for $\tau_s = 0$.

Ideally, an initial transverse magnetization returns to its original position (before starting a cycle) after one complete cycle. However, as indicated above, sample rotation causes the chemical shifts to vary over the cycle and an echo-generating π pulse no longer works efficiently to generate an echo after one storage period. Another possible interference effect could occur between the physical rotation of the sample and the nutation of the spin magnetization induced by the applied rf field, i.e., rotary resonance, which can be expected under MAS conditions when a decoupling frequency (ω_{decouple}) is equal to an integral multiple of the MAS speed, $\omega_{\text{decouple}} = n\omega_r$ ($n = 1, 2$).^{99,100} The train of ^{13}C rf pulses with a cycle time of 100 μs functions as a form of ^1H - ^{13}C decoupling, with a characteristic frequency of 10 kHz. Spinning rates at which a rotary resonance

recoupling effect may be expected include $\omega_r = 5.0$ kHz, corresponding to the $n = 2$ case. Under this situation, ^1H and ^{13}C spins are partially recoupled by rotary resonance, the ^{13}C spins undergo enhanced dipolar dephasing and the magnetization storage efficiency is further attenuated by the rotary resonance recoupling. Thus, the patterns seen in Figure AI.5, a monotonic decrease of storage efficiency with increasing MAS speed, can be interpreted as ‘converging’ for a MAS speed of about 3-4 kHz, except for the rotary resonance condition at 5.0 kHz. Presumably, if the MAS speed were increased to a value at which MAS averaging of CSA effects begins to approach the effectiveness of Brownian motion in liquids, then the system will start to behave as a liquid under magnetizations storage sequences (*vide infra*).

Magnetization storage in a liquid. A solid sample is usually spun rapidly about the magic-angle axis in order to average its chemical shift anisotropy and/or decouple dipole-dipole interactions. Even for a liquid phase, in which molecules execute rapid, isotropic motions and hence exhibit no such effects, semi-solid samples are often spun at several tens of Hz for averaging inhomogeneities in the effective static magnetic field, e.g., as caused by inhomogeneities in bulk magnetic susceptibility. In this way, NMR has been utilized for the study of liquid phases in a variety of inhomogeneous semi-solid matrices, e.g., especially biological tissues. In the present study, the effectiveness of the ALT-1 sequence was examined in the NMR of liquid-state molecules absorbed in a solid matrix; the model chosen here for this examination is aqueous methanol absorbed in a rose stem. This system was examined under low MAS speed as a function of storage time, and the storage efficiency of various magnetization storage sequences were compared.

Figure AI.6 shows plots of the storage efficiency (in terms of total spectral area) of the ^{13}C NMR spectrum of methanol adsorbed in a rose stem as a function of the storage time. When the sample is static (A), the storage efficiency of the ALT-1 sequence is higher than that of the store-and-restore sequence up to a storage time of about 80 ms, because no portion of the initial transverse magnetization is intentionally sacrificed in the ALT-1 sequence (or in XY16). The ALT-1 sequence maintains a storage efficiency greater than 0.5 for a storage time of about 80 ms. The storage efficiency of the XY16 sequence is almost equivalent to that of the ALT-1 sequence in the static case and does not fall off quickly, unlike the case of a static HMB sample, as represented in Figure AI.4. The ALT-1 sequence also demonstrates better storage efficiency for the methanol sample than that for the HMB sample. This is due to the much larger T_2 values of the liquid sample relative to the storage period. The XY16 sequence keeps the initial magnetization in the transverse plane and the magnetization is subject to T_2 relaxation throughout the entire storage period. It is not surprising that both the XY16 sequence and the ALT-1 sequence work relatively well in the case of a sample having T_2 values that are large compared to the storage periods examined.

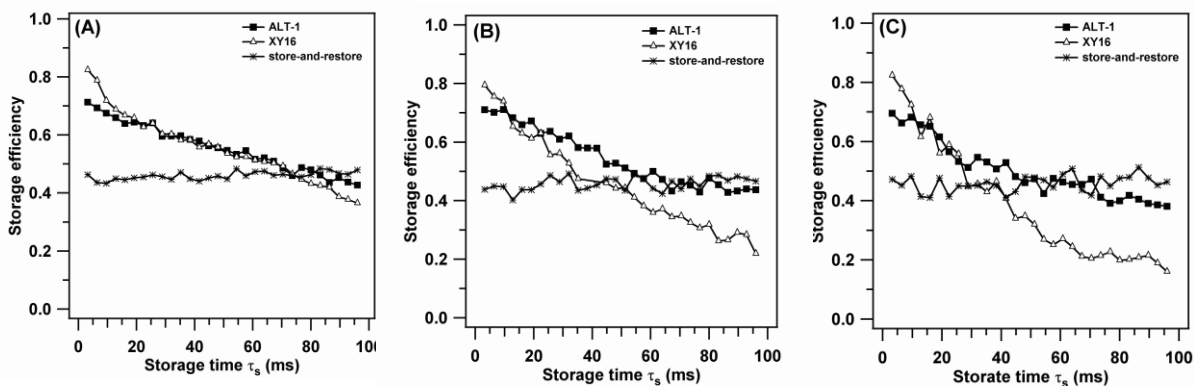


Figure AI.6. Comparison among various magnetization storage sequences of the storage efficiency (as measured in terms of spectral area) of the ^{13}C spectrum of methanol absorbed in a rose stem, as a function of storage time τ_s . The sample was rotated in MAS at (A) 0 Hz, (B) 50 Hz, and (C) 100 Hz. The cycle time τ_{cycle} is 100 μs . The storage efficiency is relative to the corresponding spectral area for $\tau_s = 0$.

The storage efficiency of the store-and-restore sequence is not affected by sample rotation at 100 Hz (Figure AI.6C), while the XY16 sequence is affected to some degree. In the store-and-restore sequence, only the component stored along the z-axis is preserved (the component left in the transverse plane is dephased and destroyed during the storage period). The storage efficiency of the store-and-restore sequence is affected by neither molecular motions nor sample rotation. The mobility (from one magnetic micro-environment to another) of methanol molecules adsorbed in the stem is apparently sufficiently large to degrade the effectiveness of echo-generating pulses. From this viewpoint, one would not expect much difference between the effectiveness of the ALT-1 sequence and that of the XY16 sequence, even though the latter sequence uses more echo-generating pulses, because the effectiveness of molecular reorientation is far more significant than that of sample rotation. The XY16 sequence, however, is affected more than the ALT-1 sequence by sample rotation (Figure AI.5), because the initial

magnetization is located entirely in the transverse plane throughout the storage period in XY16, while in the ALT-1 sequence the initial magnetization is located in the transverse plane for only half of the storage period. Reducing the duration in which the initial magnetization is located in the transverse plane diminishes the effect of sample rotation.

Conclusions

During any non-pulse segment of the storage period in the ALT-1 sequence, essentially half of the initially transverse magnetization is stored along the z axis and the other half is preserved by an echo-generating pulse, and those two components are alternated by a $\pi/2$ pulse during the cycle. As a result of the alternations, both transverse components of the initial transverse magnetization are treated ‘the same’ during the storage period in the ALT-1 sequence and orientational (phase) information of the initial transverse magnetization is kept over the storage period. For samples with long T_2 , the ALT-1 sequence and published sequences of the Carr-Purcell type are advantageous relative to the store-and-restore method, because the store-and-restore approach automatically throws away half of the initial transverse magnetization. The ALT-1 sequence preserves magnetization more effectively than a published class of modified Carr-Purcell type sequences, because essentially half of the magnetization during storage periods is not subjected to relaxation from T_2 effects. This is an especially important advantage for the ALT-1 sequence over the modified Carr-Purcell type sequences for a sample having short T_2 .

The storage efficiency of the ALT-1 sequence is lowered by sample rotation, which causes chemical shifts to vary over an echo period. In addition, a rotary resonance

recoupling can occur under MAS and this can significantly attenuate magnetization storage efficiency. In order to avoid effects of strong dipole-dipole interactions, ^1H decoupling is required during the storage period. For cases in which the ALT-1 sequence is used with ^1H decoupling, cross polarization between ^1H and ^{13}C should be avoided during the storage period, e.g., by using schemes such as mis-matched ^1H decoupling during the ^{13}C pulses or no ^1H decoupling pulse during the ^{13}C rf pulses.

Acknowledgements

The authors gratefully acknowledge support from NSF Grant CHE-0413611.

References:

- (1) Bax, A.; Szeverenyi, N. M.; Maciel, G. E. *J. Magn. Reson.* **1983**, *52*, 147.
- (2) Keeler, C.; Xiong, J. C.; Lock, H.; Dec, S.; Tao, T.; Maciel, G. E. *Cat. Today* **1999**, *49*, 377.
- (3) Szeverenyi, N. M.; Bax, A.; Maciel, G. E. *J. Magn. Reson.* **1985**, *61*, 440.
- (4) Bax, A.; Szeverenyi, N. M.; Maciel, G. E. *J. Magn. Reson.* **1983**, *55*, 494.
- (5) Maciel, G. E.; Szeverenyi, N. M.; Sardashti, M. *J. Magn. Reson.* **1985**, *64*, 365.
- (6) Sardashti, M.; Maciel, G. E. *J. Magn. Reson.* **1987**, *72*, 467.
- (7) Iwamiya, J. H.; Davis, M. F.; Maciel, G. E. *J. Magn. Reson.* **1990**, *88*, 199.
- (8) Carter, C. M.; Alderman, D. W.; Grant, D. M. *J. Magn. Reson.* **1985**, *65*, 183.
- (9) Ishii, Y.; Tycko, R. *J. Magn. Reson.* **2000**, *142*, 199.
- (10) Wiench, J. W.; Bronnimann, C. E.; Lin, V. S. Y.; Pruski, M. *J. Am. Chem. Soc.* **2007**, *129*, 12076.
- (11) Granwehr, J.; Harel, E.; Han, S.; Garcia, S.; Pines, A.; Sen, P. N.; Song, Y. Q. *Phys. Rev. Lett.* **2005**, *95*, 075503.
- (12) Moule, A. J.; Spence, M. M.; Han, S. I.; Seeley, J. A.; Pierce, K. L.; Saxena, S.; Pines, A. *Proc. Natl. Acad. Sci. U.S.A.* **2003**, *100*, 9122.
- (13) Meiboom, S.; Gill, D. *Rev. Sci. Instr.* **1958**, *29*, 688.
- (14) Maudsley, A. A. *J. Magn. Reson.* **1986**, *69*, 488.
- (15) Gullion, T.; Baker, D. B.; Conradi, M. S. *J. Magn. Reson.* **1990**, *89*, 479.
- (16) Gullion, T.; Schaefer, J. *J. Magn. Reson.* **1989**, *81*, 196.
- (17) Tang, J.; Sterna, L.; Pines, A. *J. Magn. Reson.* **1980**, *41*, 389.
- (18) Hoatson, G. L.; Vold, R. L.; Tse, T. Y. *J. Chem. Phys.* **1994**, *100*, 4756.
- (19) Gutowsky, H. S.; Pake, G. E. *J. Chem. Phys.* **1950**, *18*, 162.
- (20) Hu, J. Z.; Alderman, D. W.; Pugmire, R. J.; Grant, D. M. *J. Magn. Reson.* **1997**, *126*, 120.
- (21) Oas, T. G.; Griffin, R. G.; Levitt, M. H. *J. Chem. Phys.* **1988**, *89*, 692.
- (22) Ernst, M.; Samoson, A.; Meier, B. H. *Chem. Phys. Lett.* **2001**, *348*, 293.

APPENDIX II

Molecular-Level Consequences of Biomass Pretreatment by Dilute Sulfuric Acid at Various Temperatures

The contents of this chapter are a reformatted paper titled *Molecular-Level Consequences of Biomass Pretreatment by Dilute Sulfuric Acid at Various Temperatures*

published in *Energy & Fuels*, Volume 25, Issue 4, Pages 1790-1797.

Molecular-Level Consequences of Biomass Pretreatment by Dilute Sulfuric Acid at Various Temperatures

Takeshi Kobayashi,^a Benjamin Kohn,^a Lesley Holmes,^a Rebecca Faulkner,^a Mark Davis,^b and Gary E. Maciel^{a}*

^a Department of Chemistry, Colorado State University, Ft. Collins, CO 80523.

^b and National Renewable Energy Laboratory, Golden, CO 80401-3393.

E-mail: gary.maciel@colostate.edu

*Corresponding Author

^aDepartment of Chemistry, Colorado State University

Phone: (970)-491-6480

E-mail: gary.maciel@colostate.edu

Overview.

Ex situ room temperature ¹³C NMR measurements are reported on powdered poplar wood that has been pretreated with dilute sulfuric acid (concentrations up to 1 wt%) for times ranging up to 20 min and at temperatures of 120, 130, 140 and 150 °C. There are significant, albeit not dramatic, changes in the measured NMR *spectra* of the biomass as result of dilute sulfuric acid treatment. Values of T₁ for ¹³C and for ¹H, as well as T_{CH} and T_{1pH}, were measured for lignin peaks and for cellulose peaks in the ¹³C NMR spectra, as potential indicators of the degree of atomic-level motion. For lignin components, one finds a trend to larger T_{CH} values as treatment time or H₂SO₄ concentration is increased for treatment temperatures of 120 °C and 130 °C; however, for treatment temperatures of 140 °C and 150 °C, T_{CH} apparently decreases as treatment time is increased. This higher-temperature T_{CH} behavior implies that the lignin may actually become more rigid at later stages of treatment at temperatures ≥ 140 °C, which can be explained by cleavages of ether linkages of lignin and subsequent formation of new linkages, i.e., lignin recondensation. T_{1C} and T_{1H} measurements are consistent with this interpretation. The relationships between atomic-level mobility of lignin in biomass and

treatment temperature is consistent with published relationships between sugar yield and treatment temperature. The key role of acid treatment as a pretreatment for enzymatic digestion is evident in NMR measurements, especially relaxation measurements, even *after* the treatment.

KEYWORDS: biomass, lignocellulose, solid state NMR.

Introduction

In the production of cellulosic ethanol or potentially other organic products from biomass,¹⁰¹⁻¹⁰⁷ one of the key steps in the overall conversion procedure is the *pretreatment* step,¹⁰⁸⁻¹¹⁵ in which the cellulose contained in the biomass (lignocellulose) is rendered accessible to agents aimed at polysaccharide conversion, e.g., hydrolysis followed by fermentation. For the conversion of cellulosic biomass, one pretreatment approach that is receiving substantial attention is treatment with dilute sulfuric acid at elevated temperatures.¹¹⁶⁻¹³¹

For any pretreatment procedure, it is highly pertinent and presumably useful to elucidate the chemical-physical state of the biomass, especially chemical structure and local mobility, and hence entanglement, of the major chemical components of the biomass during, or at least at the end of, the pretreatment process. The three main types of constituents in wood are cellulose, lignin and hemicellulose. Figure AII.1 shows the monomer structure of cellulose (Figure AII.1a) and the main repeating, syringyl (Figure AII.1b) and guaiacyl (Figure AII.1c), units of lignin, as well as the structure of a hypothetical β -O-4 ether linkage between a guaiacyl unit and a syringyl unit in lignin

(Figure AII.1d). The structure of hemicellulose is more complex than that of cellulose, involving a variety of monosaccharide units, as well as other moieties such as uronic acids.

The alkyl aryl ether C_β-O-C₄ (β-O-4) linkage is the dominant connection between lignin monomers in woody biomass such as poplar.¹³² Upon treatment with dilute sulfuric acid, in addition to the dominant hydrolysis/depolymerization/disentanglement of hemicellulose, one might expect that a part of these ether linkages are cleaved, and under severe enough treatment conditions the cleaved linkages form other linkages, i.e., lignin recondensation.^{133,134} It is reported that more ether linkages are cleaved by acid treatment with increased temperature, but that above ~130 °C, this treatment also results in lignin recondensation, such that a maximum in the loosening of the biomass occurs between 120 and 130 °C.^{135,136}

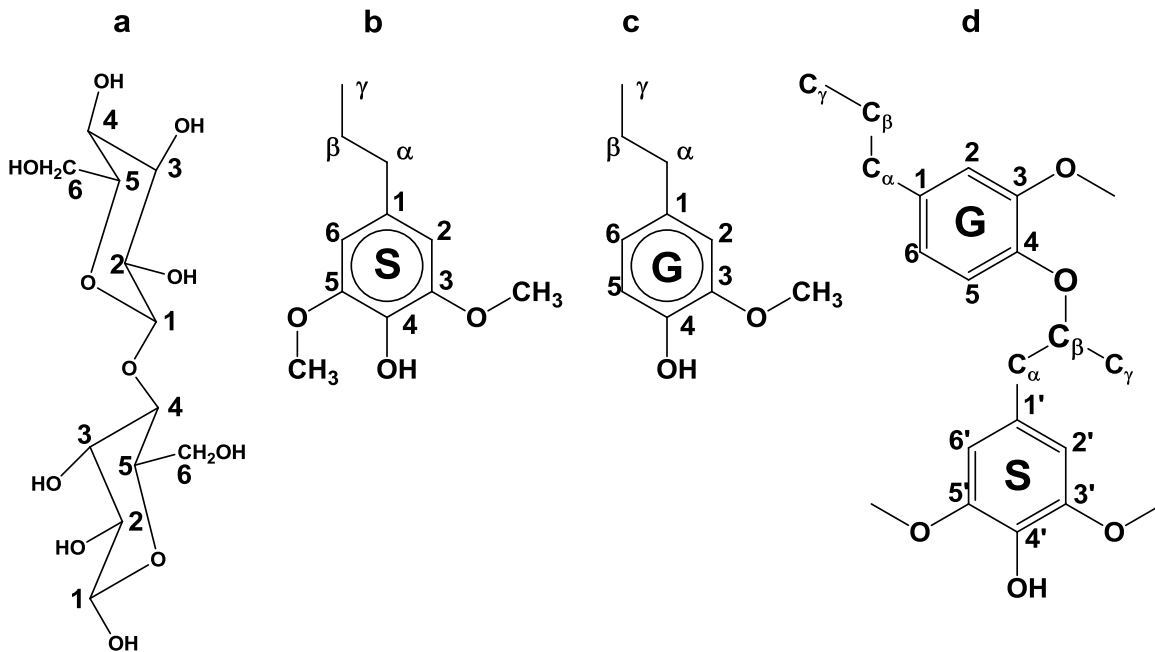


Figure AII.1. Structure of dominant chemical units in wood. a) cellulose, b) the syringyl unit of lignin (S), c) the guaiacyl unit of lignin (G) and d) a typical C_β-O-C₄ (β-O-4) linkage of lignin. R denotes repeating glucopyranose unit.

The phenylpropane unit in lignin is involved in linkages other than the C_β-O-4 and C_α-O-4 ether bonds. These include C-C or C-O-C linkages leading to the formation of, among others, β-5', β-6', 5-5', 4-O-5' condensed structures, which are more resistant to cleavage than, for example, C_β-O-4 moieties.¹³² In syringyl and guaiacyl units that are linked through the C_β-O-4 structure, mobility about C₁ and C₄ is restricted. However, if those units do not have linkages other than the β-O-4 bond, the aromatic ring can wobble or rotate about the C₁-C₄ axis, and C₃ and C₅ are more mobile than C₁ and C₄. Ether linkages between C₃ and C₅ of these units are cleaved by acid treatment, while the C₁-C_α bond is not. It therefore might be expected that mobility of C₃ and C₅ will be

enhanced by this treatment, but that those of C1 and C4 will not be altered. In contrast, previous work indicated that, when the sample was treated at 140 °C or above, cleaved ether linkages form other linkages, such as β -5', β -6', 5-5', 4-O-5'.¹³³⁻¹³⁶ Formation of these linkages would be expected to restrict motions of the aromatic ring of syringyl and guaiacyl units about the C1-C4 axis, and as a result mobility of C3 and C5 of the units will again be expected to be suppressed.

One of the few experimental approaches available for examining molecular-level structures and mobilities in solid or semi-solid materials is based on high-resolution solid-state NMR techniques,¹³⁷⁻¹⁴² including, in favorable cases, NMR relaxation parameters via their correlations of with motion.¹³⁸ For example, the spin-lattice relaxation time (T_1) is related to motions with characteristic times on the order of 10^{-8} s to 10^{-7} s; spin-lattice relaxation times in the rotating frame ($T_{1\rho}$) are sensitive to motions with characteristic times on the order of 10^{-5} s to 10^{-4} s; and cross-polarization (CP) time constants (T_{CH}) depend upon static or near-static magnetic dipole-dipole interactions.¹⁴³ Chemical shifts are exquisitely sensitive to details of molecular structure.¹⁴⁴

As part of a longer-term study aimed at using NMR measurements to determine molecular-level structures and mobilities *in situ* during a pretreatment process, in the present study we have employed *ex situ* NMR measurements, based on ^{13}C detection (in order to discriminate readily among different types of chemical structures), to study the molecular-level structures and mobilities of lignin and cellulose *at the end of the pretreatment process* for poplar wood treated with dilute sulfuric acid at temperatures from 120 °C to 150 °C for periods up to 20 min.

Experimental

Samples. Approximately 25 mg of poplar (*Populus trichocarpa*) was placed in a glass tube with about 0.2 mL of sulfuric acid (0.5 wt% H₂SO₄ unless otherwise noted below), then sealed with a 3-O-ring pressure-tight cap. The sample was heated at temperatures of 120, 130, 140 or 150 °C for periods ranging from 3 min to 20 min (not including 1 min heating-up period). Each sample was then quickly quenched to room temperature, washed with approximately 1 L of water over a two hour period, separated roughly from liquid by decantation and loaded, as a moist solid, into a 9 mm (ID) rotor for magic-angle spinning (MAS) ¹³C NMR measurements.

NMR Measurements. ¹³C NMR experiments were carried out at 25.1 and 50.2 MHz on natural-abundance (1.1 % ¹³C) samples, using Chemagnetics CP-MAS probes, for 9-mm MAS rotors, and modified Chemagnetics CMX II type spectrometers (now Varian-Agilent, Ft. Collins, CO). The MAS speed was typically 3 KHz, satisfactory for largely suppressing chemical-shift-anisotropy (CSA) sidebands with these spectrometers.¹³⁹ ¹³C spectra were processed by complex Fourier transformation of the sampled complex data and subsequent apodization with 25 or 50 Hz Lorentzian line broadening for the 25.1 MHz and 50.2 MHz measurements, respectively. The ¹H and ¹³C rf field strengths were each about 50 kHz. ¹³C chemical shifts are reported relative to liquid tetramethylsilane (TMS) at 0.0 ppm, using hexamethylbenzene as a secondary chemical shift reference.

¹H spin-lattice relaxation time (T_{1H}) measurements were made by ¹³C-detected saturation-recovery.^{145,146} ¹³C spin-lattice relaxation time (T_{1C}) measurements were made by a common CP version of the inversion recovery method.¹⁴⁷ The measurement of

rotating-frame spin-lattice relaxation times for protons ($T_{1\rho\text{H}}$) and cross-polarization time constants (T_{CH}) were made via ^{13}C detection by the well-known variable-contact-time method.^{138,145}

Results and Discussion

Peak Assignments.

Table AII.1 summarizes many of the ^{13}C chemical shift assignments that are most relevant to this study. These assignments were taken as ‘rough consensus’ values from the rather extensive literature on ^{13}C NMR of wood or wood-related samples.¹⁴⁸⁻¹⁶⁰ The numbers given in the table should be considered to have uncertainties of roughly ± 2 ppm, because of a number of factors, including variations in non-nearest-neighbor structures (e.g., alkyl substitution on aromatic rings of lignin), bulk magnetic susceptibility effects and varying chemical shift referencing methods among different laboratories.

Table AII.1. Selected^a ¹³C Chemical Shift Assignments.¹

$\delta^{13}\text{C}$ (ppm) ^c	Assignment
168-174	carbonyl or carboxyl of lignin or hemicellulose.
153	ether-linked S3, S5, G3. ^d
149	S4, G4-etherified.
146	non-ether-linked S3, S5, G3.
143	G4 with C4OH
133-138	S1.
128-132	G1.
121	G6.
115	G5.
111	G2.
109	C1 of arabinofuranosyl units.
102-106	S2, S6.
105	C1 of cellulose.
102	C1 of hemicellulose, e.g., xylan.
89	C4 of crystalline cellulose; C _α -OH of S unit.
84	C4 of amorphous cellulose; C3, C4, C5 of hemicellulose; C _β in certain chain-functionalized S units.
82	C4 of xylan.
75	C2, C3, C5 of hemicellulose and amorphous cellulose; C _α in certain chain-functionalized S units.
73	C2, C3, C5 of crystalline cellulose; C _α in certain chain-functionalized S units; C2, C3 in xylose.
66	C6 of crystalline cellulose; C _γ in certain chain-functionalized S units.
62	C6 in amorphous cellulose and hemicellulose; C5 in xylan; C _β or C _γ in certain chain functionalized S units.
56	methoxy groups of lignin, C _β in certain chain-functionalized S units.
22	acetate methyls in hemicellulose.

^a The most relevant and reliable assignments relevant, especially for intense peaks, for the issues addressed in this particular study.

^b Numbers taken as a 'consensus' from references 48 - 60.

^c Values relative to TMS.

^d Notation: S5 denotes C5 of a syringyl unit; G3 stands for C3 of a guaiacyl unit.

Figure AII.2 shows the ^{13}C CP-MAS NMR spectrum of water-saturated poplar sawdust. The weak peak at about 174 ppm represents carbonyls of lignin and of the acetate and carboxyl groups of hemicellulose. The broad peaks at 133 and 153 ppm are aromatic signals of lignin. The weak peak at 22 ppm corresponds to acetate methyls in hemicellulose. The sharp peak at 56 ppm arises from methoxyl groups of lignin and possibly of hemicellulose.^{61,62} Polysaccharides have peaks between 60 and 110 ppm, while side-chain groups of lignin provide a minor contribution to this region. The peak at 105 ppm corresponds to C1 of cellulose, with superimposed signal from C1 of hemicellulose. The peaks at 89 and 84 ppm are C4 signals from polysaccharides, mainly cellulose. The peak at about 89 ppm comes from highly ordered polysaccharides, e.g., cellulose, and the 84 ppm peak from polysaccharides that are amorphous, e.g., hemicellulose and fibre-surface cellulose; the same type of crystalline-vs-amorphous interpretation holds for the polysaccharide C6 peaks at 66 and 63 ppm as well as the C2, C3, and C5 peaks at about 73 and 75 ppm. The surfaces of cellulose-rich fibers contribute to the amorphous signal intensity.

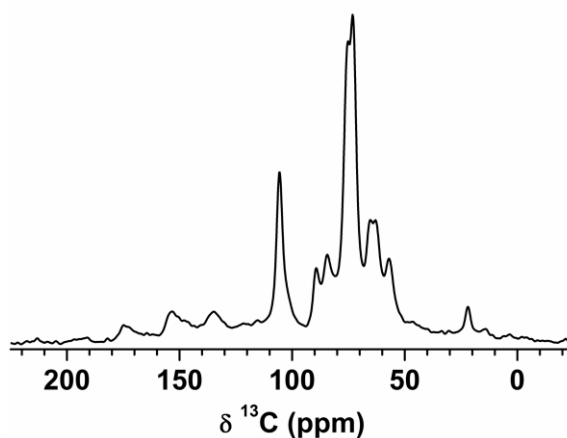


Figure AII.2. ^{13}C CP-MAS NMR spectrum of water-saturated poplar sawdust, obtained with contact time = 1 ms.

Effects of Sulfuric Acid Treatment on ^{13}C NMR Spectrum. Since cross polarization relies upon a static component of ^1H - ^{13}C dipolar interactions, the ‘mobilization’ of any portion or segment of biomass due to a treatment will reduce the observed ^{13}C CP-MAS intensity of that portion of the biomass. Hence, an observed reduction of ^{13}C CP-MAS intensity resulting from a treatment can be due to some combination of i) a conversion of one structure into other structure(s) and ii) the mobilization of certain structural component(s).

Figure AII.3 shows room temperature ^{13}C CP-MAS NMR spectra of poplar sawdust treated with 0.5 wt% H_2SO_4 at various temperatures for 5 minutes. As in all of the figures shown below that depict the effects of various extents of dilute H_2SO_4 treatments, one can see in Figure AII.3 an intensity decrease in the methoxyl peak at 56 ppm as the extent of treatment progresses. Detailed evaluation of the spectra reveals that the intensities of the peaks at 22 ppm and 174 ppm are substantially reduced by treatment at 120 °C and above. Signal intensities of the peaks at 75 ppm, 84 ppm and 63 ppm decrease with increasing treatment temperature. The decreases in signal intensities are primarily a result of the hydrolysis/mobilization and partial solubilization of hemicellulose and, to a lesser extent, amorphous cellulose. Unlike hemicelluloses, whose backbones are comprised of polymers which have short branches with 1,4- and 1,3-glycosidic linkages that are easily hydrolysable, cellulose (especially its crystalline portion) is far less susceptible to hydrolysis under the reaction conditions studied.¹⁰⁹

Hydrolysis of cellulose, especially its crystalline portion, is therefore expected to be minor and decreases observed in the signal intensities of the peaks corresponding in

part to crystalline cellulose (66, 73 and 89 ppm) are in fact smaller than those observed for hemicellulose (and amorphous cellulose). The signal intensity of the 105 ppm C1 saccharide peak also decreases as result of the treatment, primarily due to hydrolysis of glycosidic linkages in hemicellulose. Signal intensities of the aromatic lignin peaks at 133 and 153 ppm also decrease slightly after the acid treatment. The decrease in the lignin signal intensity is smaller than that observed for the other signals, as lignin is more recalcitrant to hydrolysis by dilute acid than are hemicellulose (and, to some degree, amorphous cellulose). Using integrated ^{13}C NMR intensities, as described previously in detail by Davis and co-workers,⁵⁵⁻⁵⁷ the lignin and cellulose(cryst) contents of the unheated poplar sample (Fig. AII.3 bottom) and the sample heated at 150 °C (Fig. AII.3 top), both containing 0.5 % H_2SO_4 , were determined to be 14% and 12 %, respectively, for the lignin and 34% and 21 %, respectively for the cellulose(cryst).

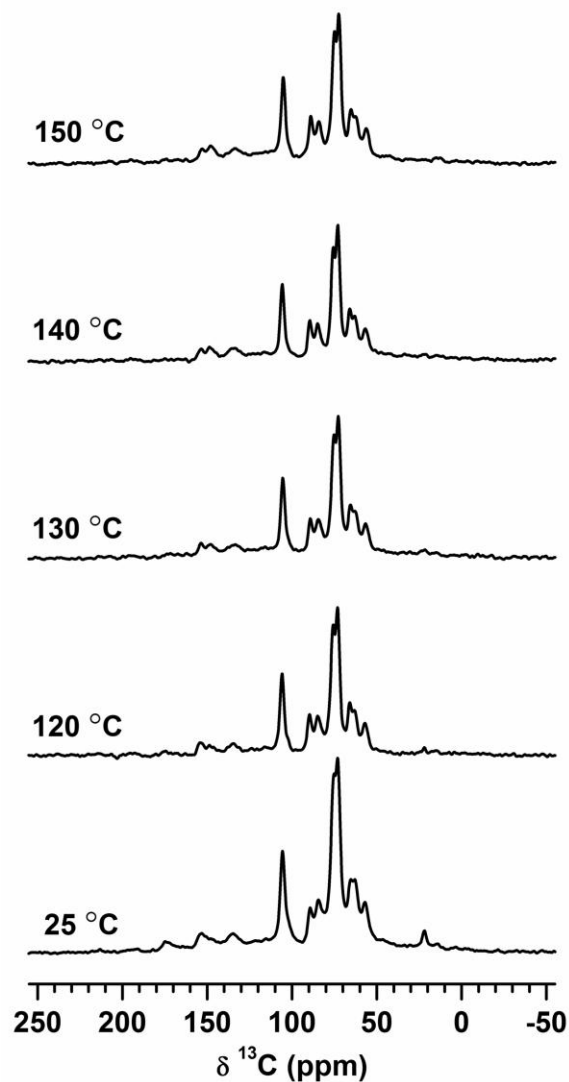


Figure AII.3. ^{13}C CP-MAS spectra of poplar sawdust with various treatment temperatures in 0.5 wt% H_2SO_4 for 5 min, obtained with contact time = 1 ms. Spectra are shown without amplitude scaling.

Figure AII.4 shows ^{13}C CP-MAS NMR spectra of poplar sawdust treated at 120 °C with 0.5 wt% H_2SO_4 , as a function of treatment time. The acetoxy ($\text{CH}_3\text{C}(\text{O})\text{-O-}$) peaks at 22 ppm and 174 ppm almost disappear after 3 minutes of treatment, while signal intensities of the amorphous saccharide peaks at 75 ppm, 84 ppm and 63 ppm decrease

only slightly with increasing treatment time. ^{13}C NMR area analysis⁵⁵⁻⁵⁷ for the unheated and 120 °C heated samples, both containing 0.5% H_2SO_4 , yielded 14% and 8%, respectively for the lignin and 34% and 27%, respectively, for the cellulose(cryst).

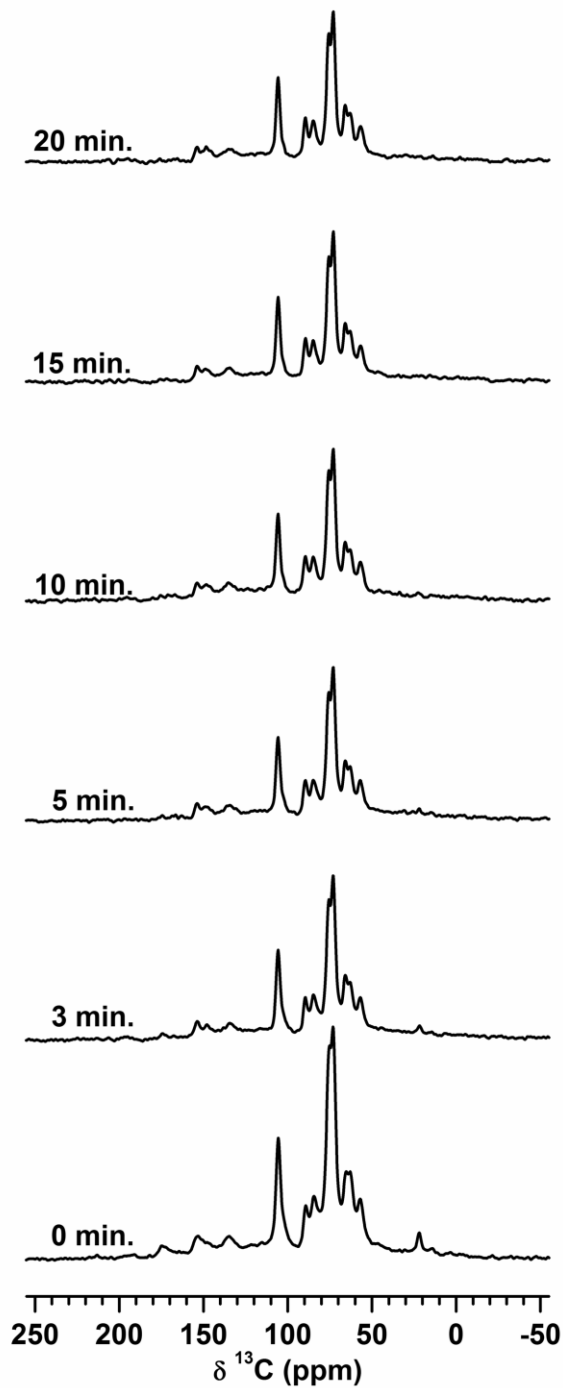


Figure AII.4. ^{13}C CP-MAS spectra of poplar sawdust treated at 120 °C with 0.5 wt% H_2SO_4 , as a function of treatment time, obtained with contact time = 1 ms. Spectra are shown without amplitude scaling.

Figure AII.5 shows ^{13}C CP-MAS NMR spectra of poplar sawdust treated with various H_2SO_4 concentrations at $120\text{ }^\circ\text{C}$ for 15 minutes. Hemicellulose (and amorphous cellulose?) is shown to be hydrolyzed and partially solubilized even by 0.1 wt% H_2SO_4 , as evidenced by a decrease in signal intensity of the peaks at 84, 75 and 63 ppm. No significant differences in the extent of hydrolysis of hemicellulose are observed between 0.5 and 1.0 wt% H_2SO_4 . These patterns are consistent with the literature on dilute acid pretreatment of biomass.¹⁶⁻³¹ ^{13}C NMR area analysis⁵⁵⁻⁵⁷ for the untreated poplar sample (Fig. AII.5 bottom) and the sample heated in 1.0% H_2SO_4 at $120\text{ }^\circ\text{C}$ (Fig.5 top) yielded 14% and 11%, respectively for the lignin and 34% and 24%, respectively, for the cellulose(cryst).

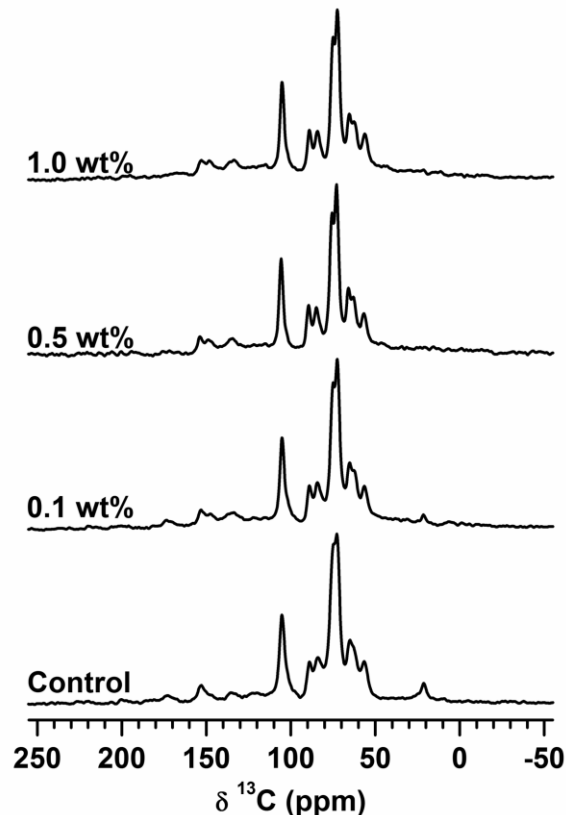


Figure AII.5. ^{13}C CP-MAS spectra (50 MHz) of poplar sawdust treated at 120 °C for 15 min with various H_2SO_4 concentrations, obtained with contact time = 1 ms. Spectra are shown without amplitude scaling.

Figure AII.6 shows the 140-165 ppm region of the ^{13}C NMR spectra of poplar sawdust samples treated with 0.5 wt% H_2SO_4 under various pretreatment conditions (i.e., temperature and treatment time). The peak at 153 ppm is primarily due to C3 and C5 of ether-linked syringyl units (S3 and S5) and ether-linked C3 of guaiacyl (G3) units, the 149 ppm peak is due mainly to ether-linked S4 and G4 units, and the peak at 147 ppm is assigned to non-ether-linked S3, S5 and G3 units. A resonance resulting from non-ether-linked syringyl and/or guaiacyl units at 147 ppm is observed as a shoulder in the control sample (untreated sawdust); the intensity of this signal increases with severity of

treatment. More ether linkages at the C5 carbon of the lignin moieties are cleaved as treatment severity increases, as is evidenced by decreasing signal intensity of the 153 ppm peak relative to that of the C3 peak at 147 ppm.

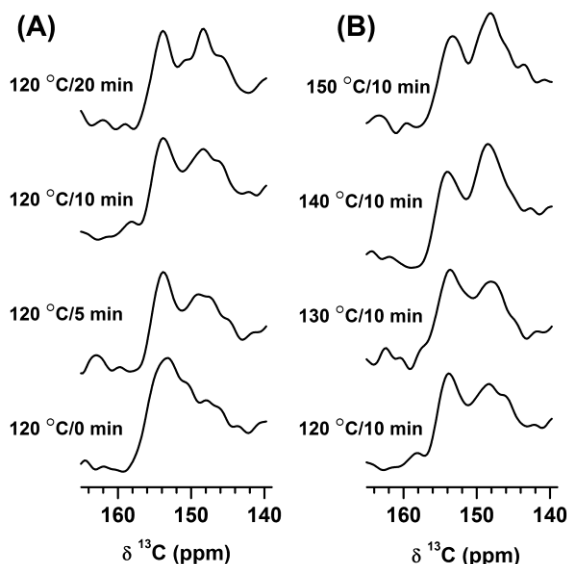


Figure AII.6. Lignin region of the ^{13}C CP-MAS NMR spectra of poplar sawdust samples treated with 0.5 wt% H_2SO_4 , as a function of (A) treatment time and (B) temperature, obtained with contact time = 1 ms.

One sees in Figures AII.3 – AII.6 that most of the obvious differences among the collections of raw spectra in each of these figures is seen between the bottom spectrum (smallest value of the parameter that is varied in the pretreatment) and all the spectra above the bottom spectrum. This implies that most of the changes that occur in the more rigid components of the sample, i.e., those components with the highest CP efficiency, occur between the control sample (no heating or no acid) and the sample for which the pretreatment parameter (temperature, heating time, H_2SO_4 concentration) has its smallest non-zero value. It can be noted that much larger changes are seen throughout the various stages of pretreatment in DP-MAS ^{13}C spectra (DP = direct polarization -- no CP –

relying on ^{13}C spin-lattice relaxation directly and hence favoring more liquid-like highly-mobile components). DP experiments are included in later studies,⁶³ yet to be published, which require the use of ^{13}C -enriched wood samples, which were not available at the time the studies reported here were conducted. Extensive DP-MAS strategies on natural-abundance samples would be time-prohibitive.

Effects of Sulfuric Acid Treatment on Molecular Dynamics. Because of imitations in signal-to-noise, uncertainties in derived relaxation values (as indicated in the ‘error bars’ in the plots below) are rather large, especially for lignin aromatic peaks. Nevertheless, even with these uncertainties, qualitative trends can be discerned.

All the $T_{1\text{C}}$ and $T_{1\text{H}}$ values that are summarized in the plots presented below were measured on the 100 MHz spectrometer. In addition, T_1 values were measured on both 100 MHz and 200 MHz spectrometers for a H_2O -saturated poplar sample.

$T_{1\text{C}}$ values were derived by curve fitting analyses of proton-enhanced ^{13}C experiments, as described by Torchia,¹⁴⁷ while $T_{1\text{H}}$ values were derived by curve fitting analyses of ^{13}C -detected saturation-recovery experiments. Although, of course, most of the experimental T_1 data would be better fit by two exponentials than by one exponential, values based on a single-exponential analysis are given in the results that follow. T_{CH} and $T_{1\rho\text{H}}$ values were calculated by curve fitting analyses of variable-contact-time experiments¹⁴⁶ on the 200 MHz spectrometer.

Figure AII.7 shows the variation in $T_{1\text{C}}$ values in various holocellulose (cellulose and hemicellulose) spectral regions (65 – 110 ppm plus lignin methoxy at 56 ppm) and the lignin region (130 – 160 ppm) of poplar sawdust as a function of the temperature of

treatment for 20 min. T_{1C} values for both chemical shift regions show a steady increase with increasing treatment temperature.

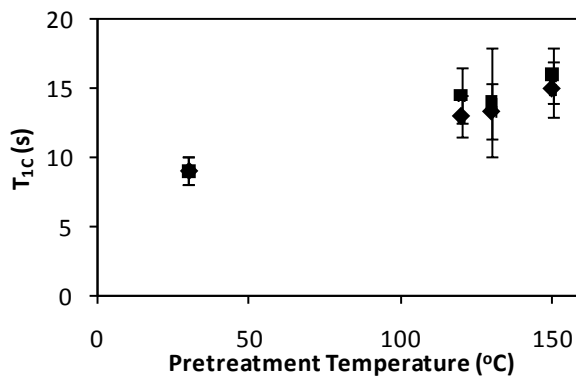


Figure AII.7. T_{1C} of holocellulose (65 – 110 ppm), ◆, and lignin (130 – 160 ppm), ■, regions of the ^{13}C CP-MAS spectra of poplar sawdust, as a function of pretreatment temperature. (0.5 wt% sulfuric acid, 20 min). Number of acquisitions = 1000, pulse delay = 1.5 s, MAS rate = 3.0 kHz.

T_{1C} values for both the carbohydrate and lignin regions of the ^{13}C spectrum, measured at both 25.1 MHz and 50.2 MHz, are each roughly twice as large at the higher magnetic field; the same is true of T_{1H} .⁶¹ This pattern indicates that the relevant atomic-level motions in these systems occur with correlation times, τ_C , that are less than $(50 \times 10^6)^{-1} = 2 \times 10^{-8}$ s and that, for T_{1C} to increase, τ_C must decrease. The fact that T_{1C} of the temperature-quenched sample increases with increasing 0.5 wt% H_2SO_4 treatment temperature indicates that, as the 20-min treatment temperature is increased, τ_C of the temperature-quenched biomass decreases – higher atomic-level mobility – for both the lignin and carbohydrate components.

Figure AII.8 shows variation in T_{1C} values for holocellulose (plus lignin methoxy) and lignin regions of the poplar sawdust spectrum as a function of 150 °C treatment time. The T_{1C} values show significant increases with increasing treatment time, leveling off after about 7 min. The results suggest that the atomic-level mobility generated at 150 °C, and retained after temperature quenching to 30 °C, does not increase after about 7 min.

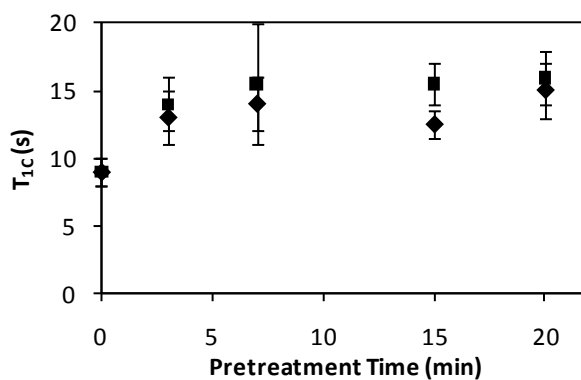


Figure AII.8. T_{1C} of holocellulose (65 – 110 ppm), \blacklozenge , and lignin (130 – 160 ppm), \blacksquare , regions of the ^{13}C CP-MAS spectra of poplar sawdust, as a function of pretreatment time. (0.5 wt% sulfuric acid, 150 °C). Number of acquisitions = 1000, pulse delay = 1.5 s, MAS rate = 3.0 kHz.

Figure AII.9 shows variation in T_{1H} values for various spectral regions of poplar sawdust as a function of treatment temperature. There is a rough trend of generally increasing T_{1H} with increasing treatment temperature, with an apparent maximum at about 130 °C. These results suggest that samples quenched to 30 °C after treatment for 20 min reach their maximum quench-retained atomic-level mobility in heating at 130 °C, and some of that mobility is not achieved or retained with 20-min treatment at 150 °C.

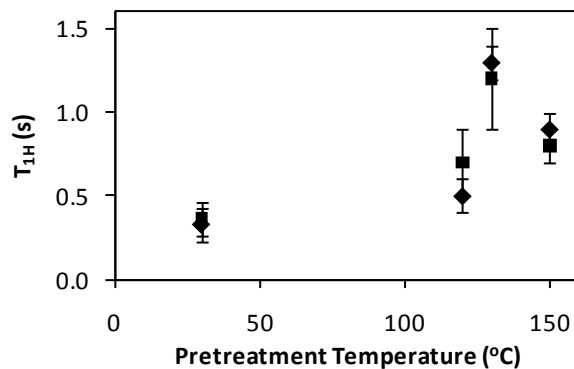


Figure AII.9. T_{1H} of holocellulose (65 – 110 ppm), ◆, and lignin (130 – 160 ppm), ■, regions of the ^{13}C CP/MAS spectra of poplar sawdust, as a function of pretreatment temperature. (0.5 wt% sulfuric acid, 20 min). Number of acquisitions = 1000, pulse delay = 1.5 s, MAS rate = 3.0 kHz.

Figure AII.10 shows variation in T_{1H} values for the main regions of the poplar sawdust spectrum as a function of treatment time at 150 °C. Aside from a maximum at about 3 min, there is a slight and gradual increase in T_{1H} with increasing treatment time. These results imply that, with a treatment temperature of 150 °C, the maximum quench-retained atomic-level mobility is achieved in about 3 min and decreases with longer treatment time.

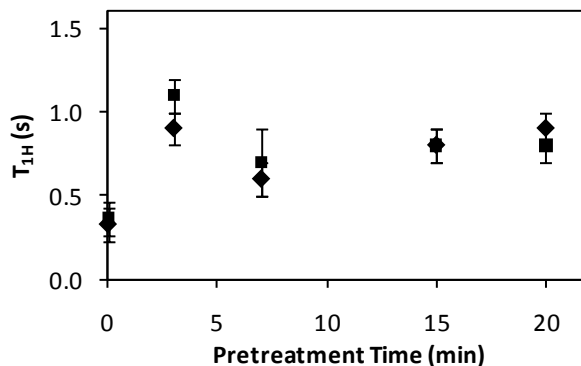


Figure AII.10. T_{1H} of holocellulose (65 – 110 ppm), \blacklozenge , and lignin (130 – 160 ppm), \blacksquare , regions of the ^{13}C CP/MAS spectra of poplar sawdust, as a function of treatment time (0.5 wt% sulfuric acid, 150 °C). Number of acquisitions = 1000, pulse delay = 1.5 s, MAS rate = 3.0 kHz.

T_{CH} and $T_{1\rho H}$ values were measured via the variable-contact-time technique.^{138,146} Only T_{CH} values are summarized and discussed below, because of the complexity of $T_{1\rho H}$ dependence on spectral densities and the difficulty of interpreting $T_{1\rho H}$ data;^{64,65} $T_{1\rho H}$ results are given in the Supporting Information.

Figure AII.11 shows variations of T_{CH} values in the 65-110 ppm region (carbohydrate region) under various 0.5 wt% sulfuric acid treatment conditions (temperature and treatment time) of poplar sawdust. While there are substantial variations of T_{CH} as time and temperature are varied, there are no obvious and dramatic trends. Furthermore, since dilute sulfuric acid treatment is believed to substantially solubilize hemicellulose, much of the observed variations in the CP dynamics may be due to compositional changes, rather than simple mobility changes. For most treatment temperatures, there appears to be a T_{CH} maximum at some intermediate treatment time.

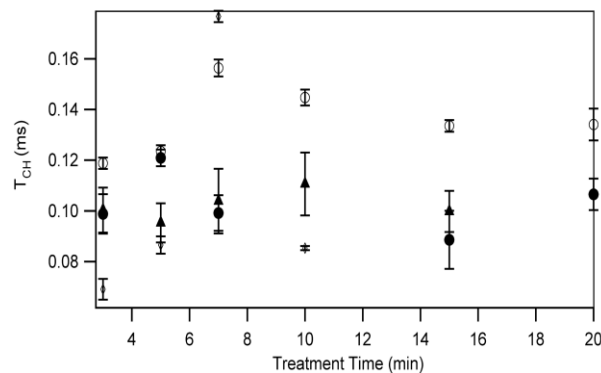


Figure AII.11. T_{CH} for the 65-110 ppm region of the ^{13}C CP/MAS spectra of poplar sawdust, as a function of treatment time. Samples were treated with 0.5 wt% sulfuric acid at 110 °C, ●; 120 °C, ○; 130 °C, ▲; and 140 °C, ◇. Number of acquisitions = 1000, pulse delay = 1.5 s, MAS rate = 3.0 kHz.

Figure AII.12 shows T_{CH} values for the 130-140 ppm region (assigned to S1 and G1) and 140-160 ppm region (assigned to S3, S5, G3, G4) in the ^{13}C NMR spectra of poplar sawdust samples treated with 0.5 wt% H_2SO_4 under various conditions (temperature and treatment time). The T_{CH} value for [S1 + G1] shows a slight increase with time for 120 °C and 130 °C treatments (implying slight increases in atomic-level mobility) and small decreases with time for 140 °C and 150 °C (implying small decreases in atomic-level mobility). The T_{CH} values of [S3 + S5 + G3 + G4] show qualitatively similar trends, although the increases with time are larger than for the [S1 + G1] case.

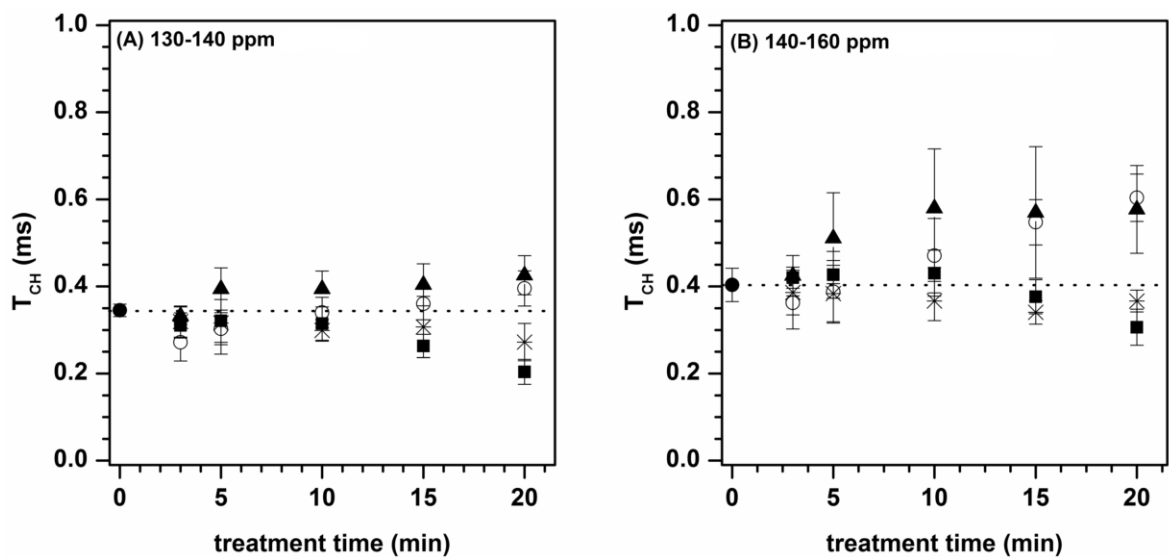


Figure AII.12. T_{CH} for (A) the 130-140 ppm region (S1 + G1) and (B) the 140-160 ppm region (S3 + S5 + G3 + G4) of the ^{13}C CP/MAS spectra of poplar sawdust, as a function of treatment time. Samples were treated with 0.5 wt% sulfuric acid at 30 °C, ●; 120 °C, ○; 130 °C, ■; 140 °C, ▲; and 150 °C, *.

These results can be well explained by cleavage of ether linkages connecting to syringyl and guaiacyl units and subsequent formation of new linkages (i.e., lignin recondensation) that occurs at higher treatment temperature. Figure AII.6 clearly confirms the cleavage of ether linkages between C3 and C5 of syringyl and guaiacyl units, whereas the cleavage of the C_{β} -O-4 linkage is not obvious. Assuming the $C1-C_{\alpha}$ bond is not cleaved, one can expect that mobility of C3 and C5 along $C1-C4$ axis will be enhanced by this treatment, but that those of C1 and C4 will not be altered. When a biomass sample is treated at 140 °C or above, it has been reported that the cleaved ether linkages form other linkages such as β -5', β -6', 5-5', 4-O-5', i.e., lignin recondensation.³³⁻³⁶ Formation of these new linkages would suppress the mobility of aromatic rings of syringyl and guaiacyl units. The ether-cleavage/ recondensation sequence is not obvious

in the ^{13}C CP/MAS NMR spectra ; however, this can be clearly revealed by the measurements of molecular-level dynamics.

Figure AII.13 shows variation in T_{CH} values for the lignin region (130 - 160 ppm) of samples treated at 120 °C for 15 min with various H_2SO_4 concentrations. Aside from the smaller T_{CH} values measured for zero H_2SO_4 concentration, T_{CH} does not seem to depend markedly upon H_2SO_4 concentration under this treatment condition, even though differences in the degree of hydrolysis/partial-solubilization are observed in the ^{13}C CP/MAS NMR spectra.

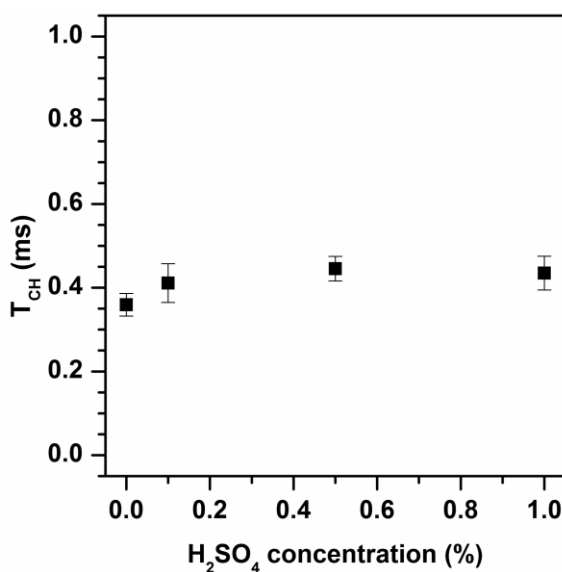


Figure AII.13. T_{CH} for the 130-160 ppm region of the ^{13}C CP/MAS spectra of poplar sawdust samples, as a function of H_2SO_4 concentration. Samples were treated at 120 °C for 15 min. Experiments were carried with contact time = 1 ms.

Summary and Conclusions

The *ex situ* results reported here provide strong indications, but no dramatic demonstrations, of substantial structural/dynamical changes in biomass structure as result of treatment with dilute sulfuric acid at various modest temperatures (≤ 150 °C), *as*

measured after the heating was over. Careful scrutiny of the ^{13}C CP/MAS spectra as functions of treatment time, temperature or acid concentration show that, *after treatment*, the composition of the biomass has undergone substantial, albeit not major, changes. This is manifested mainly in changes in peak intensities that indicate the hydrolysis/solubilization of methoxyl and $\text{CH}_3\text{C}(\text{O})\text{-O-}$ moieties specifically and, more globally, the hydrolysis/mobilization (partial solubilization) of hemicellulose and, to a lesser extent, amorphous cellulose, as well as lignin.

As the extent of treatment was increased (increasing treatment time or temperature), gradual increases of spin-lattice relaxation times, for both ^1H and ^{13}C , are seen for both holocellulose and lignin resonances; this implies that the atomic-level mobilities of these structural components are enhanced by the treatment, based on the fact that these mobilities are already on the fast-motion side of the T_1 minima. For lignin components, one finds a trend to larger T_{CH} values as treatment time or H_2SO_4 concentration is increased for treatment temperatures of 120 °C and 130 °C; however for treatment temperatures of 140 °C and 150 °C, T_{CH} seems to *decrease* as treatment time is increased. Since increased T_{CH} results from a lower polarization transfer rate, implying a greater atomic-level mobility, this higher temperature T_{CH} behavior implies that the lignin may actually become more rigid at later stages of treatment at temperatures ≥ 140 °C, as has been suggested previously.³³⁻³⁶

The yield of sugar by enzymatic digestion of cellulose depends on the accessibility of the enzyme to cellulose, but the yield has not been well correlated with the degree of hydrolysis and extraction of hemicellulose. The non-monotonic variation of the relaxation parameters observed in this study as functions of the extent or harshness of

dilute H₂SO₄ treatment can be explained by first a depolymerization (ether cleavages) and then a repolymerization (recondensation) of lignin. Viewed in these terms, the observed patterns and trends of mobility within the lignin structure of biomass that is treated with dilute sulfuric acid is consistent with the relationship between the sugar yield and the pretreatment temperature reported in previous studies.³⁶ Thus, we conclude that the key role of acid treatment as a pretreatment for enzymatic digestion can be seen through NMR relaxation measurements of motion of the lignin even *after the treatment*. Of course, it is possible that a substantially greater degree of mobilization of the lignin structure occurs *during* the pretreatment at elevated temperatures. More direct indications of the molecular-level state of biomass during pretreatment would be expected from *in situ measurements at the treatment temperature*. Such experiments, while presenting difficult technical challenges, are currently being pursued.

SUPPORTING INFORMATION

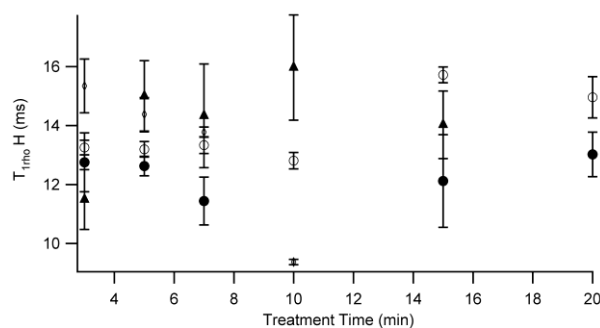


Figure AII.14. T_{1ρH} for the 65-110 ppm region of the ¹³C CP/MAS spectra of poplar sawdust, as a function of treatment time. Samples were treated with 0.5% sulfuric acid at 30 °C, ●; 120 °C, ○; 130 °C, ▲; and 140 °C, ■. Number of acquisitions = 1000, pulse delay = 1.5 s, MAS rate = 3.0

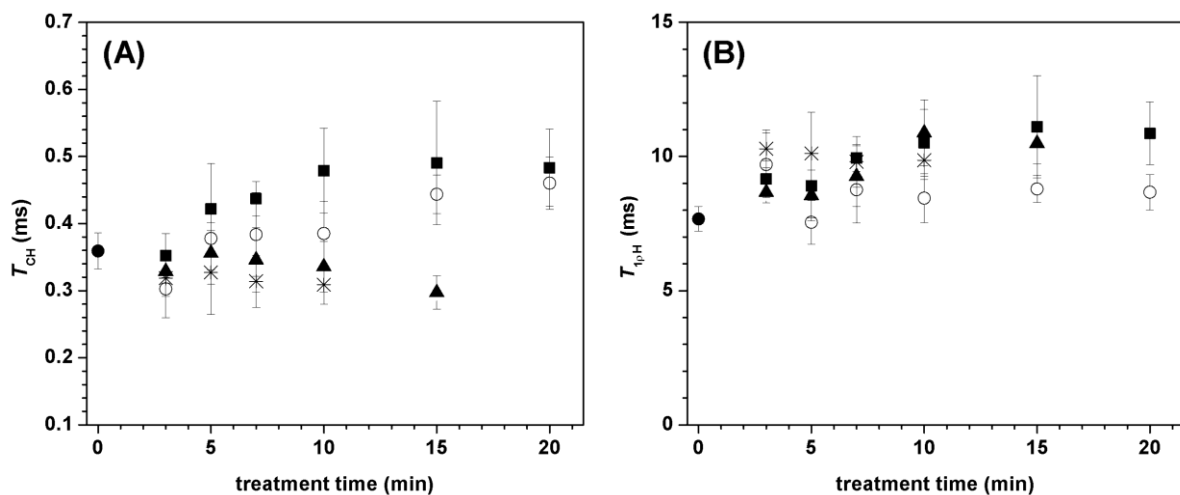


Figure AII.15. T_{CH} (A) and $T_{1\rho H}$ (B) for the 130-160 ppm region of the ^{13}C CP/MAS spectra of poplar sawdust, as a function of treatment time. Samples were treated with 0.5% sulfuric acid at 30 °C, ●; 120 °C, ○; 130 °C, ■; 140 °C, ▲; and 150 °C, *. Number of acquisitions = 1000, pulse delay = 1.5 s, MAS rate = 3.0 kHz.

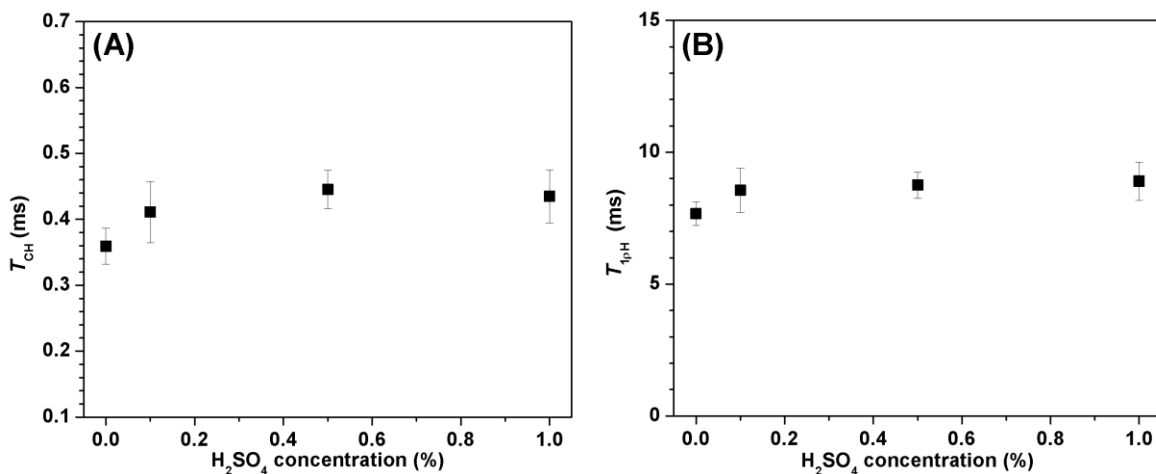


Figure AII.16. T_{CH} (A) and $T_{1\rho H}$ (B) for the 130-160 ppm region of the ^{13}C CP/MAS spectra of poplar sawdust samples, as a function of H_2SO_4 concentration. Samples were treated at 120 °C for 15 min. Number of acquisitions = 1000, pulse delay = 1.5 s, MAS rate = 3.0 kHz.

Acknowledgements

The authors gratefully acknowledge support of this research by the U.S. Department of Energy.

References:

- (1) Sannigrahi, P.; Ragauskas, A. J.; Tuskan, G. A. *Biofuels Bioprod. Bioref.* **2010**, *4*, 209.
- (2) Kintisch, E. *Science* **2007**, *315*, 786.
- (3) Tullo, A. H. *Chem. Eng. News* **2007**, *85*, 28.
- (4) McMillan, J. D. Biochemical Conversion of Cellulosic Feedstocks. In *Conference on Biomass to Chemicals and Fuels: Science, Technology and Public Policy* Huston, TX, 2006.
- (5) Sun, Y.; Cheng, J. Y. *Bioresour. Technol.* **2002**, *83*, 1.
- (6) Galbe, M.; Zacchi, G. *Appl. Microbiol. Biotechnol.* **2002**, *59*, 618.
- (7) Lynd, L. R.; Wyman, C. E.; Gerngross, T. U. *Biotechnol. Prog.* **1999**, *15*, 777.
- (8) Taherzadeh, M. J.; Karimi, K. *Int. J. Mol. Sci.* **2008**, *9*, 1621.
- (9) Kumar, P.; Barrett, D. M.; Delwiche, M. J.; Stroeve, P. *Ind. Eng. Chem. Res.* **2009**, *48*, 3713.
- (10) Taherzadeh, M. J.; Karimi, K. *Bioresources* **2007**, *2*, 707.
- (11) Taherzadeh, M. J.; Karimi, K. *Bioresources* **2007**, *2*, 472.
- (12) Mosier, N.; Wyman, C.; Dale, B.; Elander, R.; Lee, Y. Y.; Holtzapple, M.; Ladisch, M. *Bioresour. Technol.* **2005**, *96*, 673.
- (13) McMillan, J. D. In *Enzymatic Conversion of Biomass for Fuels Production*; Himmel, M. E., Baker, J. O., Overend, R. P., Eds.; American Chemical Society Symposium Series Washington, DC, 1994; Vol. 566; pp 292.
- (14) Fan, L. T.; Lee, Y.-H.; Gharpuray, M. M. *Adv. Biochem. Eng./Biotechnol.* **1982**, *23*, 157.
- (15) Millett, M. A.; Baker, A. J.; Satter, L. D. *Biotechnol. Bioeng.* **1976**, 125.
- (16) Cara, C.; Ruiz, E.; Oliva, J. M.; Saez, F.; Castro, E. *Bioresour. Technol.* **2008**, *99*, 1869.
- (17) Sun, Y.; Cheng, J. J. *Bioresour. Technol.* **2005**, *96*, 1599.
- (18) Yang, B.; Wyman, C. E. *Biotechnol. Bioeng.* **2004**, *86*, 88.
- (19) Wyman, C. E. *Ann. Rev. Energy Environ.* **1999**, *24*, 189.
- (20) Allen, S. G.; Schulman, D.; Lichwa, J.; Antal, M. J.; Jennings, E.; Elander, R. *Ind. Eng. Chem. Res.* **2001**, *40*, 2352.
- (21) Nguyen, Q. A.; Tucker, M. P.; Keller, F. A.; Eddy, F. P. *Appl. Biochem. Biotechnol.* **2000**, *84-6*, 561.
- (22) Lee, Y. Y.; Iyer, P.; Torget, R. W. Dilute-acid hydrolysis of lignocellulosic biomass. In *Advances in Biochemical Engineering Biotechnology; Recent progress in bioconversion of lignocellulosics*; Springer-Verlag: New York, USA, 1999; pp 92.
- (23) Saha, B. C.; Bothast, R. J. *Appl. Biochem. Biotechnol.* **1999**, *76*, 65.
- (24) Nguyen, Q. A.; Tucker, M. P.; Boynton, B. L.; Keller, F. A.; Schell, D. J. *Appl. Biochem. Biotechnol.* **1998**, *70-2*, 77.
- (25) Lee, K. C. P.; Bulls, M.; Holmes, J.; Barrier, J. W. *Appl. Biochem. Biotechnol.* **1997**, *66*, 1.
- (26) Torget, R.; Hsu, T. A. *Appl. Biochem. Biotechnol.* **1994**, *45-6*, 5.

- (27) Schell, D. J.; Torget, R.; Power, A.; Walter, P. J.; Grohmann, K.; Hinman, N. D. *Appl. Biochem. Biotechnol.* **1991**, 28-9, 87.
- (28) Torget, R.; Werdene, P.; Himmel, M.; Grohmann, K. *Appl. Biochem. Biotechnol.* **1990**, 24-5, 115.
- (29) Grethlein, H. E.; Allen, D. C.; Converse, A. O. *Biotechnol. Bioeng.* **1984**, 26, 1498.
- (30) Knappert, D.; Grethlein, H.; Converse, A. *Biotechnol. Bioeng.* **1980**, 22, 1449.
- (31) Knappert, D.; Grethlein, H.; Converse, A. *Biotechnol. Bioeng.* **1981**, 67.
- (32) Pinto, P. C.; Evtuguin, D. V.; Neto, C. P. *Ind. Eng. Chem. Res.* **2005**, 44, 9777.
- (33) Shimada, K.; Hosoya, S.; Ikeda, T. *J. Wood Chem. Technol.* **1997**, 17, 57.
- (34) Li, J.; Gellerstedt, G. *Ind. Crop. Prod.* **2008**, 27, 175.
- (35) Nada, A.; Yousef, M. A.; Shaffei, K. A.; Salah, A. M. *Polym. Degrad. Stab.* **1998**, 62, 157.
- (36) Xie, T.; Chen, F. *J. Appl. Polym. Sci.* **2005**, 98, 1961.
- (37) Maciel, G. E. *Science* **1984**, 226, 282.
- (38) Mehring, M. *Principles of High Resolution NMR in Solids*, 2nd ed.; Springer-Verlag: New York, 1983.
- (39) Stejskal, E. O.; Memory, J. D. *High Resolution NMR in the Solid State*; Oxford Univ. Press: Oxford, UK, 1994.
- (40) Fyfe, C. A. *Solid State NMR for Chemists*; C.F.C. Press: Guelph, Ontario, 1983.
- (41) *Solid-State NMR Spectroscopy – Principles and Applications*; Duer, M. J., Ed.; Blackwell Science: Oxford, U.K., 2002.
- (42) Schaefer, J.; Stejskal, E. O. *J. Am. Chem. Soc.* **1976**, 98, 1031.
- (43) Stejskal, E. O.; Schaefer, J.; Waugh, J. S. *J. Magn. Reson.* **1977**, 28, 105.
- (44) Abraham, R. J.; Fisher, J.; Loftus, P. *Introduction to NMR Spectroscopy*; John Wiley & Sons: New York, 1988.
- (45) Keeler, C.; Maciel, G. E. *Anal. Chem.* **2003**, 75, 2421.
- (46) Sullivan, M. J.; Maciel, G. E. *Anal. Chem.* **1982**, 54, 1615.
- (47) Torchia, D. A. *J. Magn. Reson.* **1978**, 30, 613.
- (48) Atalla, R. H.; Gast, J. C.; Sindorf, D. W.; Bartuska, V. J.; Maciel, G. E. *J. Am. Chem. Soc.* **1980**, 102, 3249.
- (49) Pacchiano, R. A.; Sohn, W.; Chlanda, V. L.; Garbow, J. R.; Stark, R. E. *J. Agric. Food Chem.* **1993**, 41, 78.
- (50) Love, G. D.; Snape, C. E.; Jarvis, M. C. *Phytochem.* **1998**, 49, 1191.
- (51) Hatfield, G. R.; Maciel, G. E.; Erbatur, O.; Erbatur, G. *Anal. Chem.* **1987**, 59, 172.
- (52) Earl, W. L.; Vanderhart, D. L. *J. Am. Chem. Soc.* **1980**, 102, 3251.
- (53) Earl, W. L.; Vanderhart, D. L. *Macromol.* **1981**, 14, 570.
- (54) Kolodziejewski, W.; Frye, J. S.; Maciel, G. E. *Anal. Chem.* **1982**, 54, 1419.
- (55) Davis, M. F.; Schroeder, H. R.; Maciel, G. E. *Holzforschung* **1994**, 48, 99.
- (56) Davis, M. F.; Schroeder, H. A.; Maciel, G. E. *Holzforschung* **1994**, 48, 186.

- (57) Davis, M. F.; Schroeder, H. A.; Maciel, G. E. *Holzforschung* **1994**, *48*, 301.
- (58) Haw, J. F.; Maciel, G. E.; Schroeder, H. A. *Anal. Chem.* **1984**, *56*, 1323.
- (59) Haw, J. F.; Maciel, G. E.; Biermann, C. J. *Holzforschung* **1984**, *38*, 327.
- (60) Leary, G. J.; Morgan, K. R.; Newman, R. H.; Samuelsson, B.; Westermark, U. *Holzforschung* **1986**, *40*, 221.